ANALYSIS OF STABILITY AND UNBALANCE RESPONSE OF FLEXIBLE ROTOR SUPPORTED ON HYDRODYNAMIC POROUS JOURNAL BEARING

A Thesis

submitted in partial fulfilment of the

requirements for the degree of

Doctor of Philosophy

By

Swarup Kumar Laha

DEPARTMENT OF MECHANICAL ENGINEERING

INDIAN INSTITUTE OF TECHNOLOGY GUWAHATI

April, 2010

CERTIFICATE

It is certified that the work contained in the thesis entitled **Analysis of Stability and Unbalance Response of Flexible Rotor Supported on Hydrodynamic Porous Journal Bearing,** by **Swarup Kumar Laha,** a student in the Department of Mechanical Engineering, Indian Institute of Technology Guwahati, India, for the award of the degree of the Doctor of Philosophy has been carried out under my supervision and that this work has not been submitted elsewhere for a degree.

(S K Kakoty)
Professor
Department of Mechanical Engineering
Indian Institute of Technology Guwahati
April, 2010

Dedicated to my parents

Acknowledgement

First and foremost I want to express my deeply-felt thanks to my thesis supervisor, Professor S K Kakoty, for his warm encouragement and thoughtful guidance. It has been an honour to be his Ph.D student. I appreciate all his contributions of time, ideas, and discussion to make my Ph.D experience productive and stimulating. The joy and enthusiasm he has for research was contagious and motivational for me, even during tough times in the Ph.D pursuit.

I also thank the members of my doctoral committee: Professor R Tiwari, Professor S K Dwivedy and Professor S Talukdar whose helpful suggestions increased both originality and quality of the thesis.

I am happy to acknowledge my debt to Professor D Chakraborty, HOD of Mechanical Engineering Department for providing me with necessary arrangements to carry out my research.

I want to express my gratitude to my friends at IITG, particularly Sachin Singh, not only for their excellent comments, but also for lively discussion about rotordynamics and vibration.

Last but not the least; I thank my parents for their unconditional love, support and encouragement to pursue my interests.

Swarup Kumar Laha
IIT Guwahati

Contents

List of Figures

List of Tables

Notation

A	Cross-sectional area of the rotor, $\pi D^2/4$
C	Clearance of the bearing
D	Diameter of the rotor
e	Eccentricity of the bearing
e_d	Eccentricity of the disk
E	Young's Modulus of the rotor
$E/(\rho g L)$	Stiffness parameter of the rotor
$\overline{F}_r^B$, $\overline{F}_\phi^B$	Non-dimensional bearing forces in circumferential and axial direction of the bearing respectively, $F_r C^2/(\eta \Omega R^3 L_B), F_\phi C^2/(\eta \Omega R^3 L_B)$
$\overline{F}_X, \overline{F}_Y$	Non-dimensional force component acting on the rotor at the bearing locations in vertical and horizontal directions respectively
g	Acceleration due to gravity
$\left[\overline{G}\right]^e$	Non-dimensional element gyroscopic matrix of the rotor
$\left[\overline{G}^d\right]$	Non-dimensional gyroscopic matrix of the disk
$\left[\overline{G}\right]$	Non-dimensional assembled gyroscopic matrix of the rotor
$\overline{h}$	Non-dimensional film thickness, $h/C = 1 + \varepsilon \cos\theta$
H	Thickness of the porous bush
k	No. of elements
$\left[\overline{K}\right]^e$	Non-dimensional element stiffness matrix of the rotor
$\left[\overline{K}\right]$	Non-dimensional assembled stiffness matrix of the rotor
K_x, K_y, K_z	Permeability of the porous bush in circumferential, radial and axial direction respectively
$\overline{K}_x$, $\overline{K}_z$	Non-dimensional permeability factor of the porous bush in circumferential and axial direction respectively, $K_x/K_y, K_z/K_y$
l	Length of rotor element, L/k

$\bar{l}$	Non-dimensional rotor element length, l/C
L	Length of the rotor
L_B	Length of the bearing
L_B/D	Aspect ratio of the bearing
m_d	Mass of the disk
$\bar{m}$	Mass parameter, $C\Omega^2/g$
$\bar{m}_d$	Ratio of disk mass to shaft mass, $m_d/(\rho AL)$
$\left[\bar{M}_T\right]^e$	Non-dimensional element translational mass matrix of the rotor
$\left[\bar{M}_R\right]^e$	Non-dimensional element rotational mass matrix of the rotor
$\left[\bar{M}^d\right]$	Non-dimensional mass matrix of the disk
$\left[\bar{M}\right]$	Non-dimensional assembled mass matrix of the rotor-disk
n	Number of discrete points in Poincaré map
$\bar{p}$	Non-dimensional pressure in the clearance space of bearing, $pC^2/(\eta UR)$
$\bar{p}'$	Non-dimensional pressure in the porous media of the bearing, $p'C^2/(\eta UR)$
$\{\bar{q}\}$	Non-dimensional displacement vector
R	Radius of the rotor
$R/(2L)$	Slenderness ratio of the rotor
R/C	Clearance ratio of the bearing
S	Sommerfeld number
$\bar{t}$	Non-dimensional time, Ωt
$\bar{T}$	Non-dimensional time, ΩT
$\bar{v}$, $\bar{w}$	Non-dimensional horizontal and vertical deflection of the rotor respectively, $v/C, w/C$
W	Load per bearing, $(\rho AL + m_d)\,g/2$
$\bar{y}$	Dimensionless radial coordinate of the bearing, y/H
$\bar{z}$	Dimensionless axial coordinate of the bearing, $2z/L_B$

β	Bearing feeding parameter, $12K_y R^2 / \left(C^3 H\right)$
ε	Eccentricity ratio of the bearing, e/C
η	Viscosity of the lubricant
ν	Poisson's ratio
ω	Whirling speed of the rotor
Ω	Rotor spin speed
ϕ	Attitude Angle
Φ	Shear factor
ρ	Mass density of the rotor material
θ	Dimensionless circumferential coordinate of bearing, x/R

Abstract

Rotating machines are one of the most important and widely used machineries in modern engineering world. Now-a-days modern rotating equipments have a number of complicated accessories attached with it and they are also made extremely flexible. They are also required to run at higher speed, much higher than their first critical speed. Fluid-film bearings supporting the rotating shafts play an important role in the dynamic behaviour of the rotors because of their stiffness and damping properties. Hydrodynamic bearings are one of the most widely used bearings to support the rotating shafts. Rotor-bearing systems exhibit a wide variety of phenomena pertaining to its operations which if not properly addressed and rectified may lead to catastrophic failure of the system. One such rotor-bearing phenomenon is the self-acting rotor vibrations induced by the hydrodynamic bearings and popularly known as oil-whirl and oil-whip which have severe repercussion on the functioning of the rotors. Another important area of rotor dynamics is the unbalance response of the rotors supported on the hydrodynamic journal bearings. Due to the inherent unbalance present in the rotor-bearing system high amplitude of vibrations are observed when the rotor is operated near its critical speed. In this context, a study of the rotor-bearing system considering the non-linearity of the oil-film forces is necessary.

In this thesis a methodology has been proposed to study stability and the unbalance response of a flexible rotor supported on two identical porous hydrodynamic journal bearing. Timoshenko Beam theory has been used for finite element formulation of the rotor. Finite hydrodynamic porous oil-film bearing is considered for estimation of hydrodynamic bearing forces. The rotor-bearing system equations are presented in non-dimensional form. In the non-dimensional scheme adopted in the work two new non-dimensional parameters are obtained. The effects of various non-dimensional rotor-bearing parameters including these two parameters on stability and dynamic response have been investigated and presented.

An investigation of stability of a fully balanced rotor has been carried out using a non-linear time transient method. This analysis enables to trace the journal centre locus at different locations of the rotor. Stable, critically stable and unstable

trajectories are shown. The stability curves have been drawn for different rotor-bearing parameters. The effect of bearing location is also studied.

Then unbalance is introduced in the model. Waterfall diagrams are obtained to study unbalance, oil-whirl for different rotor-bearing parameters. It has been observed that at low spin speed, unbalance is the major driving force and with an increase in the spin speed, oil-film forces take over as the major cause of vibration. Thus, whirling of the rotor gradually changes from synchronous to sub-synchronous. Waterfall diagrams are obtained for both run-up and run-down processes. Distinct dynamic behaviours are observed for run-up and run-down, which is known as hysteresis.

Bifurcation analysis of the rotor-bearing system has also been carried out and Poincaré maps, time response, FFT-spectrum, dynamic trajectories and bifurcation diagrams have been utilized as diagnostic tools to study the non-linear dynamics of the rotor-bearing system. It has been found that the dynamic behaviour of the system can be periodic and quasi-periodic depending on the operating conditions. Also it is observed that when rotating speed is increased the rotor-bearing system undergoes Hopf Bifurcation.

Initially, analysis of rotors supported on porous journal bearings have been carried out with an assumption that the lubricating fluid enters the clearance space of the bearing with a zero tangential velocity at the porous medium. However, earlier investigations suggest that this assumption is at best an approximation only. Therefore, the effect of tangential slip velocity using Beavers-Joseph criterion has also been carried out. The investigation reveals that stability of the system improves with increase in slip velocity. Nevertheless, it has also been observed that dynamic characteristics are not much affected by tangential velocity slip.

CHAPTER 1

Introduction

1.0 State of the Art

Rotor-bearing systems are one the of most common and essential machine parts used in many industrial machines such as turbo-generators, steam and gas turbines, IC engines, compressors, pumps, computer disk storages etc. Their performance is of utmost importance in modern industrial world. Now-a-days due to the ever increasing need of power and higher speeds, the rotors are made extremely flexible and also have a number of complicated accessories attached with the rotor. They are also made light weight and required to run much above the critical speed. In view of this, study of vibrational and dynamic characteristics of the rotor-bearing systems is essential in designing rotating equipments requiring in-depth rotor-dynamic modelling.

Rotor-bearing systems are subjected to unstable motions which if not addressed correctly may lead to catastrophic failures. Instabilities in rotor-bearing systems may arise due to a number of reasons such as fluid film bearings, shaft stiffness asymmetry, internal friction between mating components and aerodynamic forces.

Fluid film bearings, widely used in rotating equipments, to support load affect the dynamic behaviour of rotors significantly. Hydrodynamic forces from the bearing induce a self-acting vibration in the rotating machines at which the shaft whirls at around the half of the spin speed which is popularly known as half-frequency whirl or oil whirl. When the rotor speed reaches twice of the system natural frequency, half-frequency whirl becomes nearly equal to the system resonance speed; at this stage violent whipping is observed which is known as oil whip. There is a number of industrial case histories reported in which oil whip is the primary cause of rotor-bearing system instability [1, 2]. Porous oil bearings are one of most widely used journal bearings which are simple in design and need little maintenance. Porous bearings are made of sintered materials. Rotors supported by porous bearing finds its application in situation where replenishment of lubricating oil is difficult *e.g.* inside some intricate place where opening up the machinery parts for re-filling the lubricant is a cumbersome and time-consuming job. The pores of the porous bearing act as oil reservoir. Many equipments in everyday use, such as domestic appliances and audio equipments have porous bearings to support a rotating shaft. Some typical example where rotors supported by porous bearing are: computer hard-disk, electric motor, vacuum cleaner, textile spinning spindle etc. Unbalance is another major cause of concern as at critical speeds the rotors exhibit high amplitude of vibration due to the residual unbalance. Due to the presence of the different attachments to the rotor such as disks, pulleys, gears, keys etc. and manufacturing defects rotor centre of mass does not always coincide with the geometric centre. An external force acts on the rotor because of this eccentricity of the unbalance mass. Unbalance response becomes maximum when the shaft speed reaches the fundamental natural frequency.

Thus, rotors supported on porous oil bearings and under unbalance excitation may have to withstand both synchronous and sub-synchronous vibrations of high amplitude. As these synchronous and sub-synchronous vibrations become significant at different speeds, the transient response of the rotor-bearing system during speed-ascending and descending process may be obtained for better understanding of the dynamics of a rotor-bearing system.

1.1 Literature Review

1.1.1 Instability in Rotor-Bearing System

Since the publication of Newkirk and Taylor's [3] classical works on the oil whirl in 1925, extensive research has been carried out to study rotor-bearing instability. They first reported the experimental evidence of violent whipping of a flexible shaft due to fluid-film bearing. The whip started at a speed twice the first critical speed and persisted at higher speeds. Newkirk [4] reported whirling of a very short and stiff shaft at low speeds with whirl frequencies approximately half of the running speed of the shaft. Hagg [5] investigated about the stability of rotating machines on oil film journal bearings and found that the upper limit of the whirling frequency is one-half of the rotating speed. Hori [6] confirmed the phenomenon of oil whip in 1959. Pinkus [7] in 1957 conducted an extensive experimental investigation on oil whirl. He studied the effects of loading, speed, viscosity, unbalance, flexibility, and external excitation on oil whirl. Ehrich [8] in 1966, studied subharmonic frequency in rotor-dynamic vibration. He observed that the subharmonic appears when a turbo-machine is operating near the twice of its fundamental frequency. Lund [9, 10] studied the stability and damped critical speeds and modal response of a flexible rotor supported by fluid-film bearings. The bearings were modelled by their linearized stiffness and damping coefficients. These stiffness and damping coefficients of the bearing were used to represent the forces developed in the bearings when the journal centre vibrates with small amplitude. Muszynska [11, 12] developed a mathematical model to study the effect of oil whirl and whip. The analysis yielded the threshold speed of stability. The model could also evaluate stability characteristics of the rotor synchronous vibration. In her study multiple regimes stability were observed with the increase in speed.

Hagg and Warner [13] investigated the phenomena of oil whip of flexible rotors through an electric analogue study and showed that the flexibility of the rotor decreased the stability threshold. Holmes [14] investigated the role of oil-film bearing for causing instability of rotors and found that presence of external damping could suppress the instability. Manfrida and Martelli [15] applied finite element method for non-linear stability analysis for journal bearing in 1979. Rao [16] showed that instability of rotors mounted on fluid film bearings could occur with one of the cross-coupled stiffness of the bearing being negative. It had been shown that this instability occurs in a narrow range of speed at 2X the spin speed.

Akers [17] solved the equation of motion of finite journal bearing by using non-linear time transient method. Kirk and Gunter [18, 19] carried out both linear and non-linear stability analysis using short bearing approximation. Rotor transient response orbits were obtained to show the effects of unbalance, steady loading, and cyclic and rotating loads upon stability. Sinhasan and Goyal [20] carried out time-transient response analysis of circular bearing with non-Newtonian lubricant. Kumar and Rao [21, 22] investigated the stability of a rigid rotor in turbulent finite hydrodynamic journal bearing and hybrid bearing using the Constantinescu's turbulent lubrication theory. Stability curves were drawn for different aspect ratio of the bearing and Reynolds number. Pai and Majumdar [23] studied stability of oil journal bearing under dynamic load considering oil-film history. Linearized perturbation theory about the equilibrium point was applied to predict the threshold of stability. Raghunandana and Majumdar [24] studied stability of a journal bearing system with a non-Newtonian lubricant using non-linear time-transient method. Kakoty and Majumdar [25-28] investigated the effect of fluid film inertia on the stability of oil journal bearing. It was shown that the fluid inertia effect is to be considered in the analysis when modified Reynolds number is around one. It was found that although the steady-state characteristics were not affected much due to fluid film inertia, its importance in the case of stability could not be ignored.

Kakoty and Kalita [29] analyzed the stability of flexible rotors mounted on fluid film bearings. The analysis was carried out to find the effect of bearing geometry and viscosity on stability characteristics of rotor-bearing system. They also studied the stability of circular and non-circular bearings supporting flexible and rigid rotor [30, 31]. It was shown that for high values of slenderness ratio of the rotor (above 0.067) the flexible rotor threshold speed approached rigid rotor threshold speed. Chen [32] used a direct numerical method to estimate the instability threshold and stability boundaries of flexible rotor-bearing system. FEM was used to obtain the system equation of motion. El-Shafei *et al.* [33] carried out experimental investigation on oil whirl and oil whip. Experiments were conducted at various unbalances, pressures and misalignments of coupling. It was shown that the misalignment was the most important parameter for the onset of instability. Zhao *et al.* [34] studied stability and response analysis of a symmetrical single disk flexible rotor-bearing system. In their analysis both linear and non-linear oil film forces were used. JianPing *et al.* [35, 36] analyzed the non-linear dynamic behaviour of a rotor-bearing system based on continuum model. A theoretical model for oil-whip phenomena was developed. Castro *et al.* [37] also studied oil whirl and whip instabilities in rotor-bearing system for both vertical and horizontal rotor configuration. The theoretical results were found to be in good agreement with the experimental investigation.

Chattopadhyay and Majumdar [38] studied stability of rigid rotor supported in porous oil journal bearings with tangential velocity slip. The effect of slip parameters, eccentricity ratios and bearing aspect ratios on the stability were presented. Kumar [39] studied conical whirl instability of an unloaded rigid rotor supported on a turbulent flow hybrid porous journal bearing. The effects of bearing feeding parameter, Reynolds number, ratio of wall thickness of porous bush to journal radius and anisotropy of the porous material on the stability of rotor-bearing system were investigated. Guha [40] also studied conical whirl instability of rigid rotor supported on hydrodynamic porous oil journal bearing with tangential velocity slip. The linearized perturbation theory was applied to estimate the threshold of stability.

1.1.2 Effect of Unbalance on Rotor-Bearing System

Unbalance is one of the most common causes of excessive vibration observed in rotor-bearing systems because unbalance results in resonance when the rotor speed approaches its natural frequency. Unbalance is always inherent to the system. It may come from manufacturing defect, material non-homogeneity, keyways etc. or may be due to wear, thermal bending etc. Unbalance response is affected by gyroscopic effect, stiffness and damping parameters of the bearing, rotor misalignments etc. Therefore, the study of the dynamic behaviour of a rotor-bearing system under unbalance condition is very much pertinent.

Lund and Orcutt [41] studied unbalance response of a flexible rotor by using 8-cooefficients bearing model and using the transfer matrix method. Ozguven and Ozkan [42] applied finite element method to study the unbalance response of a rotor-bearing system. The effect of shear deformation and internal damping were also included in their analysis.

Rao [43] presented the dynamic unbalance response of a single-mass Jeffcott rotor in hydrodynamic bearing. The cross-coupled stiffness coefficients were considered and damping was neglected. It was shown that either there could be two distinct critical speeds of the rotor with backward whirl between them or there is no possible conventional critical speed. Sharan and Rao [44] studied unbalance response of a multi-disk rotor supported on fluid-film bearing using influence coefficients method. The bearing stiffness and damping coefficients were considered to be speed-dependent. Curti *et al.* [45] studied unbalance response of rotors by dynamic stiffness method. Lee and Jei [46] applied modal analysis of continuous rotor to calculate the unbalance response. Genta and Bona [47] also applied modal analysis to estimate unbalance response of rotors with damped natural system.

Raffa and Vatta [48] used the dynamic stiffness method to study linear rotor-bearing system. Rotating Timoshenko beam was considered in their analysis. The method was applied to obtain the critical speeds of a simple rotor and also steady-state unbalance response of two-rotor system with anisotropic support. Shih and Lee [49] presented a new method for estimating unbalance distribution of flexible shaft and rigid disks based on Transfer matrix method for analyzing the steady-state response of a rotor bearing system. Hong and Park [50] proposed a method to estimate unbalance response of a multi-span rotor-bearing system by an improved substructure synthesis scheme. In the proposed method the gyroscopic terms and bearing parameters were also included. Lee and Ha [51] predicted maximum unbalance response of a gear-coupled two-shaft rotor-bearing system based on finite element method.

Zhao *et al.* [52] presented both theoretical and experimental analysis of unbalance response of a flexible rotor supported on squeeze film dampers. Vázquez [53] carried out experimental analysis of stability and unbalance response of a flexible rotor supported on flexible bearing. Yang and Lin [54] estimated distributed unbalance of rotors. In their study eccentricity distribution was assumed and FEM was adopted. Zachariadis [55] carried out unbalance response analysis of rotors supported on hydrodynamic bearings placed closed to the nodal points of excited vibration modes. He showed that the traditional 8-coefficient bearing model used in linear rotordynamics is inadequate for unbalance response calculation. To mitigate this, the time varying tilt angles between journal and bearings were considered which led to the adoption of 32-coefficient bearing model. Liu *et al.* [56] studied the non-linear dynamics of an unsymmetrical generator-bearing system using both non-linear oil-film forces and unsymmetrical stiffness coming from the rotor. Cascade diagrams were plotted to examine the dynamic behaviour of such system. San Andrés *et al.* [57] carried out experimental analysis of rotordynamic performance of a small rotor supported on two bump-type Gas Foil Bearings (GFB) of length and diameter equal to 38.10 mm. Coast down rotor responses from 25 krpm to rest were shown for various imbalance conditions and increasing air feed pressures. It was shown that the peak amplitudes of rotor synchronous motion at the system critical speed were not proportional to the imbalance. Furthermore, for the largest imbalance, the test system showed subsynchronous motions from 20.5 krpm to 15 krpm with a whirl frequency at ~50% of shaft speed. Rotor imbalance worsens the severity of subsynchronous motions, thus denoting a forced nonlinearity in the GFBs. Wilde and Andrés [58] carried out linear rotordynamic analysis of a test rotor supported on externally pressurized gas bearings. Model predictions were compared with experiments conducted on a small rotor supported on three lobed hybrid (hydrostatic/hydrodynamic) rigid gas bearings. Predictions for the rotor-bearing system synchronous response to imbalance showed good agreement with measurements during rotor coast downs. De Santiago and Andrés [59] investigated imbalance response of a massive 45 kg rotor supported on series (flexure pivot) tilting pad bearings and integral squeeze film dampers (SFDs). Coast-down experiments from 9000 rpm were conducted for increasing levels of rotor imbalance, and equivalent system damping coefficients identified from the peak amplitude of rotor response while traversing cylindrical mode critical speeds. The tests performed with locked (inactive) and active SFDs demonstrated the effectiveness of the flexible damped support in reducing the system critical speed and improving the overall rotor response with reduced transmitted forces to ground. The SFDs allowed safe rotor operation with values of imbalance twice as large as the maximum sustained by the rotor supported on tilting pad bearings alone.

1.1.3 Non-linear Dynamic Analysis of Rotor-Bearing System

The dynamic behaviour of a rotor-bearing system depends on unbalance forces as well as the non-linear characteristics of the fluid-film forces. Due to the influence of the non-linear hydrodynamic forces the rotor motion is not in general synchronous with the spin speed, as the fluid-film also causes self-induced vibration which is commonly known as oil whirl. The rotor motion may be in some cases quasi-periodic or chaotic depending upon system parameters.

Myers [60] applied Hopf Bifurcation Theory (HBT) for the stability analysis of a rigid rotor symmetrically supported by two identical, infinitely long journal bearing. Hollis and Taylor [61] also carried out similar type of analysis by using short bearing approximation. Sundarajan and Noah [62] also applied HBT to study subcritical and supercritical bifurcation for rotor-bearing system with finite journal bearing. Wang and Khonsari [63] applied HBT to study the effects of turbulence in bearing on rigid rotors. Deepak and Noah [64] experimentally showed the existence of supercritical and subcritical bifurcation regime in rotor-bearing system. Shaw and Shaw [65] studied the effect of unbalance on oil whirl. Bifurcation diagrams were presented to study the non-linear dynamics of rigid rotor supported by short journal bearing. Lin and Hwang [66] applied Hopf Bifurcation Theory to predict the critical stability boundary for short porous journal bearing system using Brinkman model.

Brown *et al.* [67] showed that a rigid rotor supported by short journal bearing behaved chaotically when the rotating unbalance force exceeded the gravitational load. Fractal dimension concept was applied to predict onset of chaotic motion. Adiletta *et al.* [68] studied the conditions that gave rise to chaotic motion in rigid rotor on short journal bearing. They also carried out theoretical and experimental investigation on non-linear dynamics of rigid rotor supported on short journal bearing

[69, 70]. Brancatti *et al.* [71] studied stability of periodic motion of an unbalanced rigid rotor supported on short journal bearing. Kim and Noah [72] carried out bifurcation analysis of Jeffcott rotor with bearing clearance. A Harmonic Balance/Alternating Frequency Time technique was developed to obtain synchronous and subsynchronous whirling motion of horizontal Jeffcott rotor.

Chen and Yau [73] studied chaos in unbalance response of a flexible rotor supported in oil-film bearing with non-linear suspension. Poincaré maps, bifurcation diagram and power spectra were used to analyze the behaviour of the bearing centre in horizontal and vertical direction under different operating conditions. Karpenko *et al.* [74] did the bifurcation analysis of a preloaded Jeffcott rotor. It was shown that the dynamic behaviour can be effectively controlled by varying the preloading and damping of the rotor. Wang *et al.* [75] studied the non-linear dynamics of flexible rotor supported by externally pressurized porous gas journal bearing. Their works showed how the dynamic characteristics of the rotor changed with bearing number and rotor mass.

Shen *et al.* [76] carried out non-linear behaviour analysis of a rigid rotor supported in elliptical bearing system. The investigation showed that the motion can be sub-synchronous, quasi-periodic or chaotic depending on the rotor spin speed. Valverde *et al.* [77] studied stability and bifurcation analysis of a modified geometrically non-linear orthotropic Jeffcott model with internal damping. Wenhui *et al.* [78] studied the non-linear dynamic behaviour of flexible rotor-bearing system with two unbalanced disks. Maximum Lyapunov exponent was calculated to predict the onset of chaotic motion in the system. JianPing [35, 36] also showed that the rotor underwent Hopf Bifurcation as the rotor speed was increased. Shen *et al.* [79] carried out numerical and experimental analysis of rotor-bearing-seal system. The analysis was based on the Jeffcott rotor and the nonlinear oil-film forces were obtained by short bearing approximation. In this work so-called Muszynska nonlinear seal force model was adopted. It was shown that the vibration amplitude could be reduced by including the seal system. Wang and Khonsari [80] showed that the rotor stiffness had profound effect on the bifurcation characteristics of a flexible rotor. Wang and Khonsari [81] also demonstrated the existence of hysteresis phenomenon using Hopf bifurcation theory. The effect of oil viscosity on the hysteresis phenomenon was investigated. Castro *et al.* [37] showed the effects of unbalance, journal bearing parameters and rotor arrangement (vertical or horizontal) on the bifurcation characteristics of a flexible rotor supported on short journal bearing. San Andrés *et al.* [82] presented nonlinear rotor-bearing models for prediction of the dynamic shaft response of automotive turbochargers (TC) supported on floating ring bearings (FRBs). The static forced performance of the support FRBs considered lubricant thermal effects, thermal expansion of the shaft and bearings, and entrance pressure losses due to centrifugal flow effects. The linearized rotordynamic force coefficients for the inner and outer lubricant films were estimated. These coefficients were used with the rotor model to predict the synchronous response to imbalance and the system natural frequencies and stability. The nonlinear response model predicted the total shaft motion, with FFTs showing the synchronous response, and amplitudes and whirl frequencies of subsynchronous motions. Zhu and Andrés [83] conducted tests on a small rotor supported on flexure pivot hydrostatic pad gas bearings (FPTPBs) to demonstrate stable rotordynamic responses up to 100,000 rpm (limit of the drive motor). Test rotor responses showed that the feed pressure raised the system critical speed (increase in bearing direct stiffness) while the viscous damping ratio decreased. The predictions correlated favourably with experimentally identified (synchronous) direct stiffness bearing force coefficients. Tests without feed pressure showed that the rotor becomes unstable at ~81 krpm with a whirl frequency ratio of 20%. A comprehensive nonlinear rotordynamics model coupled to a complete fluid-film-bearing model was developed by San Andrés *et al.* [84]. The computational design tool predicted the limit cycle response for several inner and outer film clearances and operating conditions including rotor speed and lubricant feed pressure. They predicted linear and nonlinear shaft motion of an automotive turbocharger supported on a semi-floating ring bearing. The shaft motion predictions were compared to measurements of shaft motion at the compressor nose for speeds up to 240 krpm, and for lubricant inlet pressure of 4 bar at 150°C. The nonlinear results showed two subsynchronous whirl frequencies whose large magnitudes agreed well with the experiments. Holt *et al.* [85] carried out nonlinear analysis of turbocharger supported by floating ring bearings. Waterfall acceleration spectra versus rotor speed were obtained to show the effects of increasing lubricant inlet pressure and temperature on turbocharger rotordynamic response. A comprehensive analysis of the test data showed regimes of speed operation with two subsynchronous whirl motions (rotordynamic instabilities). It was shown that lubricant feed pressure delayed the onset speed of instability for the most severe subsynchronous motion and the effect of lubricant feed temperature is minimal on the onset. Further, it was observed that rotor imbalance suppressed the subsynchronous instabilities at large rotor speeds.

1.1.4 Porous Oil Bearing

The extensive use of porous oil journal bearings is found in industries because of their low cost and reduced oil requirement. Porous bearing can be used where other bearings cannot be placed due to lack of space or when replenishment of lubricant is difficult. The behaviors of various types of porous bearings such as squeeze films, externally pressurized bearings, journal bearings and slider bearings have been studied by various researchers and authors.

Due to the late development of powder metallurgy, the studies on porous bearings are comparatively new. The flow of the fluids through the porous media has been discussed extensively in many textbooks as well as in research papers.

Analytical studies on the characteristics of porous bearings lubricated with incompressible and compressible fluids have increased tremendously since the initial investigation of Morgan and Cameron [86] in 1957.

Cusano [87] Studied porous journal bearing based on Darcy's Model, neglecting the effect of solid boundary on fluid flow through porous media. Cheng and Rowe [88] presented a selection strategy for the design of externally pressurized porous journal bearing. The strategy was concerned with the selection of bearing type and configuration, the fluid feeding device and the bearing material.

Kaneko and Obara [89] had experimentally investigated the mechanism of lubrication in porous oil journal bearing. Quan and Wang [90] proposed a new type of porous metal bearing with non-uniform distribution of permeability which showed that the new bearing had lower friction and higher load capacity than the ordinary porous bearing, and there was no initial temperature rise and friction increase with the new bearing. Quan *et al.* [91] conducted experimental analysis under high speed (around 69000 rpm) and light load conditions and found that porous bearings could work under hydrodynamic conditions even under these high speeds. Necessity to supplement oil was emphasized to maintain hydrodynamic lubrication for high speed application in their work.

There are number of investigations to study the effect of velocity slip on the performance of self-acting porous bearings since its mathematical model proposed by Beavers and Joseph. Beavers and Joseph [92] proposed a boundary condition which accounts for a non-zero tangential velocity at the porous surface. It was assumed that slip velocity for the free fluid is proportional to the shear rate at the porous boundary. The validity of the model for velocity slip had been experimentally verified by Beavers *et al.* [93]. Murti [94] investigated the steady-state characteristics of narrow porous bearing for both small and arbitrary wall thickness considering the slip at the boundary of the porous medium following Beavers-Joseph model. Rouleau and Steiner [95] obtained the steady state characteristics of a finite full journal bearing using the continuity for velocity and pressure at the interface. It was observed that the effect of this slip velocity on the static characteristics is negligible.

Cusano [96] presented an analytical solution to predict the steady state characteristics of finite starved porous bearings with arbitrary wall thickness using the modified Reynolds equation to take into account velocity slip at the interface between the oil film and porous wall. For a particular value of eccentricity ratio and active film arc angle, total side flow which consisted of flow from the clearance gap and that from the porous ends, increased with the permeability parameter. Similar trend was observed in case of coefficient of friction and Sommerfeld number.

Prakash and Vij [97] presented an analytical solution for performance characteristics of a narrow journal bearing taking into account the effect of velocity slip at the surface of a porous medium by using the Beavers-Joseph criterion. According to Chandra *et al.* [98] porosity and the ratio of clearance to journal radius were the factors that determined the effect of slip on steady state and dynamic behaviour of porous bearing. Chattopadhyay and Majumdar [99] presented a theoretical investigation on the static characteristics of externally pressurized porous oil journal bearings considering the Beavers-Joseph model slip flow at the porous oil journal bearing interface. A numerical method had been employed to solve the governing differential equations. The effect of slip, eccentricity ratio, slenderness ratio, speed parameter and anisotropy of permeability on the load carrying capacity, friction coefficient, and attitude angle and oil flow rate had also been studied. Gururajan and Prakash [100] examined the effect of velocity slip in a thin walled infinitely short rough porous journal bearing operating under steady condition in a hydrodynamic regime.

Kumar and Rao [101] carried out steady-state performance analysis of a finite hydrodynamic porous oil journal bearing in turbulent regime which was based on Constantinescu’s turbulent lubrication theory. Lin and Hwang [102] studied hydrodynamic lubrication of finite porous journal bearing using Brinkman-extended Darcy's model.

Gururajan and Prakash [103] analyzed the effect of surface roughness in an infinitely long porous journal bearing operating under steady conditions. Elsharkawy and Guedouar [104] also studied hydrodynamic lubrication of porous journal bearing using a modified Brinkman-extended Darcy's model along with Elrod's cavitation algorithm. Meurisse and Giudicelli [105] developed a 3D conservative model for hydrodynamic porous journal model. Chen *et al.* [106] studied the phenomenon of stress jump at the porous media-fluid film interface.

1.1.5 Application of Finite Element Method in Rotordynamics

The dynamic modelling of rotors is essential to the dynamic response analysis and study of its vibration characteristics. Early rotordynamic formulations were based on either (1) analytical method or (2) transfer matrix method. However, the finite element method in rotor-bearing system is the most flexible and appropriate method. This method can be very effectively used when the rotor system is very large and complicated.

The utilization of FEM by Archer [107] yielded highly successful result. Ruhl and Booker [108] were the pioneers in using finite element method to study the stability and unbalance response in turbo-rotor system. In their formulations, only bending energy and translational kinetic energy were considered, whereas the effects of rotary inertia, gyroscopic moments, shear energy, internal damping were neglected. Thorkildsen [109] developed a finite element model, which was more general than Ruhl's model by including rotary inertia and gyroscopic moment. Dimaragonas [110] presented a more general model by considering the effects of rotary inertia, gyroscopic effects, and internal damping. Gasch [111] presented a model that was similar to Dimaragonas's but included the effect of distributed eccentricity. Nelson and McVaugh [112] developed a procedure for dynamic modelling of rotor-bearing system which consisted of rigid disks, distributed parameter finite rotor elements and discreet bearings. The FE model included the effects of rotary inertia, gyroscopic moments and axial load by using a consistent mass matrix approach. The natural whirl speed and unbalance response of typical overhung system was presented for two sets of bearing parameters (i) undamped isotropic and (ii) undamped orthotropic. Zorzi and Nelson [113] generalized the work of Nelson and McVaugh [112] by including both internal viscous and hysteretic damping in the same finite element model. It was shown that both viscous and hysteretic damping produced circulatory term in the generalized equation of motion which encouraged destabilization in this non-conservative system. Both forms of damping destabilized the rotor system and induced non-synchronous forward precession. The stabilizing effect of anisotropic bearing stiffness and external damping were also demonstrated. Rouch and Kao [114] demonstrated that dynamic reduction of finite element matrices in rotordynamic analysis had the advantage of saving computation time and modelling accuracy. Application of this method requires an extension of to account for skew-symmetric gyroscopic matrices. Kim and Lee [115] developed a power matrix reduction technique to analyze rotor-bearing system by using modal data of the isotropic undamped stationary parts. This method gave significant reduction in computation time and core size while maintaining accuracy and flexibility.

Nelson [116] utilized Timoshenko Beam Theory for establishing shape functions, and based on these shape functions, the system finite element matrices of the governing equations were derived. A shear parameter was introduced in the finite element model to account for transverse shear deformation. Setting this parameter to zero, the Timoshenko model could be reduced to Euler-Bernoulli beam. A finite element model considering shear deformation and internal damping was employed by Ozguven and Ozkan [42] to study the unbalance response of a rotor-bearing system. Chen and Ku [117] developed a three nodal, C^0 Timoshenko beam finite element model to analyze the natural whirl speeds of a rotating shaft with different end conditions. The effects of translational and rotary inertia, gyroscopic moments, bending and shear deformation were included in the mathematical model. Ku [118] presented whirl speed of a rotor-bearing system of the above model by incorporating internal viscous and hysteretic damping. Results of backward and forward whirl speed and damped stability were presented. Khulief and Mohiuddin [119] obtained the dynamic response of rotors by using finite element model with two modal truncation scheme: one with planar (undamped) modes and the other with complex (damped) modes. JianPing *et al.* [35, 36], Castro *et al.* [37] and Liu *et al.* [56] applied finite element method and direct integration scheme to obtain the dynamic response of a flexible rotor supported on journal bearing. Among many others, Chen [32], Hong and Park [50], Yang and Lin [54], Zachariadis [55] also utilized finite element method for their analyses.

1.2 Scope of the Present Work

It has been observed that there are two distinct trends in studying rotor-bearing systems. When flexible rotor systems are mostly analyzed by incorporating hypothetical bearings [9-12, 16], bearing characteristics and bearing instability study are carried out mostly for rigid rotors mounted on hydrodynamic bearings [21-28, 38-40]. There are few examples where simplified model of rotor-bearing system is taken up based on short or long bearing approximation [34-37]. Thus, in the earlier analysis of rotor supported by fluid-film bearings have many simplifying assumptions such as rigid rotor or approximate bearing (short or long bearing) solution. In view of this, it is pertinent to develop a method to analyze different characteristics of rotor-bearing system, rotor being flexible and supported by finite bearings. Porous bearings are found to be less stable than a plain journal bearing [22]. Further, it has been mentioned already that rotors supported by porous bearing finds its application in situation where replenishment of lubricating oil is difficult. As porous bearings are used in large number of applications, the knowledge of dynamic behaviour of a flexible rotor supported by porous journal bearings would be of utmost importance. Therefore, it would be relevant to study the stability of flexible rotors supported on porous bearings. However with zero bearing feeding parameter, the bearing reduces to a plain journal bearing and therefore, the stability characteristics of plain journal bearing supported rotors have also been studied in the present work. Further, no literatures on unbalance response and bifurcation characteristics of rotors supported on porous hydrodynamic bearings are available. It has also been observed that in all the previous analyses of rotor supported on porous bearings, the rotor was assumed to be rigid. The present study aims to fill the gap in understanding of dynamic behaviour of a rotor mounted on porous oil bearing by eliminating the simplifying assumptions for rotor-bearing system and considering unbalance effects. By taking into consideration a finite bearing solution instead of approximate solution and a flexible rotor model, the results of the present analysis would be more practical and reliable.

In this present work, a methodology has been proposed to study the stability and non-linear dynamic response of a flexible rotor mounted on two finite porous hydrodynamic bearings. The rotor has been modelled by finite element formulation of Timoshenko Beam theory, thus considering translational and rotary inertia, bending and shearing deformation and gyroscopic effect. Finite hydrodynamic porous oil-film bearing has been considered for estimation of hydrodynamic bearing forces. An attempt has been made in this thesis to carry out a non-dimensional study of the rotor-bearing system. To facilitate such a study the rotor-bearing system equations are non-dimensionalized and non-dimensional parameters are derived. The effects of various non-dimensional rotor-bearing parameters on the dynamic response have been investigated and presented.

A theoretical analysis using a non-linear time transient method has been carried out to study the stability of a fully balanced flexible rotor supported on two symmetrical finite porous oil journal bearings. This analysis enables to trace the journal centre locus at different locations of the rotor. Several trajectories of the journal centre have been obtained for different operating conditions. The stability curves have been drawn for different rotor-bearing parameters.

Unbalance also causes potentially damaging vibration in rotor-bearing system, which becomes severe when the rotor operates near its critical speed. In the mathematical model an unbalanced disk mass has also been introduced for studying unbalance responses. Waterfall diagrams are then obtained to study unbalance, oil-whirl and oil-whip for different rotor-bearing parameters. Waterfall diagrams are plotted for both run-up and run-down conditions.

Finally, bifurcation analysis of the rotor-bearing system is carried out. Poincaré maps, time response, power spectrum, dynamic trajectories and bifurcation diagrams are utilized as diagnostic tools to study the non-linear dynamics of the rotor-bearing system.

1.3 Organization of the Thesis

The present work deals with analysis of stability and unbalance response of flexible rotor supported by porous journal bearings. The present thesis is broadly divided into six chapters. Chapter 1 deals with state of the art and literature review of previous works. Mathematical formulation of flexible rotor based on Timoshenko beam theory and the basic governing equations of porous bearing is shown in chapter 2. A non-dimensional form of the equation of motion is also presented in this chapter. Chapter 3 deals with stability analysis of a fully-balanced flexible rotor using non-linear transient method. Then, an unbalanced rotor supported by porous bearing is considered in chapter 4. The dynamic behaviour of the rotor-bearing is studied by generating waterfall diagrams. Bifurcation characteristic of the system is also studied in detail in this chapter. Chapter 5 deals with the effect of tangential velocity slip on stability and non-linear dynamic response of rotor-bearing system. Finally, the major inferences drawn from the work carried out in this thesis are produced in chapter 6. Also, the non-dimensionalization procedure, non-dimensional parameters and elemental matrices of the finite element model of the rotor-bearing system are provided in the Appendix 1. Mathematical relation between Sommerfeld number and mass parameter is provided in Appendix 2. A sample MATLAB program for time-transient analysis of the rotor-bearing system is given in Appendix 3.

CHAPTER 2

Mathematical Formulation

2.0 Introduction

The basic equations of a rotor-bearing system are provided in this chapter. The equation of motion of the flexible rotor is derived from the finite element formulation of Timoshenko Beam Theory [116]. The governing equations of the porous oil journal bearing are the modified Reynolds equation [21, 38] along with Darcy's equation. The finite element formulation of the rotor is presented in the following section. Further, a non-dimensionalization scheme for the rotor-bearing system equation of motion has also been presented.

2.1 Assumptions

In the mathematical modelling of the rotor-bearing system the following simplifying assumptions are made:

- The rotor-bearing system is horizontal.
- The rotor is supported by two identical porous bearings. Bearings are placed symmetrically at the extreme ends of the shaft unless otherwise stated.
- The cavitation boundary condition of the bearing is based upon Reynolds boundary condition.
- A disk mass is mounted on the mid-span of the shaft. The only source of unbalance is due to disk eccentricity.
- The effect of shaft misalignment and the corresponding bearing moments are neglected.
- It is assumed that as compared to translational motion of the shaft, axial motion is negligible.
- Non-linearity in the rotor-bearing system is due to the bearings only.

2.2 Finite Element Formulation of the Rotor

There are many techniques that have been employed for designing rotating system and for obtaining the dynamic response of rotor. One of the most popular methods is the finite element method in which the rotor body is discretized into a finite number of elements.

Three different beam models may be used in the finite element analysis and they are,

- Euler-Bernoulli Beam
- Rayleigh Beam
- Timoshenko Beam

In Euler-Bernoulli Beam theory, only pure bending energy is considered. In this theory it is assumed that the cross-sectional area remains plane after bending and the elastic axis is perpendicular to the cross-sectional area. In case of Rayleigh Beam, in addition to translational kinetic energy cross-sectional rotational kinetic energy is considered which is called rotary inertia. In Timoshenko beam theory shear strain energy is also taken into account; due to the shear force the cross-section of the beam element no longer remains normal no the elastic axis. As a matter of fact, Timoshenko beam theory incorporates both shear strain energy and rotary inertia. In the present analysis, Timoshenko beam theory has been used. The gyroscopic effects are also considered. The Elemental matrices in equation of motion are obtained by Extended Hamilton's principle in accordance with the finite element formulation.

A uniform shaft of length L rotating at constant speed Ω and simply supported on two bearings is shown in Fig. 2.1 with the two primary reference systems which are utilized to describe its motion. The (XYZ) triad is a fixed reference with the X axis coinciding with the un-deformed centreline of the shaft. The $(X'Y'Z')$ triad rotates at a uniform rate Ω about the Z axis.

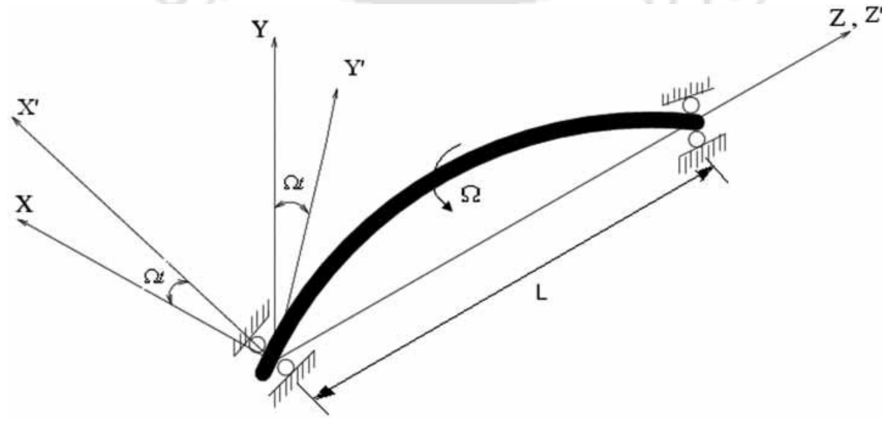

Fig. 2.1: Geometry of the rotor-bearing system

The shaft is discretized into a finite number of two-noded elements. The element is considered to be initially straight and is modelled as eight degree of freedom element: two translations and two rotations at each node. The cross-section of the element is circular and is considered to be uniform. For a typical element of the shaft, in a deformed state, located at a distance z from the left end can be described by two translations in X and Y-directions as well as the small rotations about X and Y axes. The translations of the cross-section are due to bending and shear. The relationships can be expressed as,

$$\begin{aligned} &V(z,t)=V_b(z,t)+V_s(z,t)\\ &W(z,t)=W_b(z,t)+W_s(z,t)\\ &\mathrm{B}(z,t)=-\frac{\partial W_b(z,t)}{\partial z}\\ &\Gamma(z,t)=\frac{\partial V_b(z,t)}{\partial z}\end{aligned} \tag{2.1}$$

where $V_b, V_s \,\&\, W_b, W_s$ are translations due to bending and shear in the Y and X directions respectively. The two rotations, B and Γ are only influenced by bending deformations.

The potential energy, U^e of a rotating shaft element of length l consists of elastic bending energy and shear deformation energy and is given by,

$$U^e=\frac{1}{2}\int_0^l EI\left\{\left(B'\right)^2+\left(\Gamma'\right)^2\right\}dz+\frac{1}{2}\int_0^l \kappa GA\left\{\left(V_s'\right)^2+\left(W_s'\right)^2\right\}dz \tag{2.2}$$

where the prime denotes differential with respect to axial distance z, E the Young's modulus, I the second moment of inertia, κ the shear coefficient, G the shear modulus, A the cross-sectional area of the shaft, and

$$\begin{aligned} &V_s'=\frac{\partial V}{\partial z}-\Gamma\\ &\mathrm{W}_s'=\frac{\partial W}{\partial z}+B \end{aligned}\;. \tag{2.3}$$

The elemental kinetic energy T^e of a shaft element of length l rotating at a constant speed Ω including the translational and rotary kinetic energy can be expressed as,

$$T^e=\frac{1}{2}\int_0^l \rho A\left\{\left(\dot{V}\right)^2+\left(\dot{W}\right)^2\right\}dz+\frac{1}{2}\int_0^l I_d\left\{\left(\dot{B}\right)^2+\left(\dot{\Gamma}\right)^2\right\}dz-\Omega\int_0^l I_p\left(\dot{\Gamma}\right)B\,dz+\frac{\Omega^2}{2}\int_0^l I_p\,dz \tag{2.4}$$

where dot represents differentiation with time, ρ density of the material, I_p and I_d are polar and diametral moment of inertia per unit length respectively.

In the finite element procedure, each element has two nodes and each node has four degrees of freedom: two translations and two rotations. The nodal displacement vector is given by,

$$\{q\}^e = \{V_1 \quad W_1 \quad B_1 \quad \Gamma_1 \quad V_2 \quad W_2 \quad B_2 \quad \Gamma_2\}^T . \tag{2.5}$$

The nodal displacement field of an element e can be approximated as follows,

$$\{V(z,t) \quad W(z,t) \quad B(z,t) \quad \Gamma(z,t)\} = \sum_{i=1}^{2} N_i(z)\{V_i \quad W_i \quad B_i \quad \Gamma_i\} \tag{2.6}$$

where $N_i(z)$ is the one-dimensional Lagrangian shape function.

The translational and rotational displacement fields can be expressed by the following matrix form,

$$\begin{Bmatrix} V \\ W \end{Bmatrix} = \left[N_t(z)\right]\{q\}^e = \begin{bmatrix} N_v(z) \\ \hline N_w(z) \end{bmatrix}\{q\}^e \tag{2.7}$$

and $$\begin{Bmatrix} B \\ \Gamma \end{Bmatrix} = \left[N_b(z)\right]\{q\}^e = \begin{bmatrix} N_\beta(z) \\ \hline N_\gamma(z) \end{bmatrix}\{q\}^e . \tag{2.8}$$

In the above expression $N_t(z)$ and $N_b(z)$ are the translational and rotational shape function matrices respectively.

Equation (2.3) is related to Eqns. (2.7) and (2.8) as follows,

$$\begin{Bmatrix} V_s' \\ W_s' \end{Bmatrix} = \begin{bmatrix} [N_v]' - [N_\gamma] \\ \hline [N_w]' + [N_\beta] \end{bmatrix}\{q\}^e = \left[N_s(z)\right]\{q\}^e \tag{2.9}$$

Using Eqns. (2.7), (2.8) and (2.9), the element potential and kinetic energy can be expressed in terms of nodal displacement vectors as given below,

$$U^e = \frac{1}{2}\{q\}^{eT}\left([K_b]^e + [K_s]^e\right)\{q\}^e = \frac{1}{2}\{q\}^{eT}[K]^e\{q\}^e \tag{2.10}$$

and

$$T^e = \frac{1}{2}\{\dot{q}\}^{eT}\left([M_T]^e + [M_R]^e\right)\{\dot{q}\}^e - \Omega\{\dot{q}\}^{eT}[H]^e\{\dot{q}\}^{eT} + \frac{1}{2}I_p\Omega^2 \tag{2.11}$$

where

$$[K_b]^e = \int_0^l [N_b]'^T EI [N_b]' dz \, ; \; [K_s]^e = \int_0^l [N_s]^T \kappa GA [N_b] dz$$

$$[M_T]^e = \int_0^l [N_t]^T \rho A [N_t] dz \; ; \; [M_T]^e = \int_0^l [N_b]^T I_d [N_b] dz$$

$$[H]^e = \int_0^l \left[N_\gamma\right]^T I_p \left[N_\beta\right] dz$$

The matrix equation of motion for a shaft element *e* is obtained by substituting the element potential energy and element kinetic energy given by Eqns (2.10) and (2.11) respectively, into Hamilton's principle:

$$\left([M_T]^e + [M_R]^e\right)\{\ddot{q}\}^e - \Omega [G]^e \{\dot{q}\}^e + [K]^e \{q\}^e = \{F\}^e \tag{2.12}$$

where $[G]^e = [H]^e - [H]^{eT}$ is the shaft element gyroscopic matrix and $[K]^e = [K_b]^e + [K_s]^e$ is the element stiffness matrix.

The equation of motion for a disk attached to rotor is given by,

$$\left[M^d\right]^e \left\{\ddot{q}^d\right\}^e - \Omega \left[G^d\right]\left\{\dot{q}^d\right\} = \left\{F^d\right\}_{unb} \tag{2.13}$$

where $\left[M^d\right]$ is the disk mass matrix and $\left[G^d\right]$ is the disk gyroscopic matrix.

2.3 Non-dimensionalization of the System Equation of Motion

The following non-dimensional scheme is introduced,

$\bar{z} = \dfrac{z}{C}$, $\bar{l} = \dfrac{l}{C}$, $\bar{v} = \dfrac{v}{C}$, $\bar{w} = \dfrac{w}{C}$, $\bar{t} = \Omega t$, $\bar{F} = \dfrac{F}{W}$ where, $W = \dfrac{(\rho A L + m_d)\, g}{2}$ is the load per bearing.

With the substitution of the above non-dimensional scheme the elemental equation of motion of the rotor in non-dimensional terms can be written as,

$$\left(\left[\bar{M}_T\right]^e + \left[\bar{M}_R\right]^e\right)\{\ddot{\bar{q}}\}^e - \left[\bar{G}\right]^e \{\dot{\bar{q}}\}^e + \left[\bar{K}\right]^e \{\bar{q}\}^e = \{\bar{F}\}^e \tag{2.14}$$

Similarly, equation of motion of the disk in non-dimensional terms is given by,

$$\left[\bar{M}^d\right]\left\{\ddot{\bar{q}}^d\right\} - \left[\bar{G}^d\right]\left\{\dot{\bar{q}}^d\right\} = \left\{\bar{F}^d\right\}_{unb} \tag{2.15}$$

where $\left\{\bar{F}^d\right\}_{unb}$ is the vector of unbalance forces due to the disk eccentricity.

The system equation of motion of the rotor is arrived at by assembling the elemental equations and would be as follows:

$$\left[\bar{M}\right]\left\{\ddot{\bar{q}}\right\} - \left[\bar{G}\right]\left\{\dot{\bar{q}}\right\} + \left[\bar{K}\right]\left\{\bar{q}\right\} = \left\{\bar{F}\right\} \tag{2.16}$$

In the system equation of motion, Eqn. (2.16), the right hand side is the force vector consisting of hydrodynamic forces at the bearing ends and unbalance forces due to the disk eccentricity. The non-dimensional forces at the bearing locations can be expressed as,

$$\bar{F}_Y = -\bar{F}_\phi^B \pi S \sin\phi - \bar{F}_r^B \pi S \cos\phi - 1$$

$$\bar{F}_X = \bar{F}_\phi^B \pi S \cos\phi - \bar{F}_r^B \pi S \sin\phi .$$

The non-dimensional unbalance forces at the disk location are given by,

$$\bar{F}_Y^d = 2\left(\frac{C\Omega^2}{g}\right)\left(\frac{e_d}{C}\right)\left(\frac{\bar{m}_d}{1+\bar{m}_d}\right)\sin\bar{t}$$

$$\bar{F}_X^d = 2\left(\frac{C\Omega^2}{g}\right)\left(\frac{e_d}{C}\right)\left(\frac{\bar{m}_d}{1+\bar{m}_d}\right)\cos\bar{t} .$$

The details of non-dimensional matrices and forces are given in the Appendix 1.

2.4 Hydrodynamic Porous Oil Journal Bearing

Oil-impregnated porous bearings are manufactured by powder metallurgy process. Porous bearings are widely used in light machines such as, computers, domestic appliances, electric motors, sewing machines, printing and packaging machines etc. Porous bearings have the advantage that it can be placed in interior places where refilling of lubricant is difficult as the porous bush acts as an oil reservoir.

2.4.1 Governing Equations

A hydrodynamic porous oil journal bearing is shown in the Fig. 2.2. A porous bush made of sintered material is inserted inside a solid housing. The flow through the porous bush and the clearance space is assumed to be viscous and laminar. The bearings operate under hydrodynamic lubrication conditions in the initial stages of their life cycle when the pores are filled with oil. But they operate under mixed or boundary lubrication when the pores are starved of oil due to oil leakage or during the start-up/shut-down condition of the rotor. However, only the hydrodynamic lubrication condition is considered in this present work.

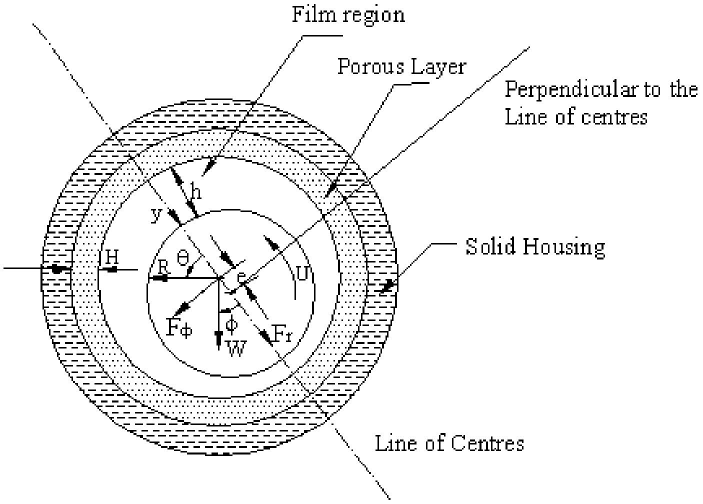

Fig. 2.2: Porous Bearing Geometry

Oil flow through the porous bush is assumed to obey Darcy's law [21, 38] and is given by,

$$k_x \frac{\partial^2 p'}{\partial x^2} + k_y \frac{\partial^2 p'}{\partial y^2} + k_z \frac{\partial^2 p'}{\partial z^2} = 0 \tag{2.17}$$

Flow through the clearance space is governed by modified Reynolds equation [21, 38], as given below

$$\frac{\partial}{\partial x}\left[\frac{h^3}{\eta}\frac{\partial p}{\partial x}\right] + \frac{\partial}{\partial z}\left[\frac{h^3}{\eta}\frac{\partial p}{\partial z}\right] = 6\frac{\partial h}{\partial x} - 12\left(\frac{\partial \phi}{\partial t}\right)\left(R\frac{\partial h}{\partial x}\right) + 12\frac{\partial h}{\partial t} + 12\frac{k_y}{\eta}\left(\frac{\partial p'}{\partial y}\right)_{y=0} \tag{2.18}$$

With the following substitutions,

$$\bar{p}' = \frac{\bar{p}' C^2}{\eta UR}; \bar{p} = \frac{pC^2}{\eta UR}; \bar{y} = \frac{y}{H}; \bar{z} = \frac{2z}{L_B}; \bar{h} = \frac{h}{C}; \bar{t} = \Omega t; \mathrm{K}_x = \frac{k_x}{k_y}; \mathrm{K}_z = \frac{k_z}{k_y}; \theta = \frac{x}{R}$$

the Eqns. (2.17) and (2.18) can be reduced to dimensionless form as follows

$$\mathrm{K}_x \frac{\partial^2 \bar{p}'}{\partial \theta^2} + \left(\frac{R}{H}\right)^2 \frac{\partial^2 \bar{p}'}{\partial \bar{y}^2} + \left(\frac{D}{L_B}\right)^2 \mathrm{K}_z \frac{\partial^2 \bar{p}'}{\partial \bar{z}^2} = 0 \tag{2.19}$$

$$\frac{\partial}{\partial\theta}\left[\bar{h}^3\frac{\partial\bar{p}}{\partial\theta}\right]+\left(\frac{D}{L_B}\right)^2\frac{\partial}{\partial\bar{z}}\left[\bar{h}^3\frac{\partial\bar{p}}{\partial\bar{z}}\right]=6\frac{\partial\bar{h}}{\partial\theta}-12\left(\frac{\partial\phi}{\partial\bar{t}}\right)\left(\frac{\partial\bar{h}}{\partial\theta}\right)+12\frac{\partial\bar{h}}{\partial\bar{t}}+\beta\left(\frac{\partial\bar{p}'}{\partial\bar{y}}\right)_{\bar{y}=0} \qquad (2.20)$$

where $\beta=\frac{12k_yR^2}{C^3H}$ is the porous bearing feeding parameter.

2.4.2 Boundary Conditions

The boundary conditions for the porous bearing are as follows:

2.4.2.1 For the porous media

$$\bar{p}'(\theta,\bar{y},\bar{z})=\bar{p}'(\theta+2\pi,\bar{y},\bar{z})\ \text{(circular)}$$

$$\bar{p}'(\theta,\bar{y},\pm1)=0\ \text{(ambient)}$$

$$\frac{\partial\bar{p}'}{\partial\bar{z}}(\theta,\bar{y},0)=0\ \text{(symmetric)}$$

$$\frac{\partial\bar{p}'(\theta,-1,\bar{z})}{\partial\bar{y}}=0\ \text{(solid casing)}$$

2.4.2.2 For the film-region

$$\bar{p}(\theta,\bar{z})=\bar{p}(\theta+2\pi,\bar{z})\ \text{(circular)}$$

$$\bar{p}(\theta,\pm1)=0\ \text{(ambient)}$$

$$\frac{\partial\bar{p}(\theta,0)}{\partial\bar{z}}=0\ \text{(symmetric)}$$

$$\left.\begin{aligned}\frac{\partial\bar{p}(\theta_2,\bar{z})}{\partial\theta}&=0\\ \bar{p}(\theta_2,\bar{z})&=0\end{aligned}\right\}\ \text{(cavitation boundary condition)}$$

2.4.2.3 For porous bush-film interface

$$\bar{p}'(\theta,0,\bar{z})=\bar{p}(\theta,\bar{z})$$

The film cavitation zone is determined by applying the Reynolds boundary conditions, $\frac{\partial\bar{p}(\theta_2,\bar{z})}{\partial\theta}=0$ and $\bar{p}(\theta_2,\bar{z})=0$ where θ_2 is the angular extent at which cavitation starts. In the numerical iteration whenever the pressures at any grid point becomes negative, it is made equal to zero and further iterations are carried out. This process can satisfy the Reynolds boundary conditions as shown by Christopherson [120] and therefore, this method has been applied in the present investigation. The film formation boundary in the present analysis is not well defined as the Reynolds boundary condition applied by using the Cristopherson algorithm ensures only the location of the cavitation start, θ_2.

The non-dimensional bearing forces along the radial and the circumferential directions are given by,

$$\begin{aligned} \bar{F}_r^{B} &= -\int_0^1 \int_0^{\theta_2} \bar{p} \cos\theta \, d\theta \, d\bar{z} \\ \bar{F}_\phi^{B} &= \int_0^1 \int_0^{\theta_2} \bar{p} \sin\theta \, d\theta \, d\bar{z} \end{aligned} \tag{2.21}$$

The bearing forces along the circumferential and radial directions are obtained by simultaneously solving the modified Reynolds equation and Darcy's equation satisfying the boundary conditions for pressure in a finite difference grid and then integrating pressure distribution over the clearance space. The Gauss-Sidel iteration method is adopted to solve the equations numerically. A successive over-relaxation scheme is used to accelerate the convergence of the iteration and to obtain the pressure distribution. The number of grids used in the iteration scheme is 60x16x24 along the circumferential, radial and axial directions respectively. It has been ensured by number of trials that increasing the grid densities further does not improve the accuracy of the solution significantly. The hydrodynamic bearing forces are obtained by double integrating the pressure distribution along the circumferential and the axial directions by using the Simpson's 1/3rd rule.

2.5 Time Transient Analysis

Let $\bar{v}_b$ and $\bar{w}_b$ denote the non-dimensional horizontal and vertical deflection of the rotor respectively at the bearing location. From the rotor-bearing geometry, $\bar{v}_b = -\varepsilon \sin\phi$ and $\bar{w}_b = -\varepsilon \cos\phi$. Therefore,

$$\left.\begin{aligned} \varepsilon &= \sqrt{\bar{v}_b^2 + \bar{w}_b^2} \\ \phi &= \tan^{-1}\left(\frac{\bar{v}_b}{\bar{w}_b}\right) \\ \dot{\varepsilon} &= -(\dot{\bar{v}}_b \sin\phi + \dot{\bar{w}}_b \cos\phi) \\ \dot{\phi} &= -\frac{(\dot{\bar{v}}_b \cos\phi - \dot{\bar{w}}_b \sin\phi)}{\varepsilon} \end{aligned}\right\} \tag{2.22}$$

These values of ε, $\dot{\varepsilon}$, $\dot{\phi}$ are substituted in Eqn. (2.20) to calculate the bearing forces for each time-step. The non-dimensional equation of motion as given in Eqn. (2.16) of the rotor is solved numerically by Wilson-θ method for translational and rotational displacement, velocity and acceleration at each nodal point and thereby eccentricity ratio and attitude angle of the bearing and their derivatives are estimated at every time step by using Eqn. (2.22). These derivatives are then used in time-dependent Reynolds equation for the calculation of hydrodynamic force components for the next time step. Thus, displacement, velocity and acceleration of rotor at different nodal points of the rotor can be obtained. Trajectories of the journal centre at different nodes are drawn by plotting ε and ϕ for a period of time.

2.6 Non-dimensional Parameters

In the non-dimensionalization method (Appendix 1) of the rotor-bearing system the following non-dimensional parameters are obtained:

$\frac{L_B}{D}$ = aspect ratio of the bearing

$\frac{e}{C}$ = eccentricity ratio of the bearing

$\frac{H}{R}$ = thickness ratio of the bearing

β = bearing feeding parameter

$\frac{R}{C}$ = clearance ratio of the bearing

$\frac{R}{2L}$ = slenderness ratio of the rotor

$\frac{E}{\rho g L}$ = stiffness parameter of the rotor

$\frac{m_d}{\rho A L}$ = ratio of disk mass to shaft mass

$\frac{e_d}{C}$ =eccentricity of the disk mass

$\frac{C\Omega^2}{g}$ = mass parameter

The last parameter is named as mass parameter following the standard nomenclature of mass parameter, $\bar{m} = \frac{mC\Omega^2}{W}$, [21, 38]. However, substituting $W = mg$, this parameter takes the form $\bar{m} = \frac{C\Omega^2}{g}$. It is noteworthy to mention that in the non-dimensional scheme used in the present analysis, two new parameters have been obtained, namely, stiffness parameter, $\frac{E}{(\rho g L)}$ and ratio of disk mass to shaft mass, $\frac{m_d}{(\rho A L)}$.

2.7 Summary

In the present chapter, the non-dimensional equation of motion of the rotor based on Timoshenko beam theory is presented. The unbalance and hydrodynamic force components acting on the rotor are also provided. Stability, non-linear dynamic response and bifurcation analysis of the rotor is carried out in the following chapters based on the equation of motion presented in this chapter. The Mass parameter, $\bar{m} = \frac{C\Omega^2}{g}$, a function of the speed of the rotor, is taken as the control parameter. Dynamic behaviour of the rotor-bearing system changes with the change in mass parameter when other non-dimensional rotor-bearing parameters remain same. A parametric study is carried out and the effect of the above parameters on stability, non-linear dynamic response and bifurcation characteristics is then investigated.

CHAPTER 3

Stability Analysis of Flexible Rotor Supported on Finite Hydrodynamic Porous Journal Bearing using Non-linear Transient Method

---

3.0 Introduction

A theoretical analysis has been carried out to study the stability of flexible rotor supported on two symmetrical finite porous oil journal bearings at the two ends. The rotor is modelled by Timoshenko Beam theory as presented in the previous chapter. An attempt has been made to investigate the stability characteristics using a non-linear transient method in this chapter. This analysis enables to trace the journal centre locus at different locations of the rotor. The bearing location journal centre trajectories are presented initially in this chapter since the main focus is to estimate the sub-synchronous critical parameters. Trajectories at other locations then follow. Several trajectories of the journal centre have been presented for different operating conditions. The present work has been carried out in non-dimensional form as given in detail in the previous chapter. The effects of Sommerfeld number, bearing feeding parameter, bearing aspect ratio, clearance ratio, slenderness ratio and material properties of the shaft on stability are also investigated. Further, the effect of the ratio of disk mass to shaft mass and the location of bearings has also been provided.

3.1 Mathematical Model

A fully balanced horizontal rotor is considered in the derivation of the mathematical model of the rotor-bearing system as shown in Fig. 3.1. The rotor is descretized into a finite number of elements. The equations of motion are obtained in accordance with the finite element formulation as described in the previous chapter. The only forces acting on the rotor are the hydrodynamic forces and the weight of the rotor.

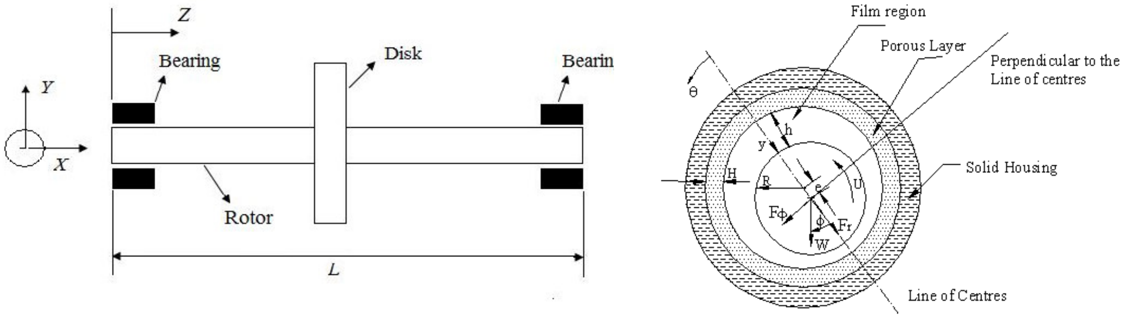

Fig 3.1: Rotor Supported on Fluid Film Bearings

The non-dimensional system equation of motion of a flexible rotor supported by the two identical bearings at the two ends is given by the following equation as shown in chapter 2,

$$\left[\bar{M}\right]\{\ddot{\bar{q}}\}-\left[\bar{G}\right]\{\dot{\bar{q}}\}+\left[\bar{K}\right]\{\bar{q}\}=\{\bar{F}\} \tag{3.1}$$

where, $\left[\bar{M}\right]$ stands for assembled mass matrix, $\left[\bar{G}\right]$ stands for assembled gyroscopic matrix, $\left[\bar{K}\right]$ stands for assembled stiffness matrix, $\{\bar{F}\}$ stands for force vector and $\{\bar{q}\}$ denotes displacement vector.

In the RHS of Eqn. (3.1) the force vector consists of hydrodynamic force components in *X* and *Y* direction and the gravitational load at the bearing locations as given below,

$$\begin{aligned}\bar{F}_Y &= -\bar{F}_\phi^B \pi S \sin\phi - \bar{F}_r^B \pi S \cos\phi - 1\\ \bar{F}_X &= \bar{F}_\phi^B \pi S \cos\phi - \bar{F}_r^B \pi S \sin\phi\end{aligned} \tag{3.2}$$

3.2 Stability Analysis

Following the method explained in section 2.5, a number of trajectories have been obtained for different mass parameters while other rotor-bearing parameters are kept constant. Stability behaviour is predicted by observing the journal centre trajectory. Initially the journal centre equilibrium position is perturbed from its static equilibrium position. A bearing is considered unstable if this trajectory grows continuously, tending to reach the clearance circle. If the journal centre trajectory traverses over a loop, the bearing is said to be in critically stable condition. When the trajectory spirals in and regains the static equilibrium position, then the bearing is said to be stable. This process is repeated for numbers of time for different values of mass parameter, $\bar{m}$ until critically stable trajectories are obtained.

3.3 Results and Discussions

Some comparisons of critical mass parameters ($\bar{m}_{cr}$) are given in the following table considering both finite bearing solution and approximate (short or long bearing) solutions. The following non-dimensional parameters are considered for the comparison: $E/(\rho gL) = 1.35\times10^5$, $\bar{m}_d = 0.0$, $R/2L = 0.0125$, $\beta = 0.0$, $L_B/D = 1.0$.

The percentage errors are given in parenthesis. A maximum of 9.9% difference is observed in case of short bearing approximation and a maximum of 9.6% difference is observed in case of long bearing approximation. It has also been observed that the error limit is significant in some cases. Therefore, it is necessary to incorporate finite bearing model for a more reliable results.

Table 3.1: Comparison of critical mass parameter with different bearing models

Eccentricity ratio (ε)	Critical Mass Parameter ($\bar{m}_{cr}$)		
	Finite Bearing	Short Bearing	Long Bearing
0.2	2.1	2.0 (5%)	2.23 (6.1%)
0.3	2.17	2.12 (2.3%)	2.31 (6.45%)
0.4	2.25	2.16 (4%)	2.40 (6.67%)
0.5	2.39	2.26 (5.4%)	2.57 (7.5%)
0.6	2.74	2.52 (8%)	2.97 (8.4%)
0.7	3.85	3.47 (9.9%)	4.22 (9.6%)

Some examples of stable, critical and unstable journal centre trajectories at the bearing locations are presented in Figs. 3.2a, 3.3a and 3.4a for L_B/D=1.0, H/R=0.2, R/C=500, β=0.03, ε=0.5, $R/2L$=0.0125 and $E/(\rho gL) = 2.7\times10^6$. Corresponding non-dimensional time responses (both vertical and horizontal) are shown in Figs. 3.2b, 3.3b and 3.4b. The corresponding mass parameter values are indicated in the figure captions.

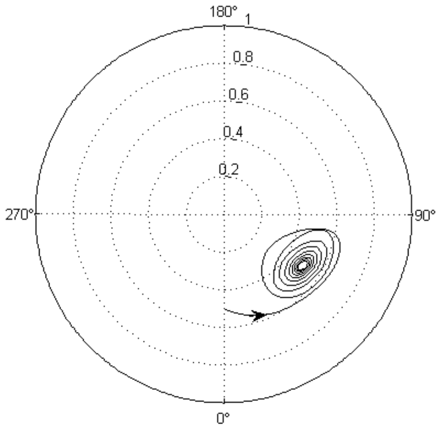

Fig. 3.2a: Trajectory of journal centre at the bearing location (stable), $\overline{m}$ =2.6

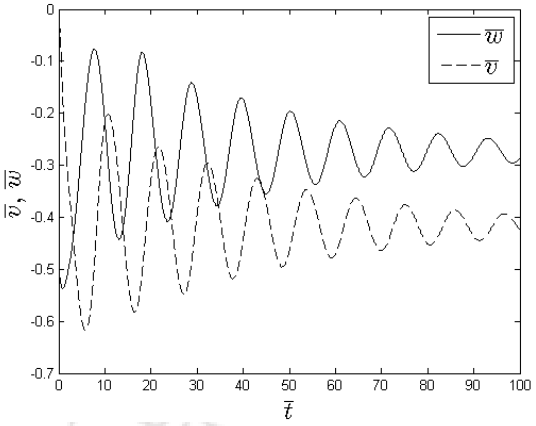

Fig. 3.2b: Vertical and Horizontal displacement vs. time of the journal centre at bearing location, $\overline{m}$ =2.6

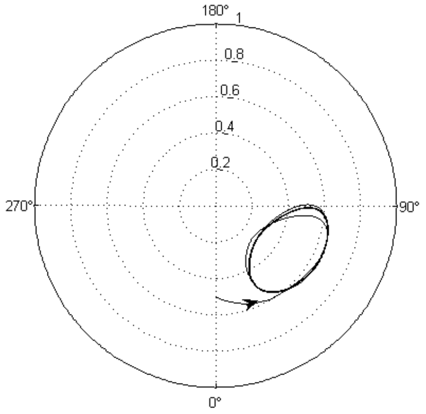

Fig. 3.3a: Trajectory of journal centre at the bearing location (critical), $\overline{m}$ =3.4

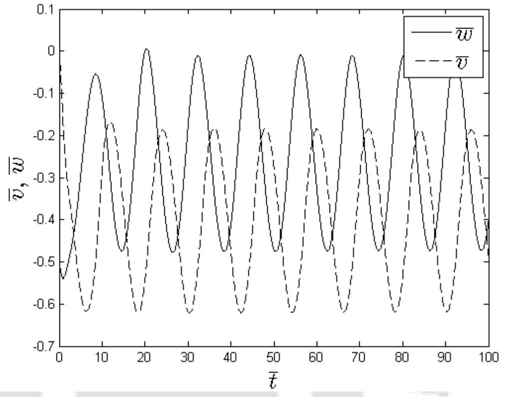

Fig. 3.3b: Vertical and Horizontal displacement vs. time of the journal centre at bearing location, $\overline{m}$ =3.4

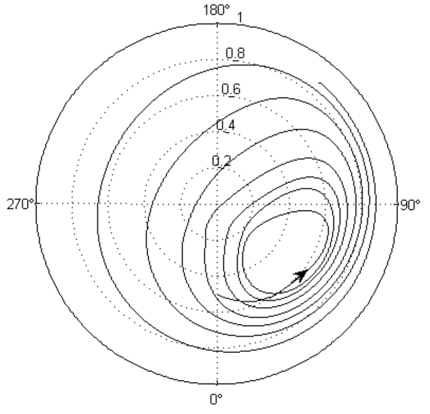

Fig. 3.4a: Trajectory of journal centre at the bearing location (unstable), $\overline{m}$ =4.2

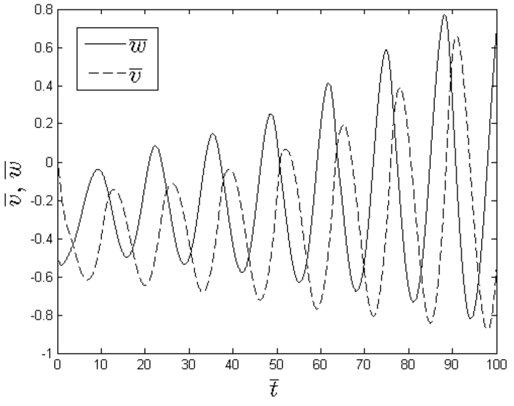

Fig. 3.4b: Vertical and Horizontal displacement vs. time of the journal centre at bearing location, $\overline{m}$ =4.2

The critical mass parameter at which journal centre traverses in a closed loop has been shown in Fig. 3.3a and corresponding amplitudes in both the transverse directions are shown in Fig. 3.3b. It may be observed that for this case the amplitude of vibration in vertical and horizontal direction does not change. Mass parameter values lower than the critical value gives stable locus. The trajectory spirals in and the amplitude of vibration decreases with time as observed in Figs. 3.2a and 3.2b respectively. Further, the journal centre grows continuously and amplitude of vibration increases as depicted in Figs. 3.4a and 3.4b respectively at mass parameter values higher than the critical value. The rotor becomes unstable at such mass parameters.

From Fig. 3.3b, the non-dimensional time period for whirling is found to be $\bar{T}_P = \Omega T_P$=12.39. Whirling frequency is given by, $\omega = \frac{2\pi}{T_P} = \frac{2\pi}{\bar{T}_P / \Omega}$. Therefore whirl ratio is estimated as $\frac{\omega}{\Omega} = \frac{2\pi}{\bar{T}_P}$=0.5071. This fact can also be ascertained from the FFT-spectrum of vertical and horizontal rotor displacement at the bearing location as shown in Figs. 3.5a and 3.5b respectively. It has been observed from the Figs. 3.5a-b that the peak is at $\frac{\omega}{\Omega}$ =0.5. This implies that the whirling frequency is half of the rotor spin speed. Therefore, the whirling phenomenon studied here is nothing but the half-frequency whirling, which is a common feature in case of fluid film bearings.

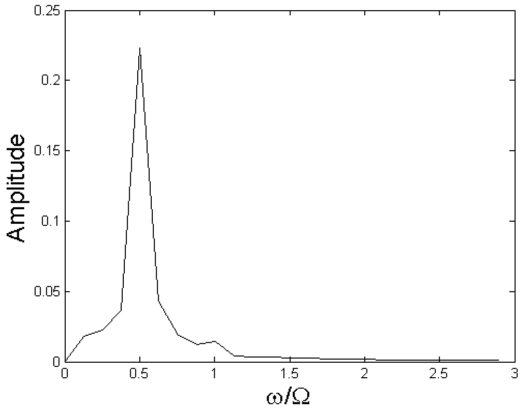

Fig. 3.5a: FFT-spectrum of vertical displacement at bearing location at $\bar{m}$ =3.4

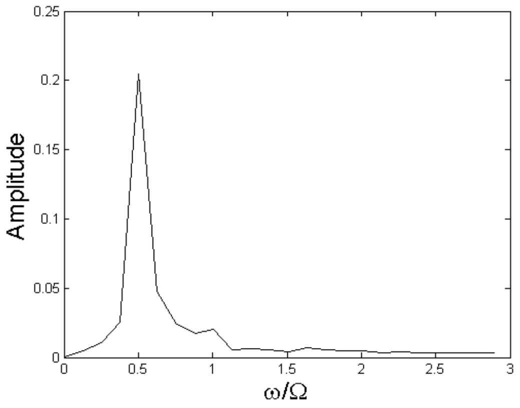

Fig. 3.5b: FFT-spectrum of horizontal displacement at bearing location at $\bar{m}$ =3.4

Similarly, journal centre trajectories and the responses are obtained at the rotor mid location when $\bar{m}$ =2.6, 3.4 and 4.2. The corresponding plots are shown in Figs.

3.6a through 3.8b. The other non-dimensional parameters are the same as mentioned above. Here also it may be observed that the journal centre trajectory at the rotor mid-location is stable at $\bar{m}$=2.6 (Fig. 3.6a), critically stable at $\bar{m}$=3.4 (Fig. 3.7a) and unstable at $\bar{m}$=4.2 (Fig. 3.8a).

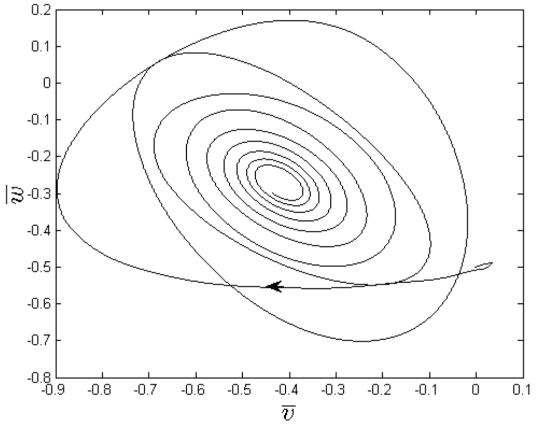

Fig. 3.6a: Trajectory of journal centre at the rotor mid location (stable), $\bar{m}$=2.6

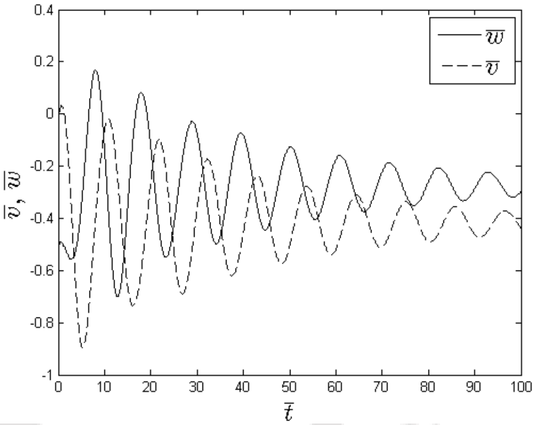

Fig. 3.6b: Vertical and Horizontal displacement vs. time of the journal centre at rotor mid location, $\bar{m}$=2.6

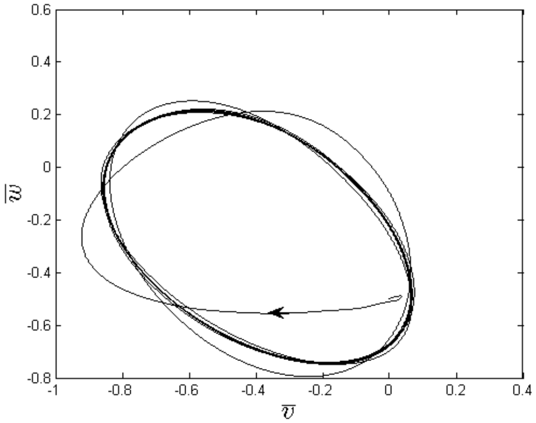

Fig. 3.7a: Trajectory of journal centre at the rotor mid location (critical), $\bar{m}$=3.4

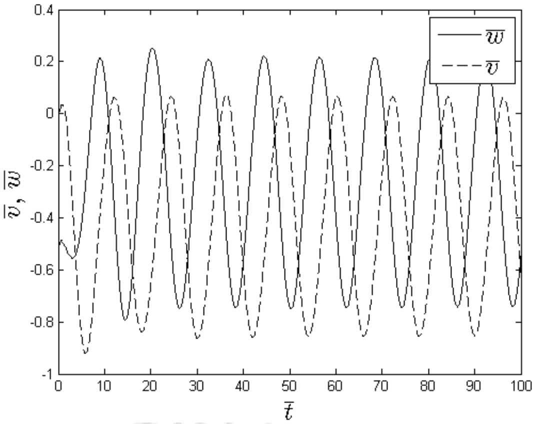

Fig. 3.7b: Vertical and Horizontal displacement vs. time of the journal centre at rotor mid location, $\bar{m}$=3.4

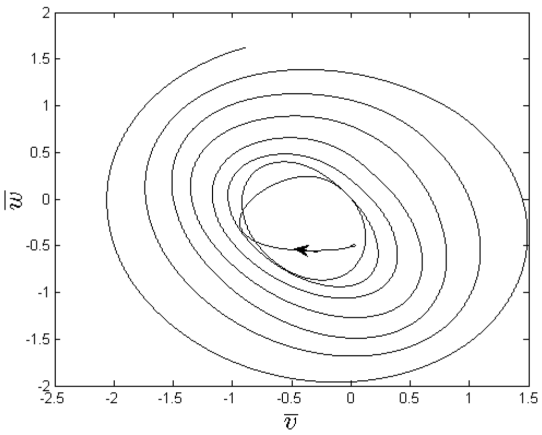

Fig. 3.8a: Trajectory of journal centre at the rotor mid location (unstable), $\bar{m}$ =4.2

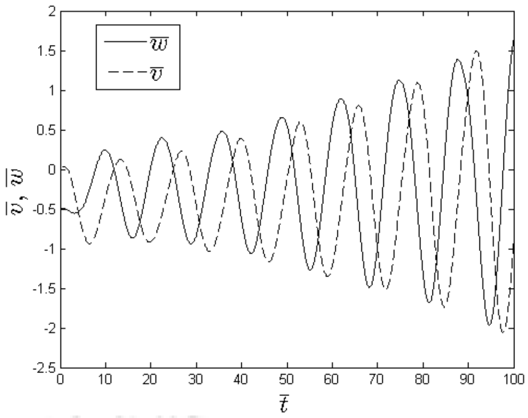

Fig. 3.8b: Vertical and Horizontal displacement vs. time of the journal centre at rotor mid location, $\bar{m}$ =4.2

The FFT-spectra of the rotor vertical and horizontal displacement at the rotor mid location at $\bar{m}$ =3.4 are shown in Figs. 3.9a and 3.9b. It is evident from Figs. 3.9a-b that the motion is sub-synchronous.

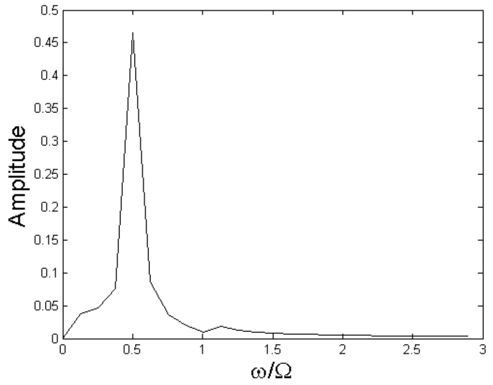

Fig. 3.9a: FFT-spectrum of vertical displacement at rotor mid location at $\bar{m}$ =3.4

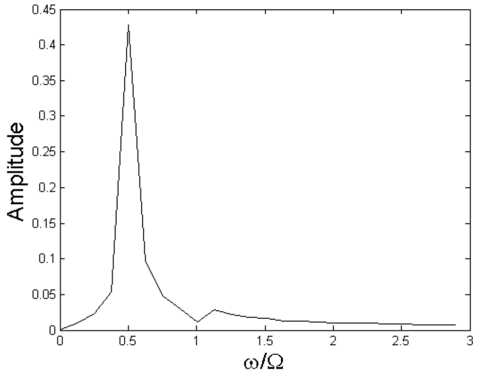

Fig. 3.9b: FFT-spectrum of horizontal displacement at rotor mid location at $\bar{m}$ =3.4

Journal centre trajectories at five nodes throughout the length of the rotor system are shown in Fig. 3.10a, 3.10b and 3.10c for $\bar{m}$=4.0, 5.33 and 6.0 respectively. The shaft trajectories are shown at the element numbers 1, 3, 5, 7 and 9. It may be observed that the nature of the trajectory (i.e. stable, critically stable or unstable) remains same throughout the length of the rotor. It may be mentioned that scaled up views of the trajectories are presented in Figs. 3.10 a, b and c. for clarity.

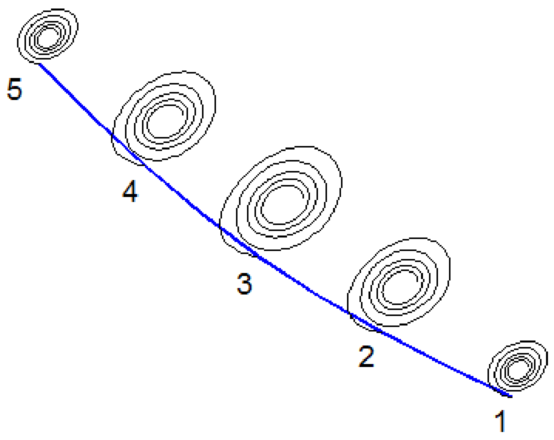

Fig. 3.10a: Rotor transient motion at $\bar{m}$ =2.6

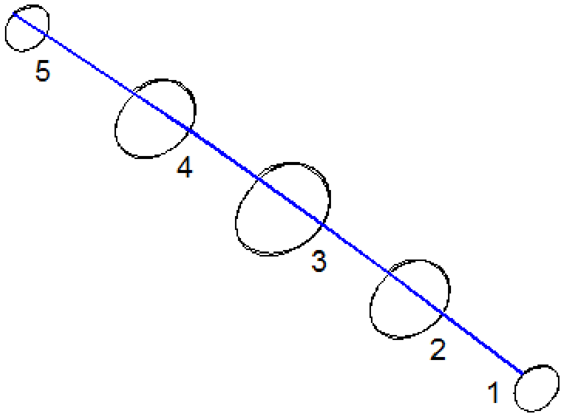

Fig. 3.10b: Rotor transient motion at $\bar{m}$ =3.4

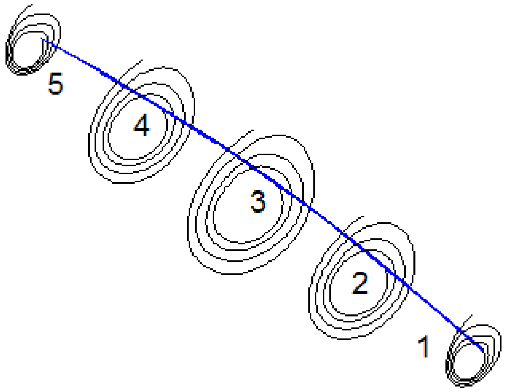

Fig. 3.10c: Rotor transient motion at $\bar{m}$ =4.2

It was observed earlier [31] that for high values of slenderness ratio (above 0.067) the flexible rotor threshold speed approaches rigid rotor threshold speed. Therefore, in the present analysis the critical mass parameters of flexible rotor with sufficiently high value of slenderness ratio (0.067) are compared with those of rigid rotor in Figs. 3.11-3.12. It is noticed that the results are very close at different eccentricity ratios (Fig. 3.11) as well as Sommerfeld numbers (Fig. 3.12) for bearing feeding parameters of 0.0 (plain bearing), 0.03 and 0.06. On the other hand this validates the methodology adopted here as the results with the present approach for higher slenderness ratio of 0.067 are close to those predicted using rigid rotor model.

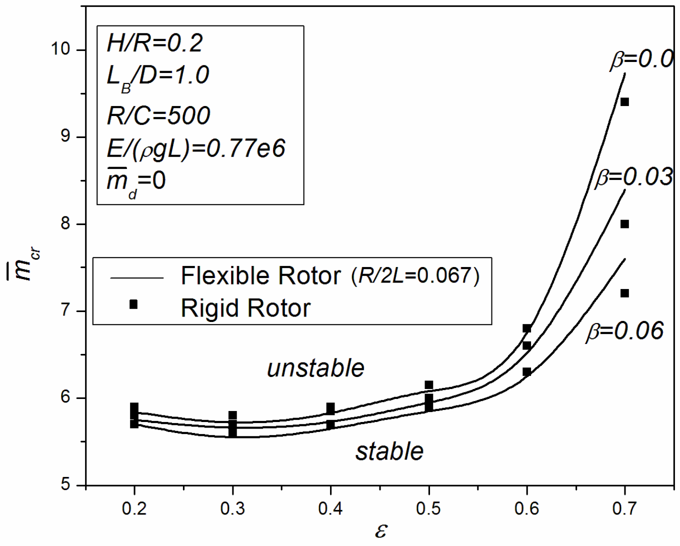

Fig. 3.11: Stability map ($\bar{m}_{cr}$ versus ε) for different bearing feeding parameter (β) using flexible rotor and rigid rotor

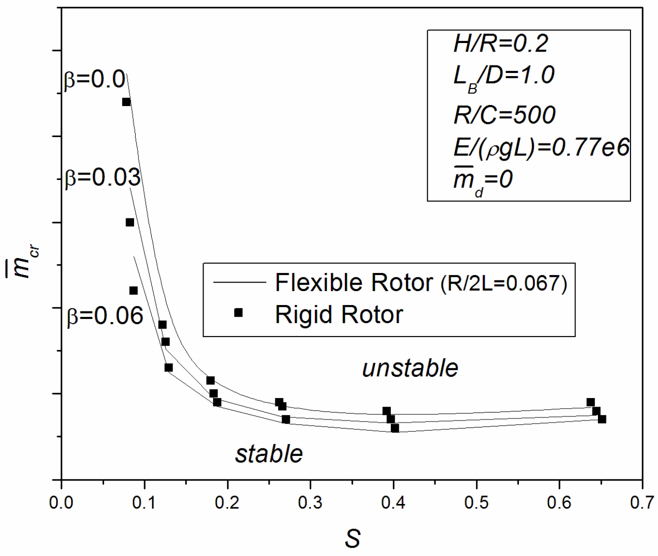

Fig. 3.12: Stability map ($\overline{m}_{cr}$ versus *S*) for different bearing feeding parameter (β) using flexible rotor and rigid rotor

3.3.1 Effect of Eccentricity Ratio of Bearing

Eccentricity ratio ε plays an important role in the margin of stability. It has been observed from Fig. 3.11 that for values of $\varepsilon \leq 0.3$, an increase in eccentricity ratio results in slight deterioration of stability. However, for $\varepsilon > 0.3$, it is found that stability improves with eccentricity ratio of bearing for all feeding parameters considered in the present work.

3.3.2 Effect of bearing feeding parameter

As shown in Fig. 3.11, three different feeding parameters are considered in the present investigation. It has been observed that with an increase in bearing feeding parameter, β, the stability margin reduces with decrease in $\overline{m}_{cr}$ for all eccentricity ratios. It may be attributed to the reason that higher porosity in the bearing results in deterioration of stability. Higher porosity means higher leakage will be there and this results in reduction of load capacity and thereby deterioration of stiffness of the bearing. Further, when β=0.0, the porous oil bearing reduces to plain journal bearing. Thus, it may be concluded that, plain journal bearings have better stability than porous bearings.

3.3.3 Effect of Sommerfeld number

Critical mass parameter may be plotted versus Sommerfeld number also as demonstrated in Fig. 3.12 for different bearing feeding parameters. It may be noticed that up to S=0.4, there is a decrease in $\bar{m}_{cr}$ with an increase in Sommerfeld no. However, for S>0.4 stability remains unaffected with the increase in Sommerfeld no. The notion, stability is a concern for lightly loaded bearing is substantiated by the results shown in Figs. 3.11 and 3.12.

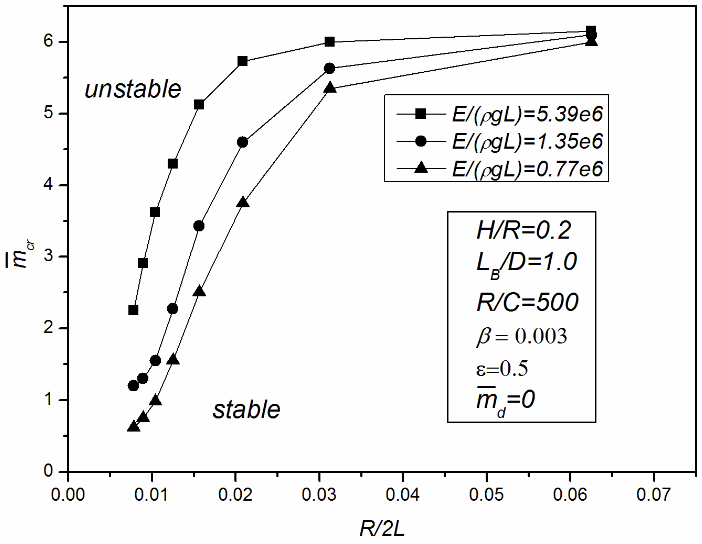

Fig. 3.13: Stability map ($\bar{m}_{cr}$ versus $R/2L$) for different values of stiffness parameter, $E/(\rho gL)$

3.3.4 Effect of Slenderness Ratio

Slenderness ratio is an important parameter in the stability analysis of flexible rotor. To investigate its effect, critical mass parameters of different rotors with different slenderness ratios at eccentricity ratio 0.5 have been estimated and plotted as shown in Fig. 3.13 for three different values of $E/(\rho gL)$. It has been observed from this figure that critical mass parameter increases with an increase in slenderness ratio. This implies that stability is poor for more flexible rotor and critical mass parameter value approaches those for rigid rotor for higher slenderness ratio.

3.3.5 Effect of Stiffness Parameter

In the present study a new parameter is introduced as stiffness parameter, which is defined as $E/(\rho g L)$. It has been observed that this parameter also plays an important role in stability of flexible rotor. The parameter depends upon the material properties and length of the rotor. In Fig. 3.13 critical mass parameter is plotted against slenderness ratio for different values of $E/(\rho g L)$. With an increase in $E/(\rho g L)$, stability of the rotor-bearing system improves. It has also been noticed that at high value of slenderness ratio ($R/2L$=0.0625) the critical mass parameter is almost same for all values of $E/(\rho g L)$, which is also nearly equal to the rigid rotor critical mass parameter.

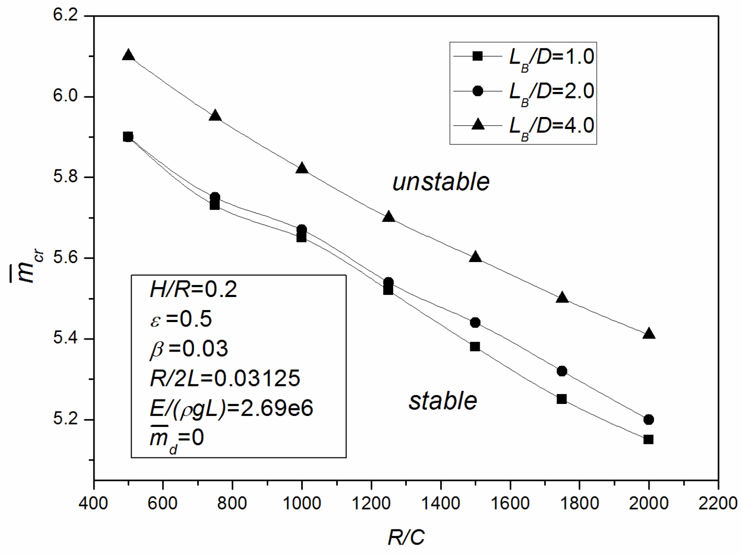

Fig. 3.14: Stability map ($\bar{m}_{cr}$ versus *R/C*) for different values of bearing aspect ratio, L_B/D

3.3.6 Effect of Clearance Ratio of the Bearing

Figure 3.14 depicts the variation of critical mass parameter against clearance ratio of the bearing for three different values of bearing aspect ratio. It may be observed that with the increase of clearance ratio critical mass parameter decreases for all values of bearing aspect ratio. Thus, it may be concluded that higher the clearance ratio, poor is the stability of the rotor.

3.3.7 Effect of Bearing Aspect Ratio

Bearing aspect ratio L_B / D is another important non-dimensional parameter which affects the stability of the rotor. In Fig. 3.14, the variation of critical mass parameter is plotted against clearance ratio for three different values of bearing aspect ratio L_B / D =1.0, 2.0 and 4.0. It can be seen from Fig. 3.14 that with the increase of L_B / D, critical mass parameter values increases. Therefore, it may be concluded that stability of the rotor-bearing system improves with the increase of bearing aspect ratio.

3.3.8 Effect of Ratio of Disk Mass to Shaft Mass

Rotors in general have a number of accessories attached with it such as gears, pulleys etc. Stability of rotor-bearing assembly system significantly depends on the mass of these accessories. In the present study, the effect of disk masses on the stability is analyzed. The disk masses are mounted at the rotor mid-location. Fig. 3.15 shows the variation of critical mass parameter against Sommerfeld number for three different values of the ratio of disk mass to shaft mass, $\overline{m}_d$ =15, 35 and 55. It can be observed that with increase in $\overline{m}_d$, critical mass parameter decreases. Therefore, it may be concluded that with increase in ratio of disk mass to shaft mass, threshold speed of stability decreases.

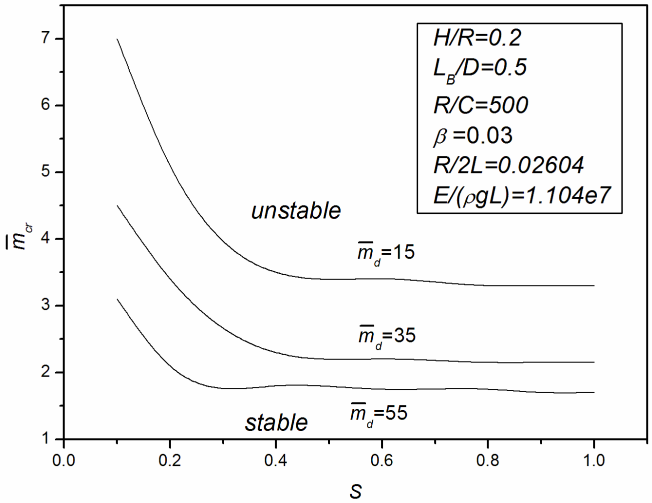

Fig. 3.15: Stability map ($\overline{m}_{cr}$ versus *S*) for different values of ratio of disk mass to shaft mass, $\overline{m}_d$

3.3.9 Effect of Location of Bearings

In the above discussion (sub-sections 3.3.1 through 3.3.8), the bearings are positioned at the extreme ends (i.e., at nodes 1 and 15) of the shaft. Now, it has been proposed to study the stability characteristics of rotor by changing the bearing locations. In view of this, the shaft is divided into 14 elements as shown in Fig. 3.16 and the two bearings are symmetrically located at node numbers 1 and 15, 2 and 14, 3 and 13 and so on. The variation of critical mass parameter with the change in location of the bearings is tabulated in Table 3.1 for three different slenderness ratios $R/2L=$ 0.00625, 0.0083 and 0.0125. Other rotor-bearing parameters are $E/(\rho gL)=2.69\times10^{6}$, $m_d/(\rho AL)=0.0$, $\varepsilon=0.5$, $\beta=0.03$, $H/R=0.2$, $L_B/D=1.0$ and $R/C=500$.

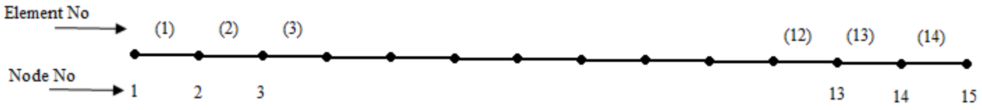

Fig. 3.16: Element and Node number of the shaft

Table 3.2: Variation of critical mass parameter ($\overline{m}_{cr}$) with bearing location

Bearing Location Node Numbers	Critical Mass Parameter ($\overline{m}_{cr}$)		
	$R/2L$=0.00625	$R/2L$=0.0083	$R/2L$=0.0125
1-15	0.8	1.7	3.4
2-14	1.2	2.5	4.3
3-13	2.3	3.7	5.4
4-12	3.4	5.4	5.9
5-11	4.1	5.8	6.1
6-10	3.0	4.5	5.8
7-9	2.0	3.5	5.2

It has been observed from Table 3.1 that as the bearings are placed more inside from the extreme ends of the shaft, the stability improves. Stability is the lowest when the bearings are placed at the extreme ends of the shaft (node numbers 1 and 15). Highest stability is obtained when the bearings are placed at node numbers 5 and 11 for all values of slenderness ratio. However, if the bearings are placed at further inside than this location then stability slightly deteriorates as it can be observed from Table 3.1 that critical mass parameter decreases when the bearings are placed at nodes 6-10 and 7-9. Thus, observing the Table 3.1, it may be inferred that overhung shafts have better stability characteristics.

3.4 A Case Study

The above analysis is carried out in a non-dimensional form. To demonstrate how a rotor-bearing problem with known geometry and other properties can be dealt with the non-dimensional results presented in this chapter has been provided in this section.

Let the threshold speed of a rotor-bearing system described by Rao [121] (page 212, Example 8.1) be estimated. The rotor-bearing geometry and properties are given in Table 3.2:

Table 3.3: Rotor-bearing data for simulation

Mass of rotor system (Disk mass+shaft mass), M	54.432 kg
Shaft stiffness for Jeffcott rotor, K	1.387×10^7 N/m
Length of bearing, L_B	1.27 cm
Diameter of bearing, D	2.54 cm
Bearing Clearance, C	0.00254 cm
Oil Viscosity, η	0.0242 Pa-s

Instead of 4 axial groove bearings in the said example, isotropic porous bearings with $\beta = 0.03$ and $H/R = 0.2$ have been considered. It has also been assumed that the shaft is made of steel with density, $\rho = 7830$ kg/m^3 and modulus of elasticity, $E = 2.07\times10^{11}$ N/m^2. Shaft stiffness for Jeffcott rotor is given by, $K = \frac{48EI}{L^3}$. Therefore, length of the shaft has been found to be, L=0.244 m. Mass of the disk has been found to be, $m_d = M - \rho\frac{\pi}{4}D^2L = 53.46$ kg.

Having all the required data, the non-dimensional parameters have been estimated as follows:

L_B / D=0.5, H / R=0.2, R / C=500, β=0.03, $R / 2L$=0.02604, $E/(\rho g L) = 1.104\times10^7$, $\overline{m}_d$=55.23 (say 55) and S=0.7.

To estimate the threshold speed, the corresponding critical mass parameter has to be known. The non-dimensional parameter values pertaining to the problem correspond to the results presented in Fig. 3.15. Critical mass parameter has been obtained from this plot for S=0.7 and $\overline{m}_d$=55, which is, $\overline{m}_{cr} = \frac{C\Omega_{cr}^2}{g}$=1.7. Having known the critical mass parameter, the threshold speed has been found to be, Ω_{cr}=810 rad/s or Ω_{cr}=7738 rpm.

This example demonstrates how such problems can be resolved in a very simple way utilizing the presented results.

3.5 Summary

A non-linear time transient analysis has been carried out for a flexible rotor supported on two identical hydrodynamic porous bearings in the present study. The methodology adopted results in plotting of journal centre trajectory at different locations of the rotor. However, only the trajectories in the bearing locations are taken up in the present work. The investigation is noteworthy in the sense that critical mass parameter, which is a function of spin speed of rotor, can be estimated for different non-dimensional rotor-bearing parameters such as bearing aspect ratio, Sommerfeld number, bearing feeding parameter, clearance ratio, slenderness ratio of rotor and newly introduced stiffness parameter. The methodology and the results presented here would be highly useful for rotor-bearing analysts.

The following conclusion may be drawn from the above analysis:

- An increase in slenderness ratio results in improved stability of the rotor.
- Higher the stiffness parameter, the better is the stability.
- Permeability of the porous bush adversely affects the stability of rotor-bearing system. High permeability results in deterioration of stability.
- Threshold of stability increases with the decrease in Sommerfeld number.
- Higher the clearance ratio, poor is the stability of the rotor.
- Stability of the rotor-bearing system improves with the increase of bearing aspect ratio.
- Stability deteriorates with increase in the ratio of disk mass to shaft mass.

- Overhung rotors are more stable than rotors supported at the ends.

It is worth mentioning here that due to the bending and shear effect, there is a possible misalignment of the rotor and therefore, the boundary conditions of the bearings at both the ends may be different from those considered in this work. This issue may be addressed later for better prediction of flexible rotor-bearing system as it is not within the scope of the present work.

CHAPTER 4

Non-linear Dynamic Analysis of an Unbalanced Flexible Rotor Supported on Porous Oil Journal Bearings

---

4.0 Introduction

In the present chapter the non-linear dynamic analysis of a flexible rotor with a rigid disk under unbalance excitation mounted on porous oil journal bearings at the two ends is carried out. It is assumed that the non-linearity in the system is due to the bearings only. The system equation of motion is obtained by finite element formulation of Timoshenko Beam and the disk as provided in chapter 2. The non-linear oil-film forces are calculated from the solution of the modified Reynolds equation simultaneously with Darcy's equation. The system equation of motion is then solved by Wilson-θ method. The results have been presented and effects of different parameters have been discussed in the previous chapter without considering unbalance of the rotor. To carry out non-linear dynamic analysis, a small unbalance is introduced to the rotor in this chapter. Three-dimensional Waterfall diagrams are generated to study the dynamics of the rotor-bearing system during start-up and shut-down.

Further, Bifurcation diagrams, Poincaré maps, time response, journal trajectories and FFT-spectrum etc. are obtained to study the non-linear dynamics of the rotor-bearing system. It is shown that the system undergoes Hopf bifurcation as the speed increases. The effects of various non-dimensional rotor-bearing parameters on the non-linear dynamic behaviour of the system have been investigated. Some insights about improving instability problem of rotor-bearing system are obtained by varying these parameters

4.1 Equation of Motion

A simple rotor model with a disk at the mid-point of the rotor is assumed for mathematical modelling of the system as shown in Fig. 3.1. The rotor-disk system is supported by two porous oil journal bearings at the extreme ends.

The elemental equation of motion of a rotor element in non-dimensional form is given by [116],

$$\left(\left[\bar{M}_T\right]^e+\left[\bar{M}_R\right]^e\right)\left\{\ddot{\bar{q}}\right\}^e-\left[\bar{G}\right]^e\left\{\dot{\bar{q}}\right\}^e+\left[\bar{K}\right]^e\left\{\bar{q}\right\}^e=\left\{\bar{F}\right\}^e \tag{4.1}$$

The non-dimensional equation of motion of the disk is,

$$\left[\bar{M}^d\right]\left\{\ddot{\bar{q}}^d\right\}-\left[\bar{G}^d\right]\left\{\dot{\bar{q}}^d\right\}=\left\{\bar{F}^d\right\}_{unb} \tag{4.2}$$

where $\left\{\bar{F}^d\right\}_{unb}$ is the vector of unbalance forces due to the disk eccentricity.

The system equation of motion of the rotor is arrived at by assembling the elemental equations and would be as follows:

$$\left[\bar{M}\right]\left\{\ddot{\bar{q}}\right\}-\left[\bar{G}\right]\left\{\dot{\bar{q}}\right\}+\left[\bar{K}\right]\left\{\bar{q}\right\}=\left\{\bar{F}\right\} \tag{4.3}$$

In the system equation of motion, Eqn. (4.3), the right hand side is the force vector consisting of hydrodynamic forces at the bearing ends and unbalance forces due to the disk eccentricity. The non-dimensional forces at the bearing locations has been expressed as,

$$\begin{aligned}\bar{F}_Y &= -\bar{F}_\phi^B \pi S \sin\phi - \bar{F}_r^B \pi S \cos\phi - 1\\ \bar{F}_X &= \bar{F}_\phi^B \pi S \cos\phi - \bar{F}_r^B \pi S \sin\phi.\end{aligned} \tag{4.4}$$

where S is the Sommerfeld number.

The non-dimensional unbalance forces at the disk location are given by,

$$\begin{aligned}\bar{F}_Y^d &= 2\left(\frac{C\Omega^2}{g}\right)\left(\frac{e_d}{C}\right)\left(\frac{\bar{m}_d}{1+\bar{m}_d}\right)\sin\bar{t}\\ \bar{F}_X^d &= 2\left(\frac{C\Omega^2}{g}\right)\left(\frac{e_d}{C}\right)\left(\frac{\bar{m}_d}{1+\bar{m}_d}\right)\cos\bar{t}.\end{aligned} \tag{4.5}$$

4.2 Solution Procedure

The system equation of motion Eqn. (4.3) is solved by Wilson-θ method and the governing equations for the bearing are solved by Gauss-Seidel iteration method with successive over-relaxation. The detailed solution procedure is given in section 2.5. In each integration cycle, initial time-series data for first 200 revolutions of the rotor are not used for dynamic behaviour investigation, thereby guaranteeing the data being used is steady-state as was done by Chen and Yau [73].

Waterfall diagrams are spectrum plots taken over a range of speeds of a machine, such as during start-up or shut-down. Waterfall diagrams relate the rotor spin speed, amplitude of vibration and whirl frequency in a 3-D plot.

Bifurcation diagrams are obtained by taking the mass parameter as the control parameter. Bifurcation diagrams are generated by plotting the variation of $\bar{v}(n\bar{T})$ and $\bar{w}(n\bar{T})$ coordinates of the return Poincaré map against the mass parameter.

In the analysis, mass parameter is incremented with a constant step. The state variables at the end of one integration cycle are taken as the initial condition for the next mass parameter. Sommerfeld number varies with the variation of mass parameter. Sommerfeld number varies with the mass parameter by the following relation: if S_1 and S_2 are two Sommerfeld numbers and $\bar{m}_1$ and $\bar{m}_2$ are the corresponding mass parameters then, $\frac{S_1^2}{S_2^2} = \frac{\bar{m}_1}{\bar{m}_2}$ (Appendix 2).

4.3 Results and Discussion

4.3.1 Validation

To validate the present model developed in this paper, waterfall diagram for a rotor-bearing system described by Castro *et al.* [37] is generated and compared as shown in Figs. 4.1. The properties of the rotor-bearing configuration considered in [37] are tabulated below for a quick reference.

Table 4.1: Rotor-bearing data for simulation

Distance between the two bearings	600 mm
Diameter of the shaft	12mm
Mass of the Disk	2.34 kg
Young's Modulus	2.067E11 Pa
Density	7800 kg/m^3
Unbalance moment	2E-5 kg-m
Bearing Clearance	90 μm
Oil Viscosity	0.04 Pa-s
Diameter of the Bearing	0.031 m

In the present model the porous bearing reduces to plain journal bearing when $\beta = 0.0$. The essential dynamics of the rotor has been studied from the waterfall diagram at the bearing location. The resonance frequency of the rotor is about 22 Hz. From the waterfall diagram, it has been observed that the synchronous vibration due to the unbalance has highest magnitude around 22 Hz and when the shaft rotation reaches nearly 44 Hz, which is twice the resonance frequency, severe vibration due to oil whip is observed. It may be observed that the waterfall diagram generated with the present methodology [Fig. 4.1(c)] matches quite well with the published experimental [Fig. 4.1(a)] as well as simulated [Fig. 4.1(b)] results (Fig. 19-20 in [36]) to capture the salient features of rotor-bearing vibration. As the methodology adopted is found to be valid, it has been proposed to study the effects of slenderness ratio, stiffness parameter and bearing feeding parameter on the dynamic behaviour of a rotor-bearing system as described in the following sections.

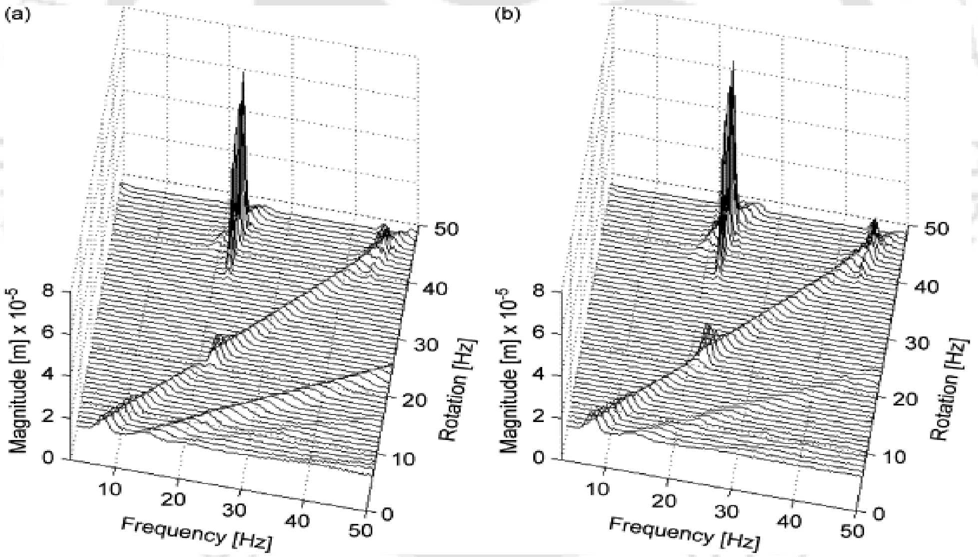

Fig. 4.1(a): Experimental waterfall diagram for (a) horizontal displacement and (b) vertical displacement ref. [37]

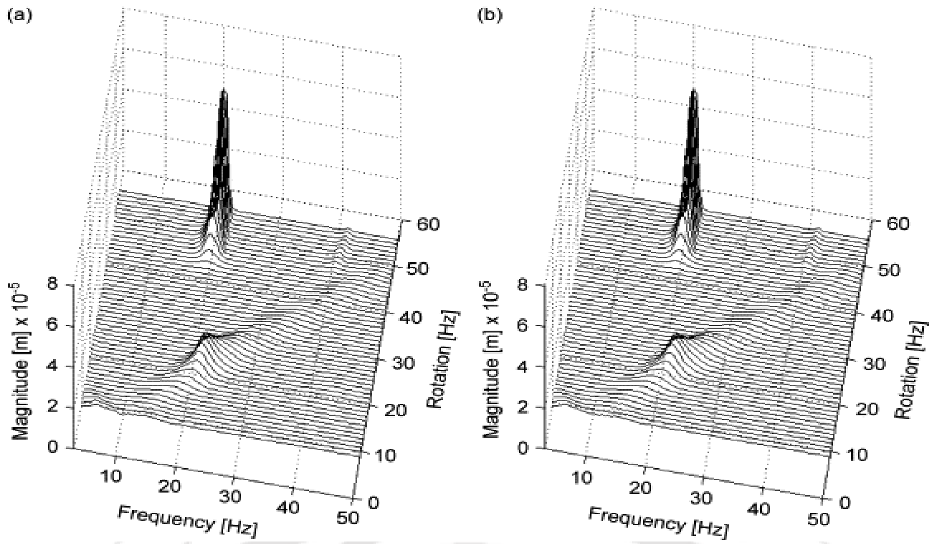

Fig. 4.1(b): Simulated waterfall diagram for (a) horizontal displacement and (b) vertical displacement ref. [37]

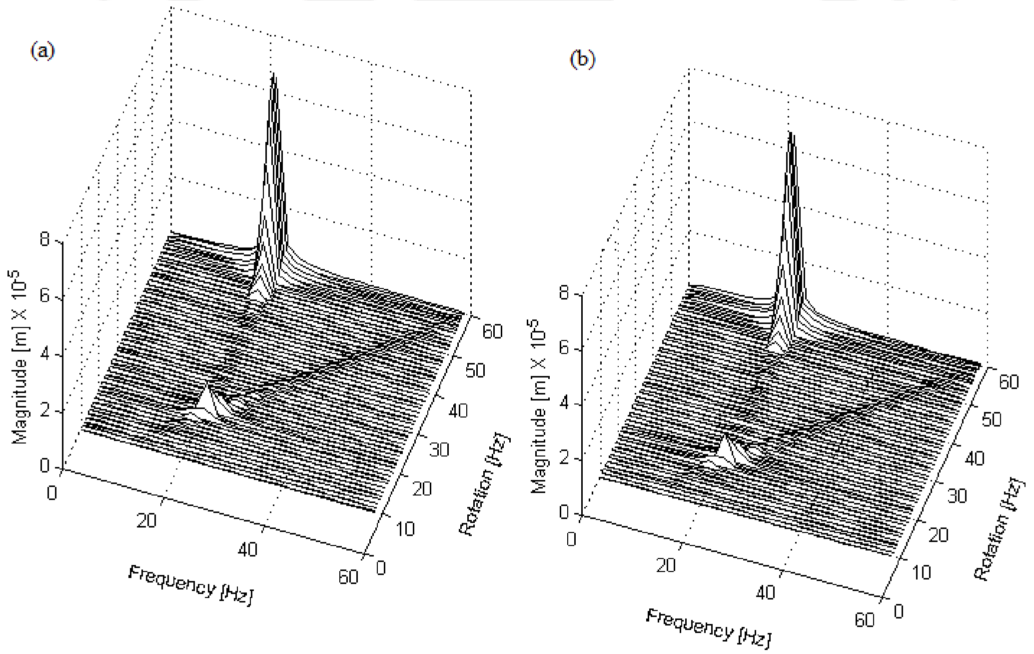

Fig. 4.1(c): Simulated waterfall diagram for (a) horizontal displacement and (b) vertical displacement with present methodology

4.3.2 Journal Centre Trajectory and Responses

For a given set of parameters of the rotor-bearing systems, $\frac{R}{2L}$=0.0125, $\frac{E}{(\rho g L)}=2.7\times10^{6}$, β=0.03, $\frac{L_B}{D}$=1.0, $\frac{m_d}{(\rho A L)}$=0.25 and $\frac{e_d}{C}$=0.25 a number of trajectories, responses and FFT-spectrum are obtained by varying the mass parameter. The nature of the trajectories and responses are studied as the mass parameter is increased. Trajectories, responses and FFT-spectra of the rotor-bearing system at the bearing location and disk location are shown in Figs. 4.2a-4.10b for three different values of mass parameter, $\overline{m}$=1.0, 2.0 and 3.0. When $\overline{m}$=1.0 the trajectory and responses are regular (Fig.4.2a-b, 4.5a-b) and only one peak is observed at ω/Ω =1.0 in the FFT spectra (Fig. 4.8a-b). This is due to the unbalance force. However, at $\overline{m}$=2.0 one more peak appears at ω/Ω=0.5 (Fig. 4.9a-b). This peak appears because of sub-synchronous whirl due the hydrodynamic forces. In this case trajectories and responses are asynchronous. When $\overline{m}$=3.0, the sub-synchronous whirl amplitude due to oil film is much higher than unbalance amplitude (Fig. 4.10a-b). It may be observed from Fig. 4.7a-b that at higher values of mass parameter vis-à-vis spin speed the bearing forces become so large that the rotor-bearing system becomes unstable as the amplitude of vibration grows with time. Corresponding trajectories (Fig. 4.4a-b) also indicate instability in the system. In view of these results, it may be inferred that at lower values of mass parameter the unbalance forces are dominant in the dynamic behaviour, however, at moderate values of mass parameter both the bearing forces and the unbalance forces are dominant. However, at higher values of the mass parameter the bearing forces are more dominant than the unbalance forces and can induce instability in the system.

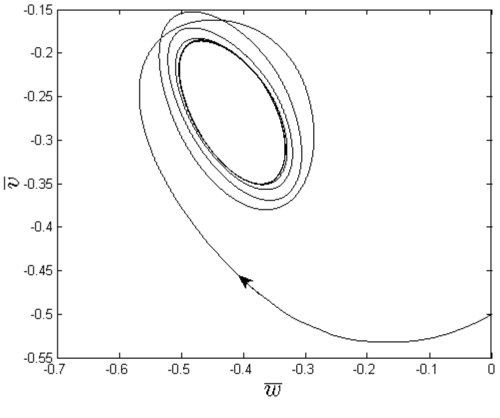

Fig. 4.2a: Trajectory at the bearing location at $\overline{m}$=1.0

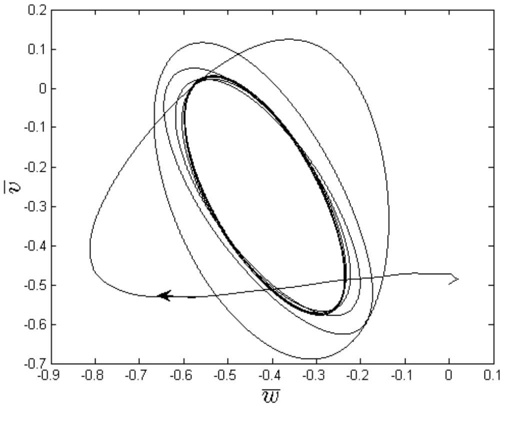

Fig. 4.2b: Trajectory at the disk location at $\overline{m}$=1.0

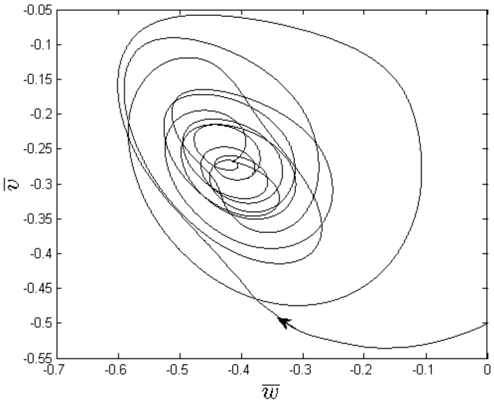

Fig. 4.3a: Trajectory at the bearing location at $\overline{m}$ =2.0

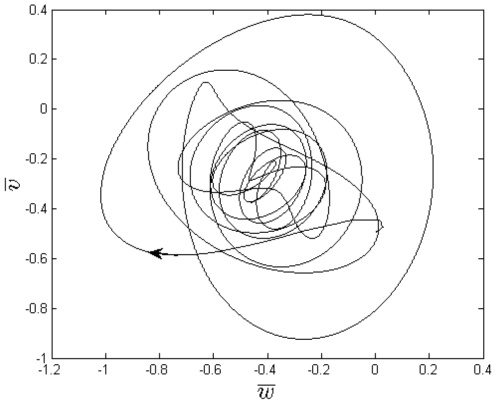

Fig. 4.3b: Trajectory at the disk location at $\overline{m}$ =2.0

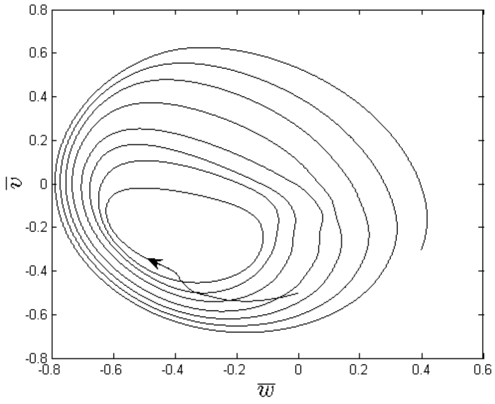

Fig. 4.4a: Trajectory at the bearing location at $\overline{m}$ =3.0

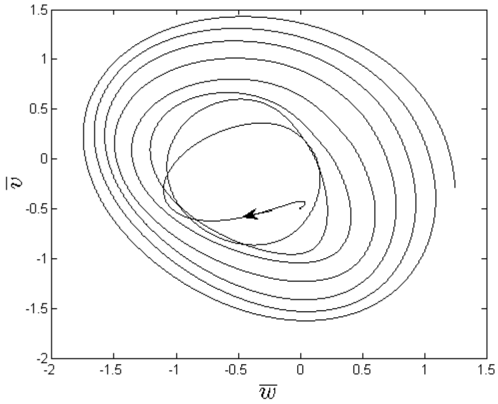

Fig. 4.4b: Trajectory at the disk location at $\overline{m}$ =3.0

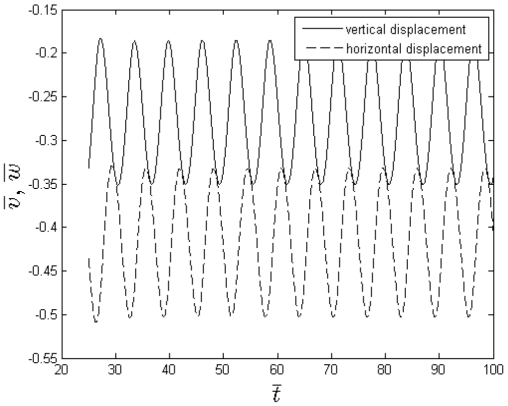

Fig. 4.5a: Response at the bearing location at $\overline{m}$ =1.0

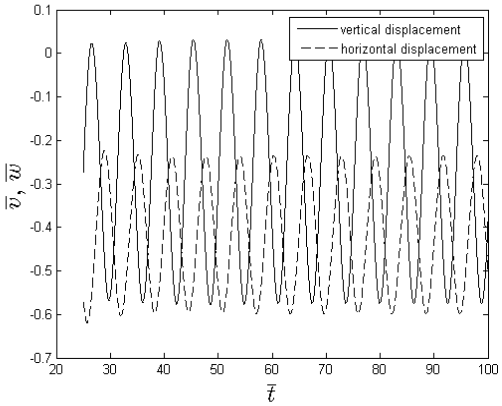

Fig. 4.5b: Response at the disk location at $\overline{m}$ =1.0

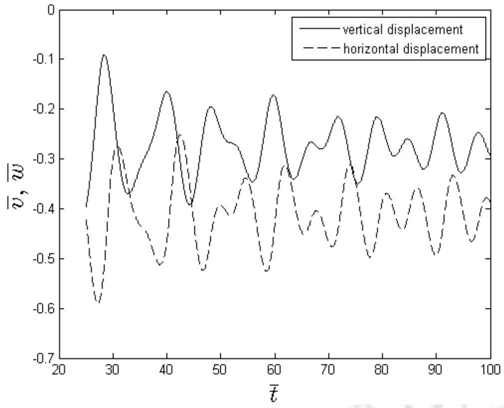

Fig. 4.6a: Response at the bearing location at $\overline{m}$ =2.0

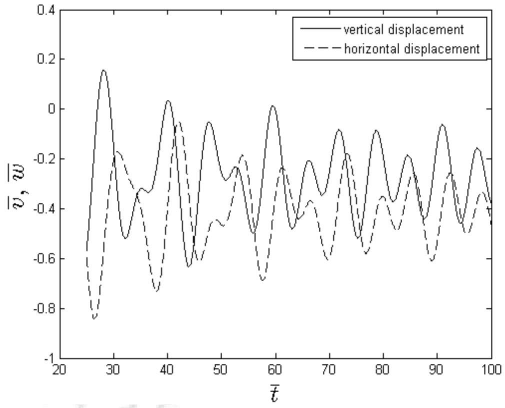

Fig. 4.6b: Response at the disk location at $\overline{m}$ =2.0

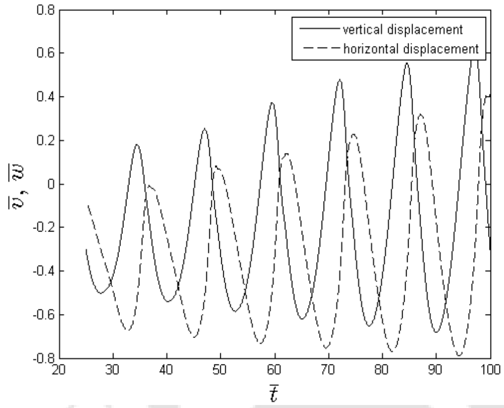

Fig. 4.7a: Response at the bearing location at $\overline{m}$ =3.0

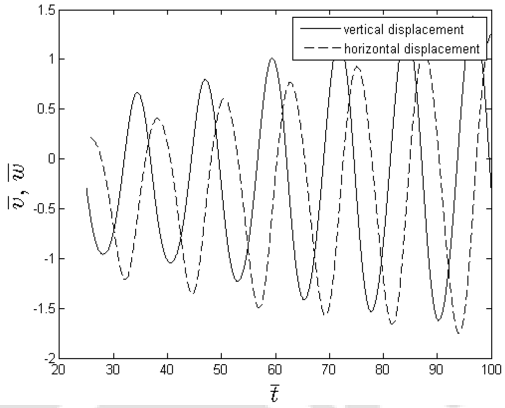

Fig. 4.7b: Response at the disk location at $\overline{m}$ =3.0

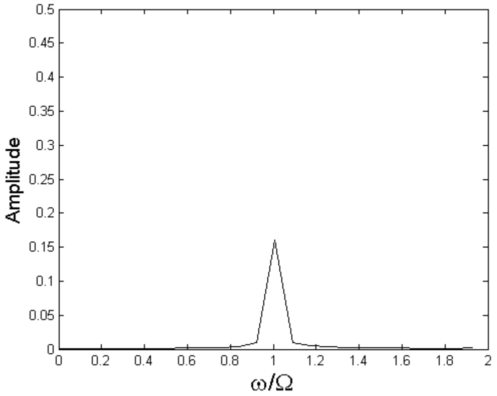

Fig. 4.8a: FFT-spectrum at the bearing location at $\overline{m}$ =1.0

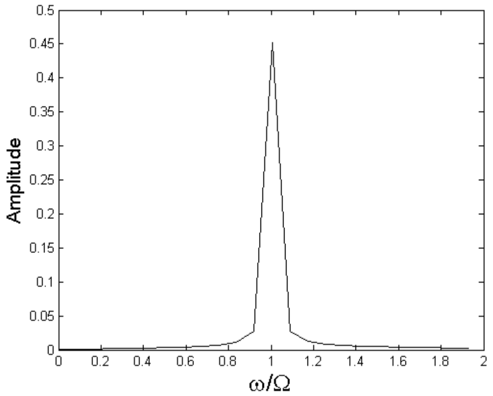

Fig. 4.8b: FFT-spectrum at the disk location at $\overline{m}$ =1.0

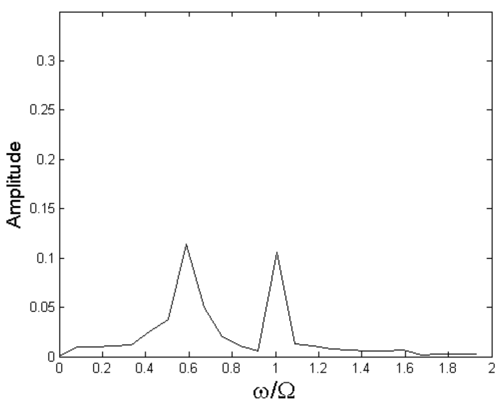

Fig. 4.9a: FFT-spectrum at the bearing location at $\bar{m}=2.0$

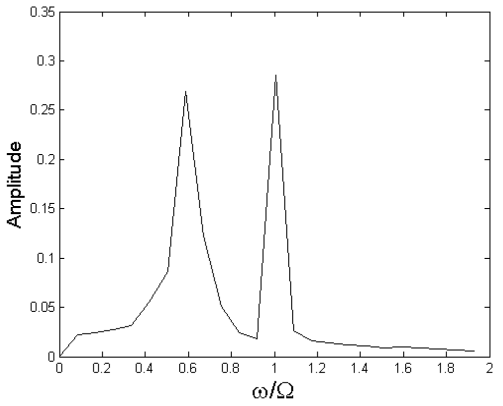

Fig. 4.9b: FFT-spectrum at the disk location at $\bar{m}=2.0$

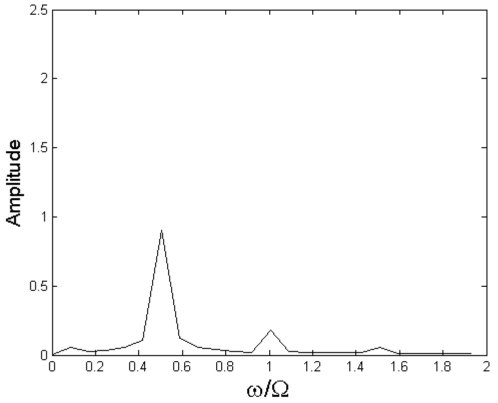

Fig. 4.10a: FFT-spectrum at the bearing location at $\bar{m}=3.0$

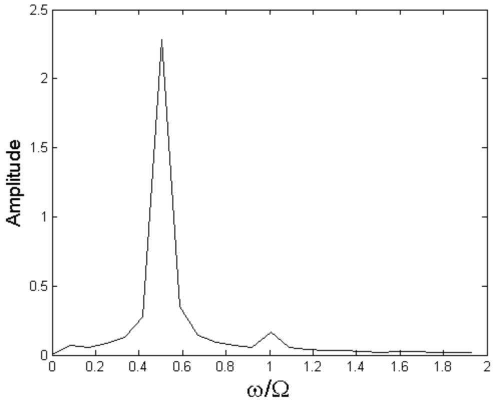

Fig. 4.10b: FFT-spectrum at the disk location at $\bar{m}=3.0$

4.3.3 Waterfall Diagrams

In the present scheme of analysis, the non-dimensional parameters obtained are, $L_B/D, e/C, e_d/C, H/R, R/C, R/(2L), E/(\rho gL), m_d/(\rho AL)$ and $C\Omega^2/g$. The last parameter is known as mass parameter, $\bar{m}$, a function of the operating speed. In the present analysis, mass parameter, $\bar{m}$ is changed over a range and simultaneously change in the dynamic behaviour of the rotor-bearing is studied. Waterfall diagrams which can depict the change in dynamics with change in spin speed are obtained for both run-up and run-down case. In the run-up procedure spin speed of the rotor bearing system increases with time whereas during run-down, speed of the rotor decreases. The following changes are made for analysis during run-up and run-down.

Run-up case: Mass parameter which is a function of spin speed is incremented in a step-wise manner and the state variables at the end of one integration cycle are taken as the initial condition for the next mass parameter.

Run-down case: Mass parameter is decremented in a step-wise manner and the state variables at the end of one integration cycle are taken as the initial condition for the next mass parameter.

Waterfall diagrams are obtained for different slenderness ratios, stiffness parameters, ratio of disk mass to shaft mass and bearing feeding parameters. The effects of different non-dimensional parameters are studied for different values of bearing feeding parameters. Since the trend of behaviour of the rotor-bearing system remains same with other values of feeding parameter, therefore, results with $\beta = 0.03$ and 1.0 only are presented here.

Figure 4.11 shows the variation of non-dimensional first natural frequency as a function of mass parameter of a rigidly supported rotor. The critical value of mass parameter corresponds to resonance speed at which the $\omega / \Omega = 1$ line intersects the plot as depicted in Fig. 4.11. Both forward and backward natural frequencies are observed.

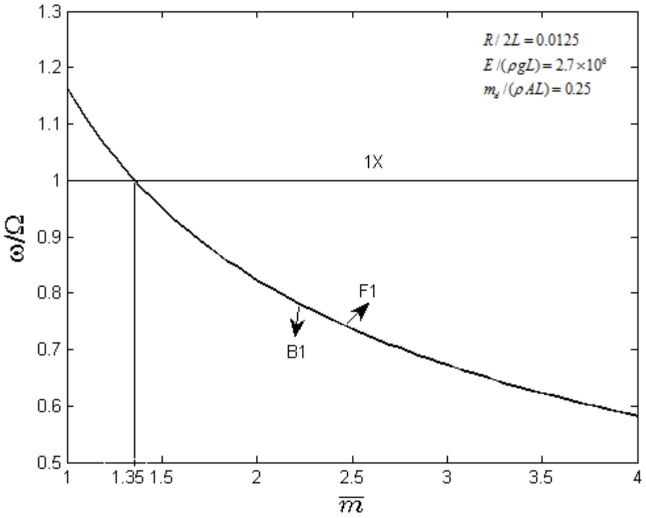

Fig. 4.11: Variation of natural whirl frequency with mass parameter

Waterfall diagrams (Figs. 4.12-4.30) of rotors with different bearing feeding parameters, bearing aspect ratios, slenderness ratio of the rotor and stiffness parameters are obtained at the bearing location and the disk location. The following parameters are kept same while drawing the waterfall diagrams: $H/R = 0.2$; $\bar{K}_x = \bar{K}_z = 1.0$.

The waterfall diagrams of the flexible rotor exhibit the following dynamic phenomena:

1. When the mass parameter of the rotor is low, there is only synchronous vibration with small amplitudes as shown in Figs. 4.12-4.30. In such a case, only one peak is observed along the line ω/Ω=1. This is caused by the unbalance of the rotor.
2. Unbalance response becomes maximum at a value of mass parameter corresponding to the resonance frequency (*e.g.*, for rotor with slenderness ratio, $R/2L = 0.0125$ and stiffness parameter, $E/(\rho gL) = 2.7\times10^6$ critical speed is $\bar{m}$=1.35 (Fig. 4.11) and from the waterfall diagram of the same rotor highest peak along the ω/Ω=1 line has been observed at close to $\bar{m}$=1.4 (Fig. 4.12a-b)). Therefore, unbalance becomes maximum at the mass parameter which corresponds to resonance frequency.
3. At higher values of mass parameter apart from synchronous vibration, oil-whirl which is half-synchronous vibration also appears as observed in Figs. 4.12-4.30; one more peak is observed along the ω/Ω=0.5 line. Amplitude of oil whirl increases with the increase of mass parameter and is much higher than that of unbalance response.
4. Waterfall diagrams during run-up and run-down of machines show distinct behaviour as observed from Figs. 4.12a through 4.17b. Waterfall diagrams in run-up and run-down are depicted in Figs. 4.12a-4.12b when $R/2L = 0.0125$, $E/(\rho gL) = 2.7\times10^6$, $\bar{m}_d$=0.25, and $\beta = 0.0$. It has been observed that during run-up (Fig. 4.12a) oil-whirl starts at $\bar{m}$=4.0, but for run-down (Fig. 4.12b) it ends at $\bar{m}$=2.2. This means that during run-down oil-whirl does not disappear just at the speed where oil-whirl first appears during the run-up process. Oil-whirl during run-down disappears at lower speed than the speed at which it appeared in run-up. This phenomenon is known as hysteresis [35-36]. This type of hysteresis has been observed for all other values of bearing feeding parameters as well as different values of slenderness ratio of the rotor.

4.3.3.1 Effect of Bearing Feeding Parameter

Bearing feeding parameter depends on the permeability of the porous housing. Its effect on the dynamics of rotor-bearing can be studied by changing its value while other parameters are kept constant as seen in Figs. 4.12a through 4.15b. Waterfall diagrams for both run-up and run-down processes are obtained for four different values of bearing feeding parameter, β=0.0, 0.03, 1.0 and 3.0 when $R/2L = 0.0125$, $E/(\rho g L) = 2.7\times10^6$ and $\bar{m}_d$ =0.25.

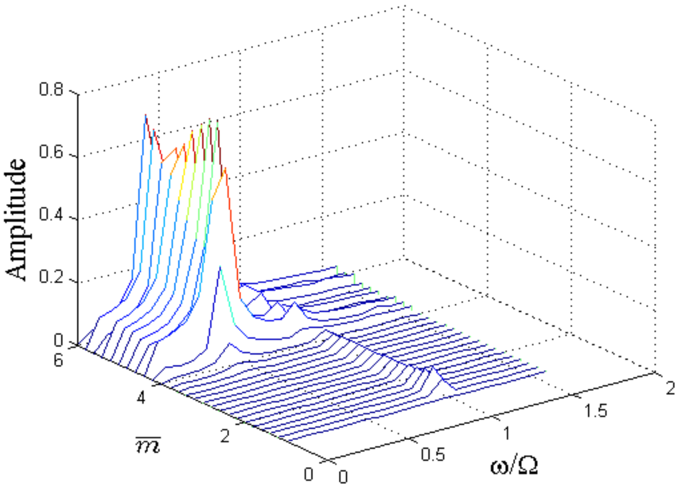

Fig. 4.12a: Waterfall diagram of rotor during run-up with, $R/2L = 0.0125$, $E/(\rho g L) = 2.7\times10^6$, $\bar{m}_d = 0.25$, e_d/C=0.25, $\beta = 0.0$

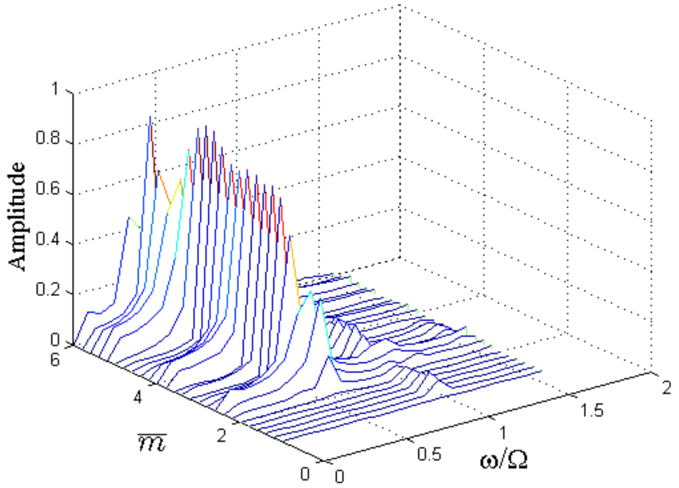

Fig. 4.12b: Waterfall diagram of rotor during run-down with, $R/2L = 0.0125$, $E/(\rho g L) = 2.7\times10^6$, $\bar{m}_d = 0.25$, e_d/C=0.25, $\beta = 0.0$

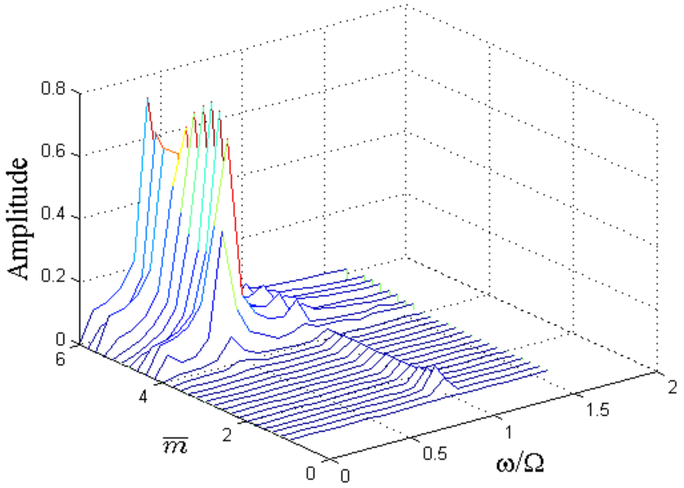

Fig. 4.13a: Waterfall diagram of rotor during run-up with, $R/2L = 0.0125$, $E/(\rho gL) = 2.7\times10^6$, $\overline{m}_d$ =0.25, e_d/C =0.25, $\beta = 0.03$

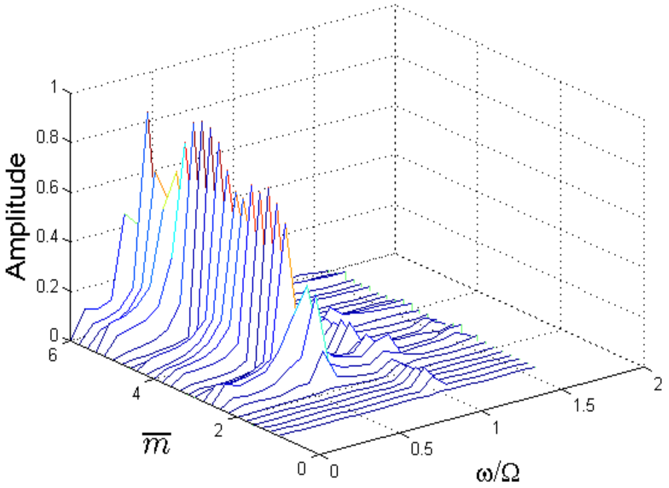

Fig. 4.13b: Waterfall diagram of rotor during run-down with, $R/2L = 0.0125$, $E/(\rho gL) = 2.7\times10^6$, $\overline{m}_d$ =0.25, e_d/C =0.25, $\beta = 0.03$

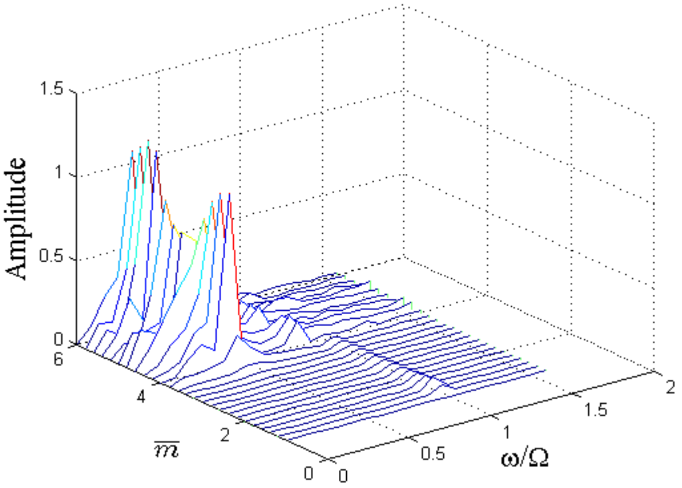

Fig. 4.14a: Waterfall diagram of rotor during run-up with, $R/2L = 0.0125$, $E/(\rho g L) = 2.7\times10^{6}$, $\overline{m}_d$ =0.25, e_d/C =0.25, $\beta = 1.0$

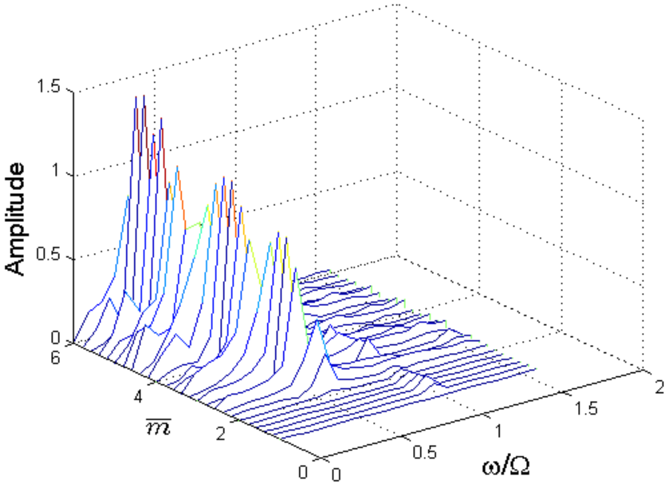

Fig. 4.14b: Waterfall diagram of rotor during run-down with, $R/2L = 0.0125$, $E/(\rho g L) = 2.7\times10^{6}$, $\overline{m}_d$ =0.25, e_d/C =0.25, $\beta = 1.0$

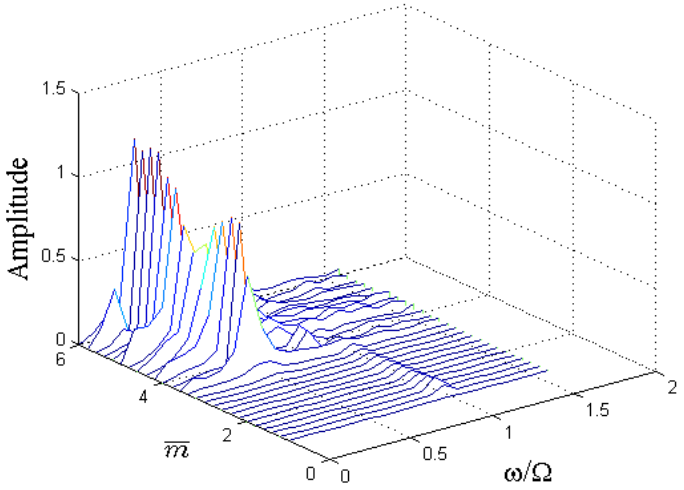

Fig. 4.15a: Waterfall diagram of rotor during run-up with, $R/2L = 0.0125$, $E/(\rho gL) = 2.7\times10^6$, $\overline{m}_d$=0.25, e_d/C=0.25, $\beta = 3.0$

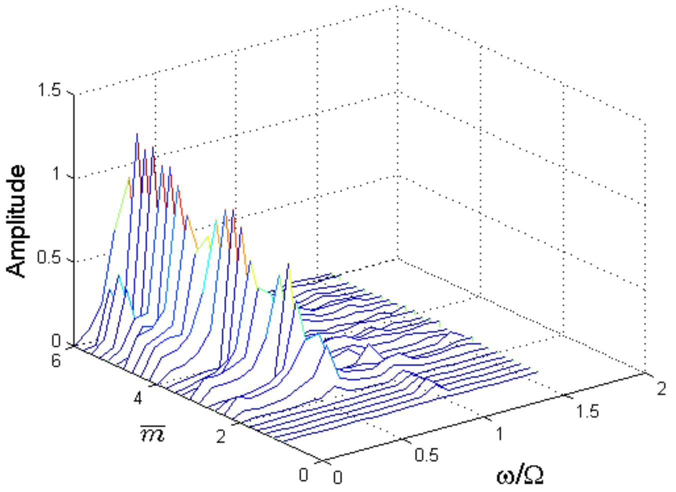

Fig. 4.15b: Waterfall diagram of rotor during run-down with, $R/2L = 0.0125$, $E/(\rho gL) = 2.7\times10^6$, $\overline{m}_d$=0.25, e_d/C=0.25, $\beta = 3.0$

It has been observed from Figs. 4.12a through 4.15b that for β=0.0 and 0.03, oil-whirl takes place at $\overline{m}$=4.0 during run-up process and oil-whirl terminates at $\overline{m}$=2.2 during run-down. However, for β=1.0 and 3.0, oil-whirl takes place at $\overline{m}$= 3.8 and 3.4 respectively during run-up process and oil-whirl terminates at $\overline{m}$=2.0 during run-down. Nevertheless, for β=1.0 and 3.0, amplitude of oil-whirl has been found to be more. Thus, it has been inferred that whirl-amplitude increases with increase in permeability of the porous bush.

Finally, a Table has been provided below summarizing the effects of different bearing feeding parameters on the appearance of oil-whirl. It may be seen from the table that at high values of β, oil-whirl appears at lower mass parameter.

Table 4.2: Effect of bearing feeding parameter on the appearance of oil-whirl

β	Mass parameter at which oil whirl appears during run-up	Mass parameter at which oil whirl terminates during run-down
0.0	4.0	2.2
0.03	4.0	2.2
1.0	3.8	2.0
3.0	3.4	2.0

4.3.3.2 Effect of Slenderness Ratio

Slenderness ratio which is defined as the ratio of radius of gyration to the length of the rotor also plays an important role in determining the dynamic characteristics of the rotor-bearing system. Waterfall diagrams for both speed-ascending and speed-descending processes are studied for three different slenderness ratios $R/2L$ = 0.0156, 0.0125 and 0.01. The respective plots are depicted in Fig. 4.13a-b, 4.16a-b and 4.17a-b when other rotor-bearing parameters are $E/(\rho g L) = 2.7\times10^6$, $\bar{m}_d$ =0.25, $\beta = 0.03$. From Figs. 4.13a, 4.16a and 4.17a it has been observed that for run-up waterfall diagrams oil-whirl takes place at $\bar{m}$ = 4.2, 4.0 and 3.0 when the slenderness ratios are $R/2L$ = 0.0156, 0.0125 and 0.01 respectively. Simultaneously, for run-down waterfall diagrams (Figs. 4.13b, 4.16b and 4.17b), oil-whirl terminates at $\bar{m}$ = 2.8, 2.2 and 1.4 respectively. Thus, it may be inferred that with the increase in slenderness ratio oil-whirl takes place at higher mass parameter vis-à-vis higher spin speed.

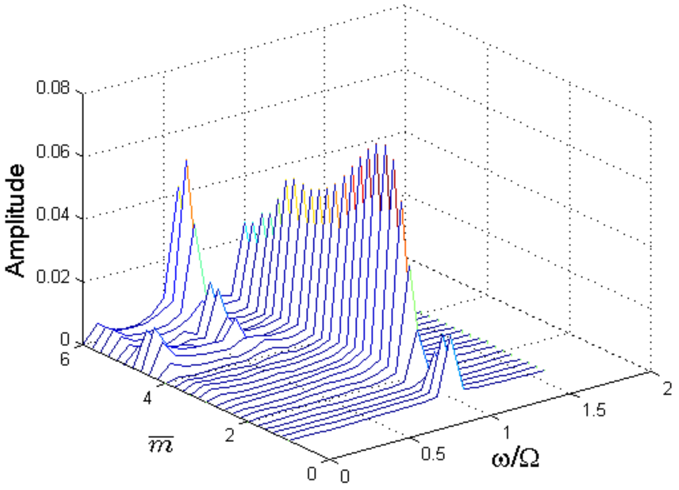

Fig. 4.16a: Waterfall diagram of rotor during run-up with, $R/2L = 0.0156$,
$E/(\rho g L) = 2.7\times10^6$, $\overline{m}_d = 0.25$, $e_d/C = 0.25, \beta = 0.03$

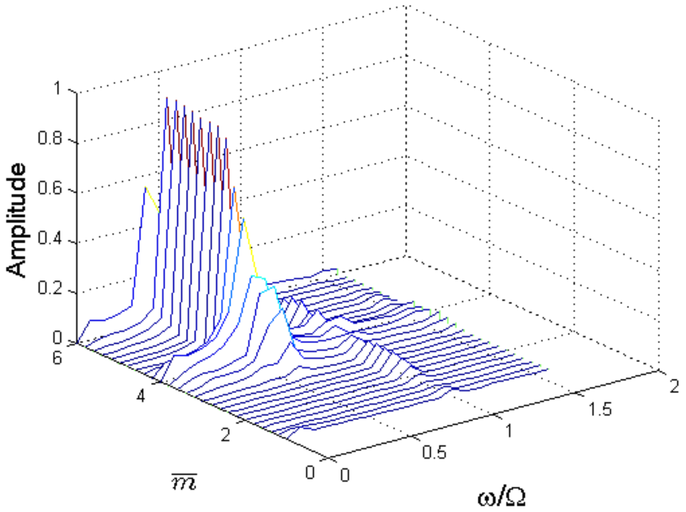

Fig. 4.16b: Waterfall diagram of rotor during run-down with, $R/2L = 0.0156$,
$E/(\rho g L) = 2.7\times10^6$, $\overline{m}_d = 0.25$, $e_d/C = 0.25, \beta = 0.03$

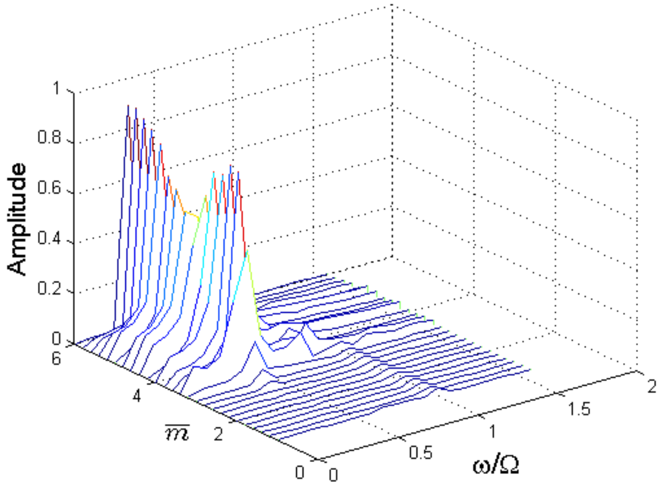

Fig. 4.17a: Waterfall diagram of rotor during run-up with, $R/2L = 0.01$, $E/(\rho g L) = 2.7\times10^6$, $\overline{m}_d = 0.25$, $e_d/C = 0.25$, $\beta = 0.03$

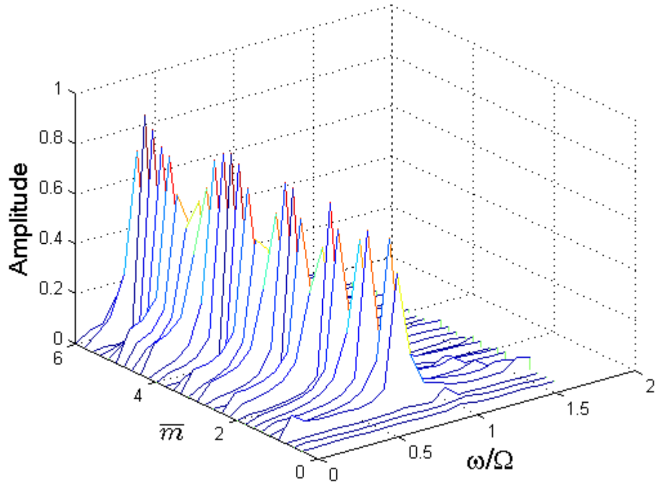

Fig. 4.17b: Waterfall diagram of rotor during run-down with, $R/2L = 0.01$, $E/(\rho g L) = 2.7\times10^6$, $\overline{m}_d = 0.25$, e_d/C =0.25, $\beta = 0.03$

The effect of slenderness ratio on dynamic behaviour of rotor-bearing system has been carried out by taking bearing feeding parameter, $\beta = 0.03$ and it may be observed that with increase in slenderness ratio oil-whirl occurs at higher spin speed. Now it is proposed to see whether the effects of slenderness ratio remain same at higher bearing feeding higher value. Therefore, waterfall diagrams during run-up are again obtained for three different slenderness ratios, *R/2L* = 0.0156, 0.0125 and 0.01

while taking a higher value of bearing feeding parameter, β = 1.0. The other rotor-bearing parameters remain same which are $E/(\rho g L) = 2.7\times10^6$, $\bar{m}_d$ =0.25, e_d/C = 0.25. The corresponding waterfall diagrams are shown in Figs. 4.18, 4.19 and 4.20 respectively. It has been observed from Figs. 4.18 through 4.20 that for *R/2L* = 0.0156, 0.0125 and 0.01 oil-whirl starts at $\bar{m}$ = 4.0, 3.8 and 2.0 respectively. Therefore, it may be concluded that with the increase in slenderness ratio oil-whirl takes place at higher mass parameter. Similar trend was also observed when the bearing feeding parameter was low, β = 0.03.

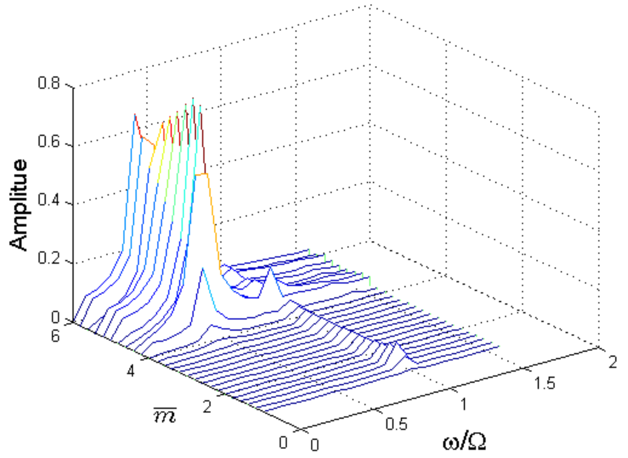

Fig. 4.18: Waterfall diagram of rotor during run-down with, $R/2L = 0.0156$, $E/(\rho g L) = 2.7\times10^6$, $\bar{m}_d = 0.25$, $e_d/C = 0.25$, $\beta = 1.0$

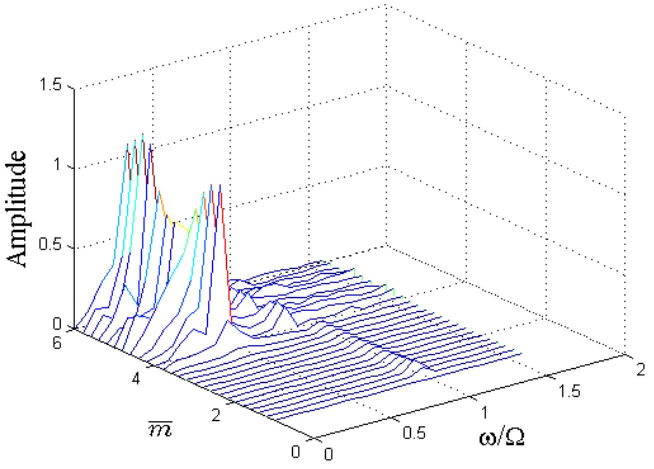

Fig. 4.19: Waterfall diagram of rotor during run-down with, $R/2L$=0.0125, $E/(\rho g L) = 2.7\times10^6$, $\bar{m}_d = 0.25$, $e_d/C = 0.25$, $\beta = 1.0$

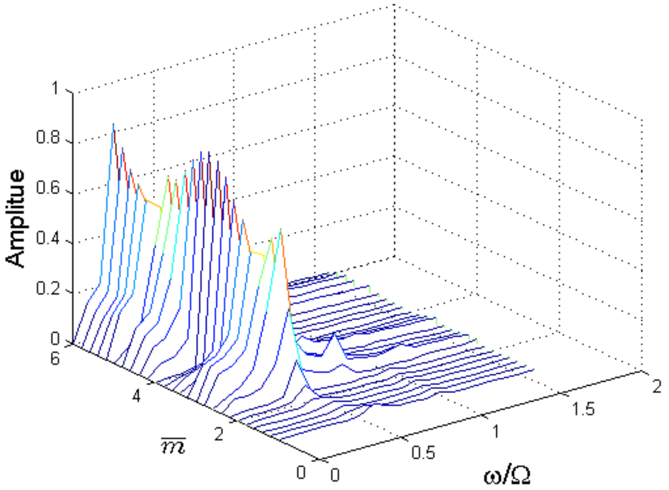

Fig. 4.20: Waterfall diagram of rotor during run-down with, $R/2L$=0.01, $E/(\rho g L)=2.7\times10^6$, $\overline{m}_d=0.25$, $e_d/C=0.25$, $\beta=1.0$

A Table has been provided below summarizing the effects of different slenderness ratio of the rotor on the appearance of oil-whirl for three different values of bearing feeding parameters. It may be observed that, for all values of β as the slenderness ratio increases, oil-whirl appears at higher mass parameter. Also, as the permeability increases, oil-whirl appears at lower mass parameter.

Table 4.3: Effect of slenderness ratio on the appearance of oil-whirl

R/2L	Mass parameter at which oil whirl appears during run-up			Mass parameter at which oil whirl terminates during run-down
	$\beta=0.03$	$\beta=1.0$	$\beta=3.0$	$\beta=0.03$
0.0156	4.2	4.0	3.6	2.8
0.0125	4.0	3.8	3.4	2.2
0.01	3.0	2.0	1.4	1.4

4.3.3.3 Effect of Stiffness parameter

Stiffness parameter, which depends on the material properties and length of the rotor, is also found to have significant effect on the waterfall diagram of rotor-bearing system. To study the effect of stiffness parameter, waterfall diagrams for run-up process are obtained for three values of stiffness parameters, $E/(\rho g L) = 2.7\times10^6$, 1.8×10^6 and 5.4×10^6 when other rotor-bearing parameters are $R/2L = 0.01$, $\overline{m}_d =$ 0.25 and $\beta = 0.03$. The waterfall diagrams are shown in Figs. 4.17a, 4.21 and 4.22 respectively. It has been observed from Fig. 4.17a that for $E/(\rho g L) = 2.7\times10^6$, oil-whirl appears at $\overline{m}$ =3.0, similarly for $E/(\rho g L) = 5.4\times10^6$ (Fig. 4.21) and 1.8×10^6 (Fig. 4.22) oil-whirl takes place at $\overline{m}$ =4.0 and 2.0 respectively. These results clearly indicate that with increase in stiffness parameter, oil-whirl appears at higher mass parameter. Therefore, higher the stiffness parameter, oil-whirl takes place at higher spin speed.

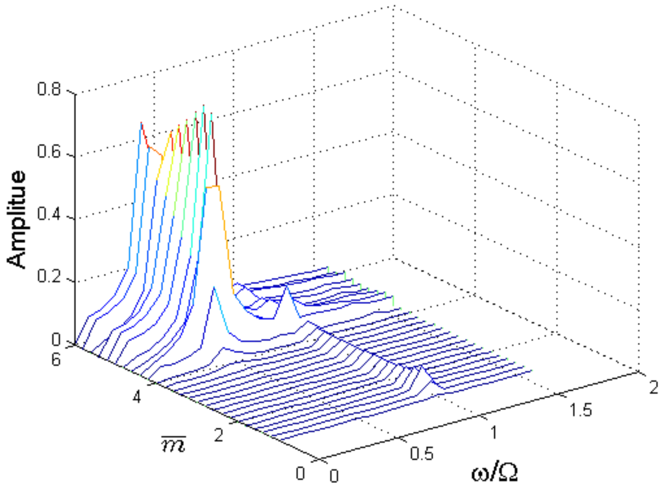

Fig. 4.21: Waterfall diagram of rotor during run-up with, $R/2L = 0.01$, $E/(\rho g L) = 5.4\times10^6$, $\overline{m}_d = 0.25$, $e_d/C = 0.25, \beta = 0.03$

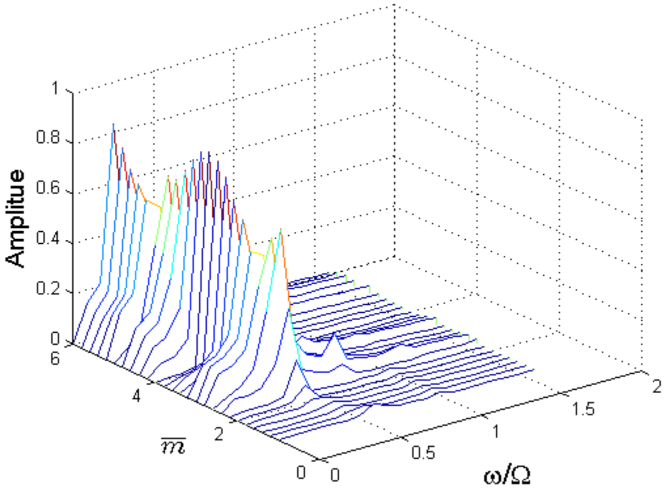

Fig. 4.22: Waterfall diagram of rotor during run-up with, $R/2L = 0.01$, $E/(\rho g L) = 1.8\times10^6$, $\overline{m}_d = 0.25$, $e_d/C = 0.25$, $\beta = 0.03$

The previous investigation of the effects of stiffness parameter was carried out at lower bearing feeding parameter, $\beta = 0.03$. Now, waterfall diagrams during speed-ascending process are again obtained by taking higher value of $\beta = 1.0$ for three different values of stiffness parameters, $E/(\rho g L) = 2.7\times10^6$, 5.4×10^6 and 1.8×10^6 when the other rotor-bearing parameters are $R/2L = 0.01$, $\overline{m}_d$ =0.25, and e_d/C = 0.25. The corresponding figures are shown in Figs. 4.20, 4.23 and 4.24 respectively. It has been observed from these figures that oil-whirl stars at $\overline{m}$ = 2.0, 2.2 and 0.9 respectively. Therefore, the conclusion that with higher stiffness parameter, oil-whirl takes place at higher spin speed remains same even at higher bearing feeding parameter.

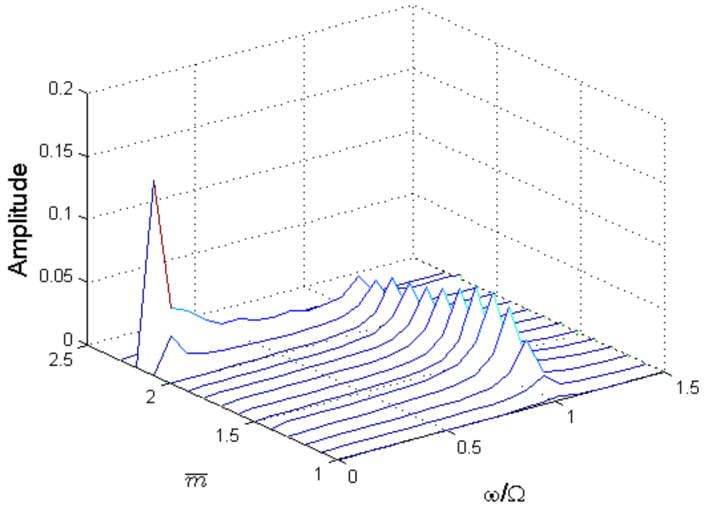

Fig. 4.23: Waterfall diagram of rotor during run-up with, $R/2L = 0.01$, $E/(\rho gL) = 5.4\times10^6$, $\overline{m}_d = 0.25$, $e_d/C = 0.25$, $\beta = 1.0$

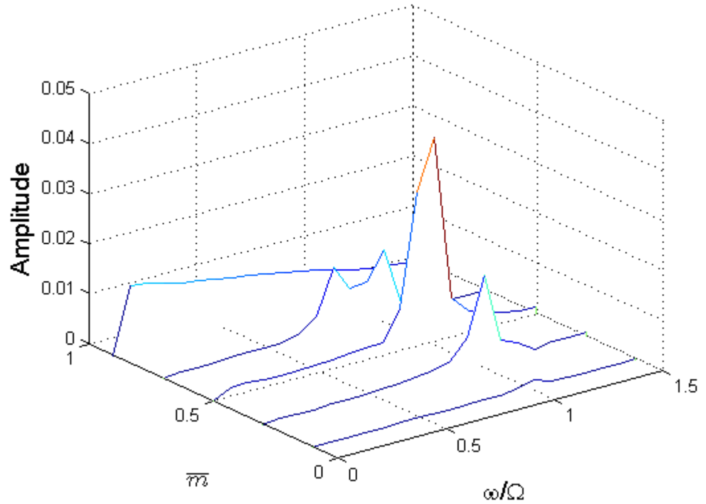

Fig. 4.24: Waterfall diagram of rotor during run-up with, $R/2L = 0.01$, $E/(\rho gL) = 1.8\times10^6$, $\overline{m}_d = 0.25$, $e_d/C = 0.25$, $\beta = 1.0$

Finally, the effect of different stiffness parameters on the appearance of oil-whirl has been is summarized in the Table 4.4. It may be seen from Table 4.4, that for all values of bearing feeding parameter, oil-whirl appears at higher mass parameter as the stiffness parameter increases. Also, with increase in bearing feeding parameter, β, oil-whirl appears at lower mass parameter.

Table 4.4: Effect of stiffness parameter on the appearance of oil-whirl

$E/(\rho g L)$	Mass parameter at which oil-whirl appears during run-up		
	$\beta = 0.03$	$\beta = 1.0$	$\beta = 3.0$
1.8×10^6	2.0	0.9	0.6
2.7×10^6	3.0	2.0	1.4
5.4×10^6	4.0	2.2	2.4

4.3.3.4 Effect of Ratio of Disk Mass to Shaft Mass

Disk masses are always present in rotor system in forms of gears, pulleys, couplings etc. Disk masses have profound effect on the dynamics of rotor-bearing system. Therefore, it is very important to study the effect of unbalance masses on the dynamic behaviour of the system. In the present analysis three different ratios of disk mass to shaft mass are considered and the corresponding waterfall diagrams for run-up process are generated. The three values of ratios of disk mass to shaft mass considered are, $\overline{m}_d$ = 0.25, 1.5 and 3.0 when other rotor-bearing parameters are $R/2L = 0.0125$, $E/(\rho g L) = 2.7\times10^6$ and $\beta = 0.03$ and the respective waterfall diagrams are depicted in Figs. 4.13a, 4.25 and 4.26. It has been seen from Figs. 4.13a, 4.25 and 4.26 that for $\overline{m}_d$ =0.25, 1.5 and 3.0 oil-whirl starts at $\overline{m}$ = 4.0, 1.8 and 1.0 respectively. These waterfall diagrams clearly indicate that oil-whirl appears at lower mass parameter as the ratio of disk mass to shaft mass increases.

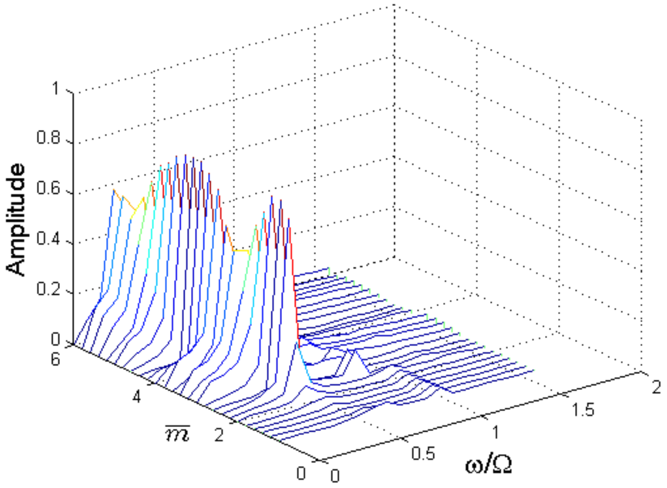

Fig. 4.25: Waterfall diagram of rotor during run-up with, $R/2L = 0.0125$, $E/(\rho g L) = 2.7\times10^6$, $\overline{m}_d = 1.5$, $e_d/C = 0.25, \beta = 0.03$

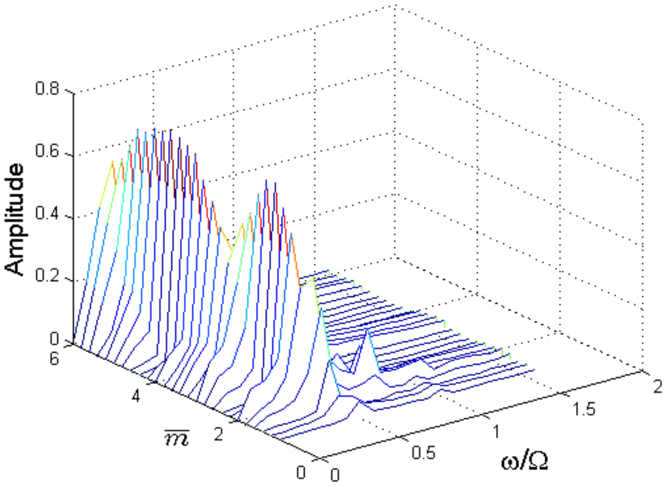

Fig. 4.26: Waterfall diagram of rotor during run-up with, $R/2L = 0.0125$, $E/(\rho g L) = 2.7\times10^6$, $\overline{m}_d = 3.0$, $e_d/C = 0.25, \beta = 0.03$

The effect of the ratio of disk mass to shaft mass on waterfall diagram is studied in above section at lower bearing feeding parameter value, $\beta = 0.03$. It is now proposed to investigate the effects of ratio of disk mass to shaft mass at higher feeding parameter. To this effect, waterfall diagrams for $\overline{m}_d$ = 0.25, 1.5 and 3.0 are obtained by taking a higher value of bearing feeding parameter, $\beta = 1.0$. The waterfall diagrams for $\overline{m}_d =$ 0.25, 1.5 and 3.0 are shown in Figs. 4.19, 4.27 and 4.28 respectively. The other non-dimensional parameters are mentioned with the corresponding figures.

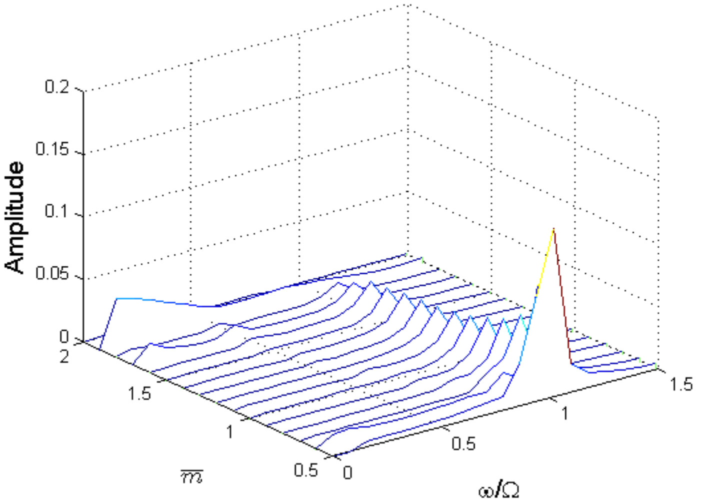

Fig. 4.27: Waterfall diagram of rotor during run-up with, $R/2L = 0.0125$, $E/(\rho g L) = 2.7 \times 10^6$, $\overline{m}_d = 1.5$, $e_d/C = 0.25$, $\beta = 1.0$

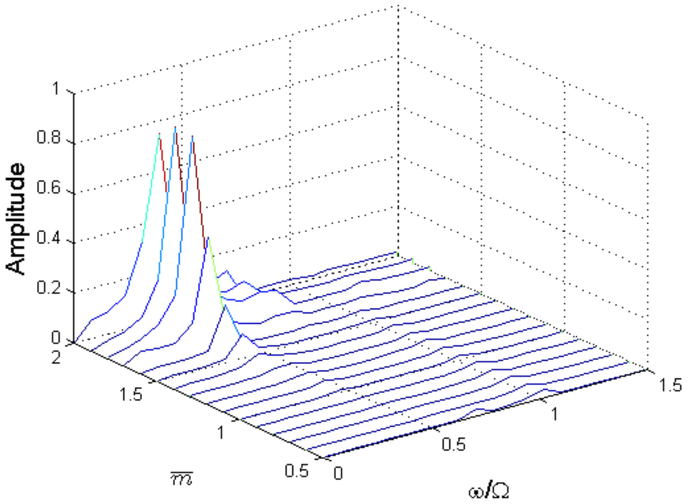

Fig. 4.28: Waterfall diagram of rotor during run-up with, $R/2L = 0.0125$, $E/(\rho g L) = 2.7 \times 10^6$, $\overline{m}_d = 3.0$, $e_d/C = 0.25$, $\beta = 1.0$

It has been observed that for $\overline{m}_d = 0.25$, 1.5 and 3.0 oil-whirl starts at $\overline{m}$ = 3.8, 1.7 and 1.3 respectively. Thus, it may be concluded that as $\overline{m}_d$ increases oil-whirl appears at lower mass parameter. The same trend was observed at lower value of bearing feeding parameter.

The effect of the ratio of disk mass to shaft mass on the appearance of oil-whirl has been is tabulated in Table 4.5. It has been observed from Table 4.5 that as $\overline{m}_d$ increases oil-whirl appears at lower mass parameter. Also, it may be again observed that oil-whirl starts appearing at lower mass parameter as the permeability of porous bush given in terms of β increases.

Table 4.5: Effect of ratio of disk mass to shaft mass on appearance of oil-whirl

$\overline{m}_d$	Mass parameter at which oil whirl appears during run-up		
	$\beta = 0.03$	$\beta = 1.0$	$\beta = 3.0$
0.25	4.0	3.8	3.4
1.5	1.8	1.7	1.3
3.0	1.0	1.3	0.6

4.3.3.5 Effect of Eccentricity of Disk Mass

Eccentricity of the disk mass is given by the distance between the geometric centre and the mass centre. This quantity also significantly affects the non-linear dynamics of the rotor-bearing system. Waterfall diagrams are obtained for three different eccentricities of the disk mass: $e_d/C = 0.05$, 0.25 and 0.5 as shown in Figs. 4.29, 4.25 and 4.30 respectively. The other rotor-bearing parameters are $R/2L = 0.0125$, $E/(\rho g L) = 2.7\times10^6$, $\overline{m}_d$ =1.5 and $\beta = 0.03$. It has been observed from the waterfall diagrams for all values of e_d/C, oil-whirl appears at $\overline{m}$ = 1.8. However, for e_d/C=0.05 (Fig. 4.22) the vibration amplitude due to unbalance is very small compared to other values of e_d/C.

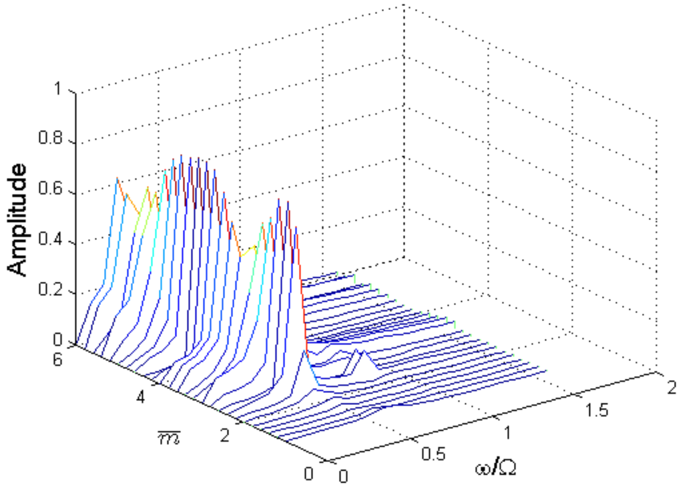

Fig. 4.29: Waterfall diagram of rotor during run-up with, $R/2L = 0.0125$, $E/(\rho gL) = 2.7\times10^6$, $\overline{m}_d = 1.5$, $e_d/C = 0.05, \beta = 0.03$

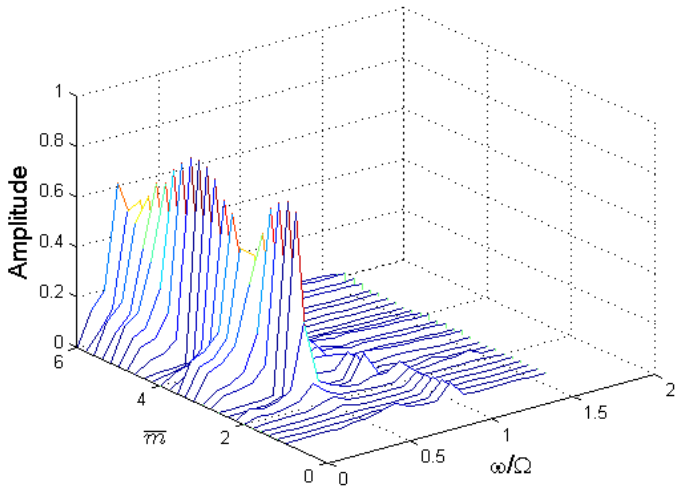

Fig. 4.30: Waterfall diagram of rotor during run-up with, $R/2L = 0.0125$, $E/(\rho gL) = 2.7\times10^6$, $\overline{m}_d = 1.5$, $e_d/C = 0.5, \beta = 0.03$

Finally, Table 4.6 summarizes the effect of eccentricity of disk mass on appearance of oil-whirl for $\beta = 0.03$. From the table it may be observed that oil-whirl appears at same value of mass parameter, $\overline{m}$ = 1.8 for all the eccentricity ratio of the disk considered.

Table 4.6: Effect of eccentricity of disk mass on appearance of oil-whirl

e_d/C	Mass parameter at which oil whirl appears during run-up
	$\beta = 0.03$
0.05	1.8
0.25	1.8
0.5	1.8

4.3.4 Bifurcation Diagrams

Hydrodynamic journal is a common machine element which is strongly non-linear as the bearing forces are non-linear functions of displacement and velocity of the journal centre. Rotor supported by hydrodynamic bearings under unbalance excitation may exhibit periodic or aperiodic response depending upon its spin speed. As the motion of a rotor-bearing system becomes aperiodic the system shows high amplitude of vibration. The Hopf Bifurcation Theory is concerned with the bifurcation of the periodic orbits. Therefore, it is pertinent to study the bifurcation behaviour of a flexible rotor supported on oil bearings. The study incorporates porous bearings, because of its poor stability characteristics compared to plain journal bearings. The effects of various non-dimensional parameters including the bearing feeding parameter on the bifurcation characteristics of a rotor-bearing system are analyzed.

To generate a bifurcation diagram mass parameter is varied with a constant step and the state variables at the end of integration are used as initial value for the next mass parameter. This means that there is tendency for the integration cycle to follow a single response curve. The variation of the $\bar{v}\left(n\bar{T}\right)$ and $\bar{w}\left(n\bar{T}\right)$ coordinates, of return in the Poincaré map (*n* is the number of discrete points in the Poincaré map) is then plotted against mass parameter to generate bifurcation diagram [72]. Bifurcation diagrams are generated for different slenderness ratio, stiffness parameter of the rotor and ratio of disk mass to shaft mass as well as for different bearing feeding parameter of the bearing. In the analysis the mass parameter $\bar{m}$ is incremented with a step of 0.2. The value of corresponding Sommerfeld number for

$\overline{m} = 1.0$ is *S*=0.1792. The following parameters are used in this analysis: $H/R = 0.2$; $\overline{K}_x = \overline{K}_z = 1.0$; $e_d/C = 0.25$.

4.3.4.1 Effect of Slenderness Ratio

Slenderness ratio is an important parameter in the bifurcation analysis of a flexible rotor. Bifurcation diagrams of horizontal and vertical displacement at the bearing location for four different slenderness ratios, *R/2L* = 0.0156, 0.0125, 0.01 and 0.00625 are shown in Figs. 4.31-4.34 respectively when the stiffness parameter is $E/(\rho g L) = 2.7 \times 10^6$, ratio of disk mass to shaft mass is $\overline{m}_d = 0.25$ and bearing feeding parameter is $\beta = 0.03$. It has been observed from Fig. 4.27 that when $1.0 < \overline{m} < 4.4$, the rotor vibration is synchronous with non-dimensional time period $\overline{T} = 2\pi$, and for $\overline{m} \geq 4.4$ the vibration becomes quasi-periodic when the slenderness ratio is 0.0156. Such type of phenomenon is known as Hopf bifurcation [35-37]. Therefore, the rotor undergoes Hopf bifurcation at $\overline{m} = 4.4$. Similarly for *R/2L*= 0.0125 (Fig. 4.32), the rotor vibration is synchronous when $1.0 < \overline{m} < 4.0$ and then beyond $\overline{m} = 4.0$ the vibration become quasi-periodic.

For rotors with slenderness ratios *R/2L*= 0.01 and 0.00625 the vibration becomes quasi-periodic at $\overline{m}$=3.0 and 1.0 respectively (Figs. 4.33-4.34). Rotors with lower slenderness ratio undergo Hopf bifurcation at lower spin speed is evident from above analysis.

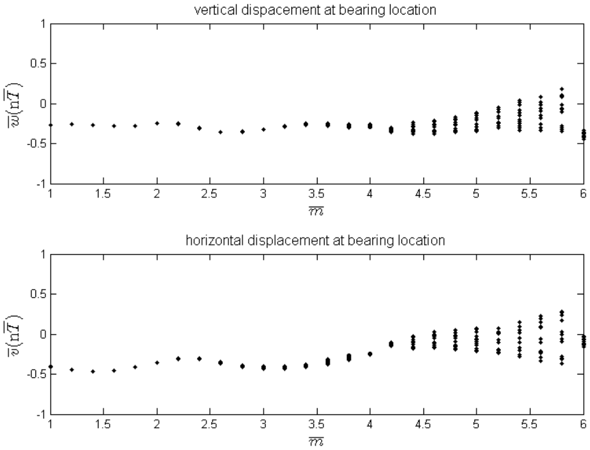

Fig. 4.31: Bifurcation diagram of rotor with $R/2L = 0.0156$,
$E/(\rho g L) = 2.7 \times 10^6$, $L_B/D = 1.0$, $\overline{m}_d = 0.25$, $\beta = 0.03$

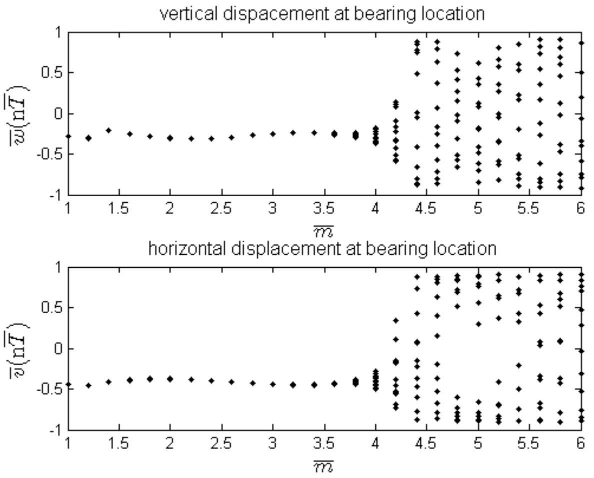

Fig. 4.32: Bifurcation diagram of rotor with $R/2L = 0.0125$,

$E/(\rho gL) = 2.7 \times 10^6$, $L_B/D = 1.0$, $\overline{m}_d = 0.25$, $\beta = 0.03$

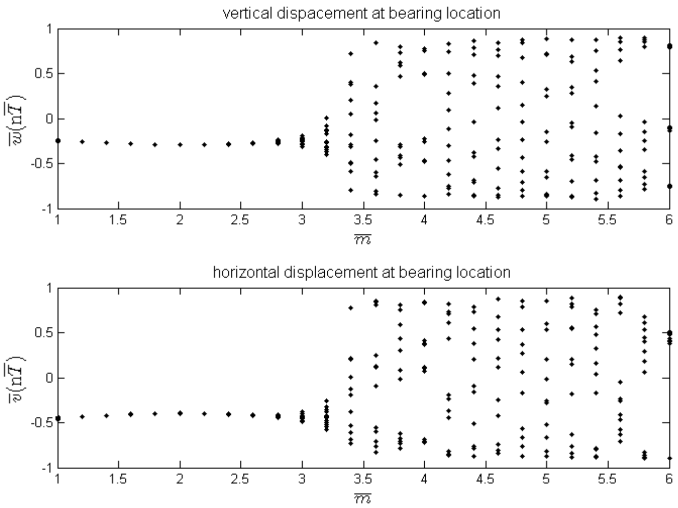

Fig. 4.33: Bifurcation diagram of rotor with $R/2L = 0.01$,

$E/(\rho gL) = 2.7 \times 10^6$, $L_B/D = 1.0$, $\overline{m}_d = 0.25$, $\beta = 0.03$

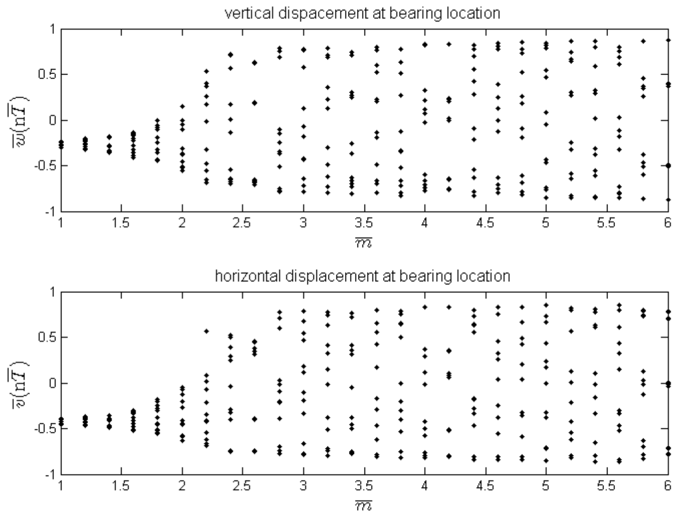

Fig. 4.34: Bifurcation diagram of rotor with $R/2L = 0.00625$,
$E/(\rho g L) = 2.7\times10^{6}$, $L_B/D = 1.0$, $\overline{m}_d = 0.25$, $\beta = 0.03$

Trajectory, time response Poincaré map and FFT-spectrum of rotor with $R/2L = 0.0125$, $E/(\rho g L) = 2.7\times10^{6}$, $\overline{m}_d =$ 0.25 and $\beta = 0.03$ are shown in Figs. 4.35-4.38. It has been observed from Figs. 4.35-4.36 that trajectory and time response of this rotor is regular at $\overline{m}$ =2.0 and 3.0, asynchronous at $\overline{m}$ =4.0 and again regular at $\overline{m}$ =5.0. It has been observed from Fig. 4.37 that vibration is single-periodic at $\overline{m}$ = 2.0 and 3.0, and then quasi-periodic at $\overline{m}$ =4.0 and 5.0. It has been also observed from Fig. 4.38 that at $\overline{m}$ =2.0 and 3.0 the motion is synchronous as the unbalance forces are the major cause of vibration. However, at $\overline{m}$ = 4.0 and 5.0, oil-film forces replaces unbalance forces as the main cause of vibration.

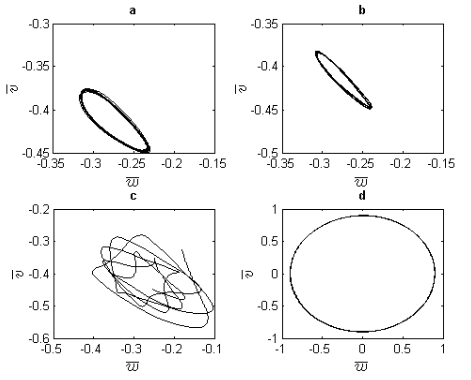

Fig. 4.35: Trajectory at (a) $\overline{m}$ =2.0, (b) $\overline{m}$ =3.0, (c) $\overline{m}$ =4.0, (d) $\overline{m}$ =5.0

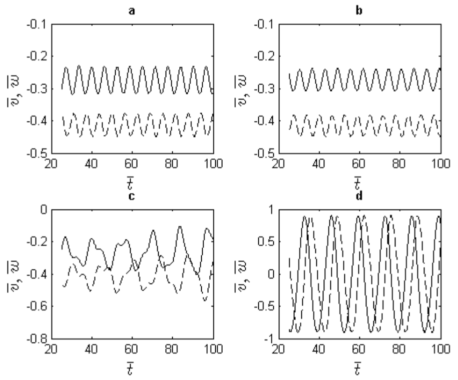

Fig. 4.36: Time response (a) $\overline{m}$ =2.0, (b) $\overline{m}$ =3.0, (c) $\overline{m}$ =4.0, (d) $\overline{m}$ =5.0

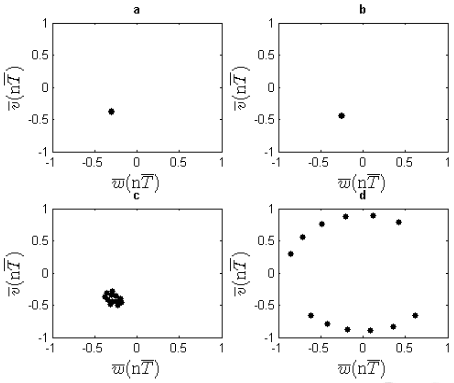

Fig. 4.37: Poincaré map at (a) $\overline{m}$ =2.0, (b) $\overline{m}$ =3.0, (c) $\overline{m}$ =4.0, (d) $\overline{m}$ =5.0

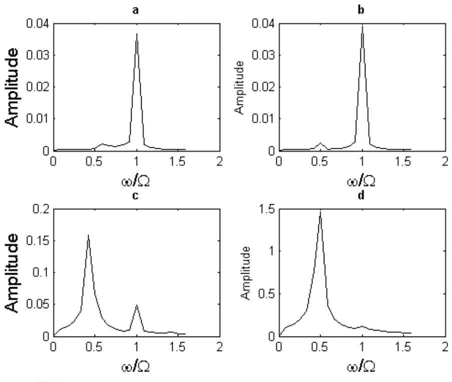

Fig. 4.38: FFT-spectrum at (a) $\overline{m}$ =2.0, (b) $\overline{m}$ =3.0,(c) $\overline{m}$ =4.0, (d) $\overline{m}$ =5.0

The effect of slenderness ratio on bifurcation characteristics is carried out in above section at low value of bearing feeding parameter, $\beta = 0.03$ and it was inferred that with increase in slenderness ratio bifurcation takes place at higher mass parameter. It is now proposed to investigate whether same effects of slenderness ratio stay at higher permeability of the porous bush. Thus, the effect of slenderness ratio has been again analyzed by taking higher value of permeability of the porous bush, *i.e.* $\beta = 1.0$. The bifurcation diagrams for *R/2L* = 0.0156, 0.0125 and 0.01 are shown in Figs. 4.39-4.41 respectively. Other rotor-bearing parameters are shown with the corresponding figures.

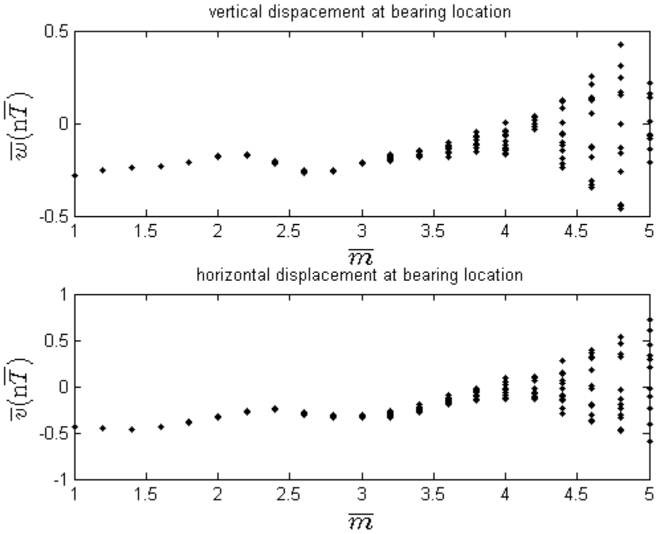

Fig. 4.39: Bifurcation diagram of rotor with $R/2L = 0.0156$,

$E/(\rho g L) = 2.7\times10^{6}$, $L_B / D = 1.0$, $\overline{m}_d = 0.25$, $\beta = 1.0$

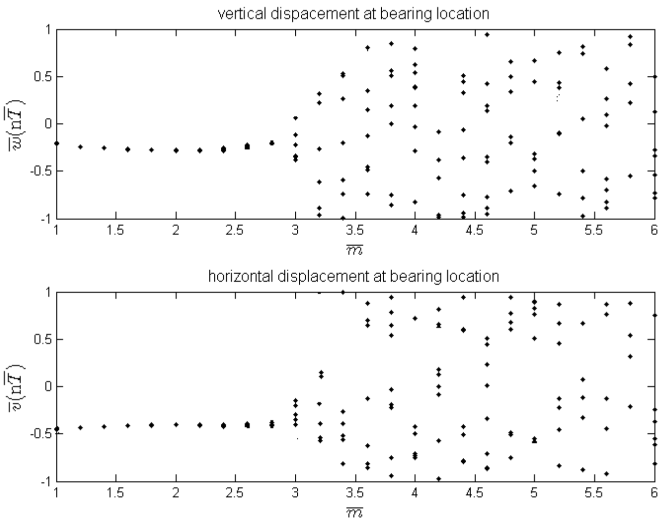

Fig. 4.40: Bifurcation diagram of rotor with $R/2L = 0.0125$,
$E/(\rho g L) = 2.7 \times 10^6$, $L_B/D = 1.0$, $\bar{m}_d = 0.25$, $\beta = 1.0$

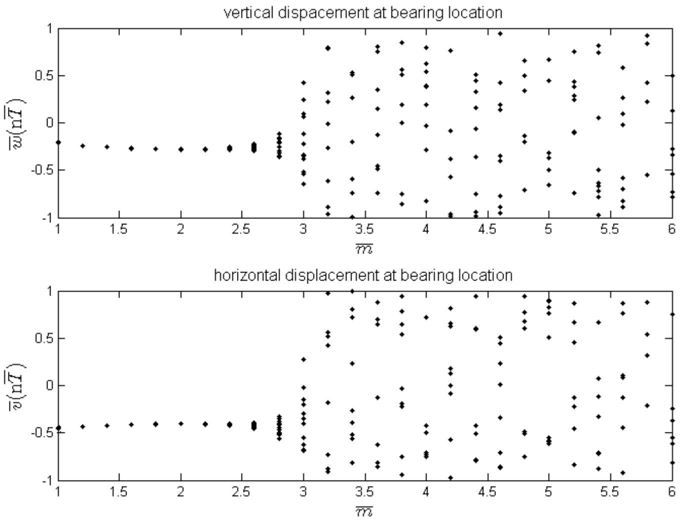

Fig. 4.41: Bifurcation diagram of rotor with $R/2L = 0.01$,
$E/(\rho g L) = 2.7 \times 10^6$, $L_B/D = 1.0$, $\bar{m}_d = 0.25$, $\beta = 1.0$

It has been observed that the rotor undergoes Hopf bifurcation at $\bar{m}$ = 3.4, 3.0 and 2.6 for *R/2L* = 0.0156, 0.0125 and 0.01 respectively. Similar to the inference drawn for $\beta = 0.03$ it has been again observed that as the slenderness ratio increases, Hopf bifurcation takes place at higher mass parameter.

The effect of different slenderness ratios on the bifurcation characteristics of rotor has been summarized in the Table 4.7. It may be again inferred that for all three values of β, as the slenderness ratio increases, the rotor undergoes bifurcation at higher mass parameter. It may be also seen that as β increases, bifurcation takes place at lower mass parameter.

Table 4.7: Effect of slenderness ratio on bifurcation

R/2L	Mass parameter at which bifurcation takes place		
	$\beta = 0.03$	$\beta = 1.0$	$\beta = 3.0$
0.0156	4.4	3.4	3.0
0.0125	4.0	3.0	2.6
0.01	3.0	2.6	2.4
0.00625	1.0	0.8	0.6

4.3.4.2 Effect of Stiffness Parameter

It has been mentioned earlier that, a new parameter, namely stiffness parameter is introduced in this study, which is defined as $E/(\rho g L)$. The parameter depends upon the material properties and the length of the rotor. An attempt has been made to study the effect of this parameter in this section. Bifurcation diagrams for three different stiffness parameters $E/(\rho g L) = 2.7\times10^6$, 1.8×10^6 and 5.4×10^6 are shown in Figs. 4.33, 4.42 and 4.43 respectively when *R/2L* = 0.01, $\bar{m}_d$ = 0.25 and $\beta = 0.03$. It has been observed from Fig. 4.33 that when $1.0 < \bar{m} < 3.0$, the rotor vibration is synchronous with non-dimensional time period $\bar{T} = 2\pi$, and for $\bar{m} \geq 3.0$ the vibration becomes quasi-periodic when the stiffness parameter is 2.7×10^6. Thus, the rotor-bearing system undergoes Hopf bifurcation at $\bar{m}$=3.0. Similarly, in the second (Fig. 4.42) and third case (Fig. 4.43), the corresponding values of $\bar{m}$ are 2.0 and 4.0. From bifurcation diagrams generated for other values of stiffness parameters, $E/(\rho g L)$, along with Figs. 4.33, 4.42 and 4.43 it has been observed that with increase in the stiffness parameter, $E/(\rho g L)$, bifurcation takes place at higher mass parameter value.

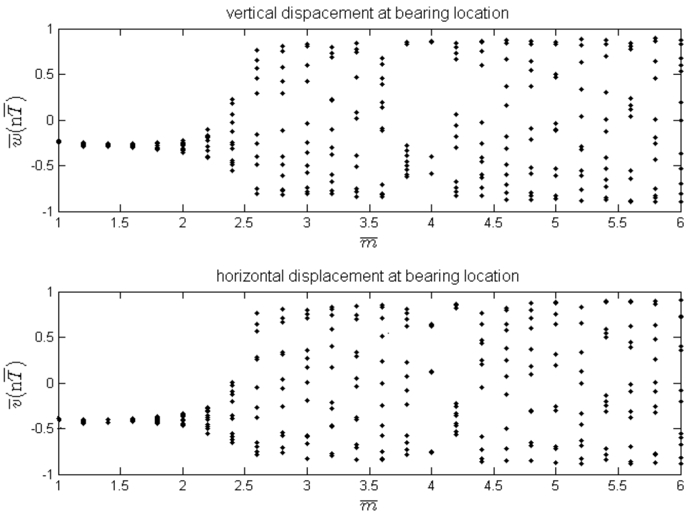

Fig. 4.42: Bifurcation diagram of rotor with $R/2L = 0.01$,
$E/(\rho g L) = 1.8\times10^6$, $L_B/D = 1.0$, $\bar{m}_d = 0.25$, $\beta = 0.03$

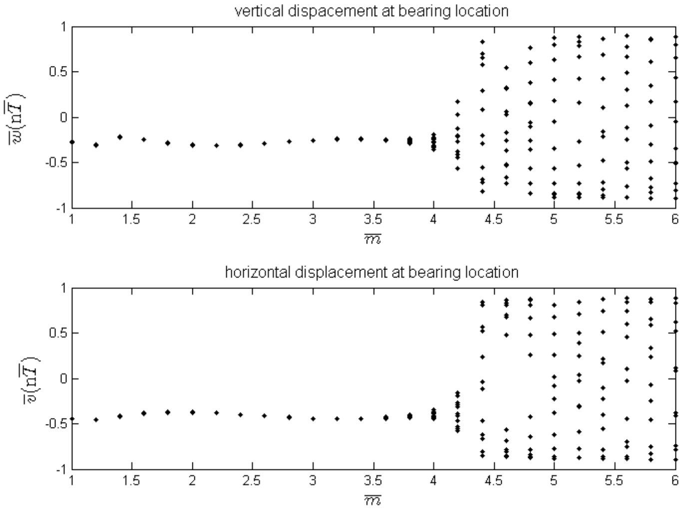

Fig. 4.43: Bifurcation diagram of rotor with $R/2L = 0.01$,
$E/(\rho g L) = 5.4\times10^6$, $L_B/D = 1.0$, $\bar{m}_d = 0.25$, $\beta = 0.03$

Trajectory, time response, Poincaré map and FFT-spectrum of rotor with $R/2L = 0.01$, $E/(\rho g L) = 5.4\times10^6$, $\bar{m}_d = 0.25$ and $\beta = 0.03$ are depicted in Figs. 4.44-4.47 respectively. It has been observed from Figs. 4.44-4.45 that trajectory and time response of this rotor are synchronous at $\bar{m} = 2.0$ and 3.0 but asynchronous at $\bar{m} = 4.0$ and then again become regular at $\bar{m} = 5.0$. It is evident from Fig. 4.46 that vibration is single-periodic at $\overline{m} = 2.0$ and 3.0 and then quasi-periodic at $\overline{m} = 4.0$ and 5.0. At $\overline{m} =$ 2.0 and 3.0, the major driving force is the unbalance, thus the motion is synchronous and both response and the trajectory are found to be regular. But at $\overline{m} =$ 4.0 both unbalance and the hydrodynamic force are dominant making the trajectory and response asynchronous. And at mass parameter $\overline{m}$ =5.0 the bearing forces are more dominant than the unbalance and the motion now again becomes regular. This can be ascertained from Fig. 4.47.

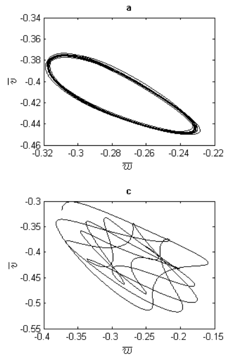

Fig. 4.44: Trajectory at (a) $\overline{m}$ =2.0, (b) $\overline{m}$ =3.0, (c) $\overline{m}$ =4.0, (d) $\overline{m}$ =5.0

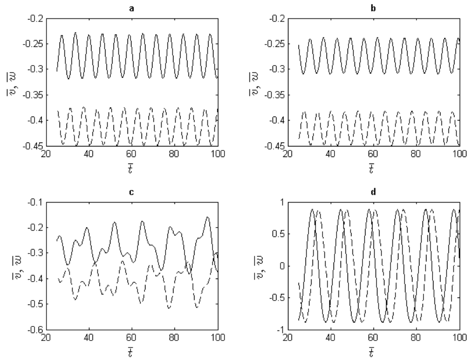

Fig. 4.45: Time response (a) $\overline{m}$ =2.0, (b) $\overline{m}$ =3.0, (c) $\overline{m}$ =4.0, (d) $\overline{m}$ =5.0

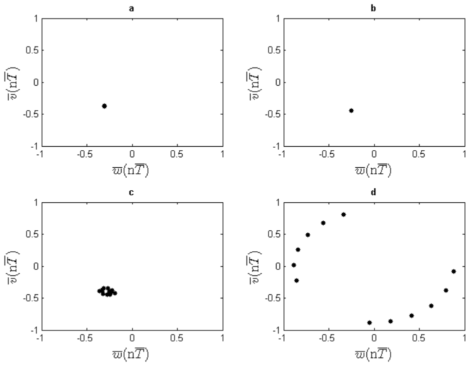

Fig. 4.46: Poincaré map at (a) $\overline{m}$ =2.0, (b) $\overline{m}$ =3.0, (c) $\overline{m}$ =4.0, (d) $\overline{m}$ =5.0

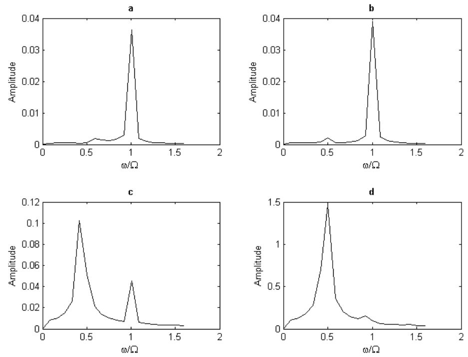

Fig. 4.47: FFT-spectrum at (a) $\overline{m}$ =2.0, (b) $\overline{m}$ =3.0,(c) $\overline{m}$ =4.0, (d) $\overline{m}$ =5.0

Bifurcation diagrams are again generated for three different stiffness parameters with higher permeability of the porous bush, $\beta = 1.0$. Bifurcation characteristics of rotors with $E/(\rho g L) = 2.7\times10^6$, 5.4×10^6 and 1.8×10^6 are shown in Figs. 4.41. 4.48 and 4.49 respectively. The other rotor-bearing parameters are mentioned with the corresponding figures. It has been observed from the results that the rotor undergoes Hopf bifurcation at $\overline{m}$ = 2.6, 3.2 and 0.9 for $E/(\rho g L) = 2.7\times10^6$, 5.4×10^6 and

1.8×10^6 respectively. Therefore, it may be concluded that even at higher bearing feeding parameter value, the trend that with increase in stiffness parameter, bifurcation takes place at higher mass parameter value remains same.

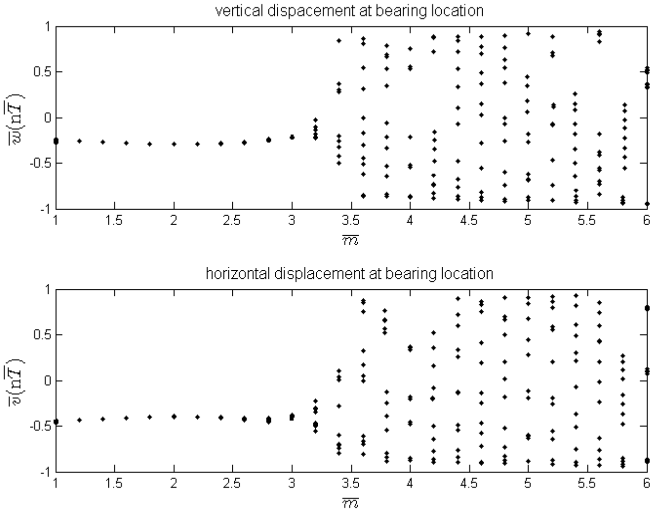

Fig. 4.48: Bifurcation diagram of rotor with $R/2L = 0.01$, $E/(\rho gL) = 5.4\times10^6$, $L_B/D = 1.0$, $\overline{m}_d = 0.25$, $\beta = 1.0$

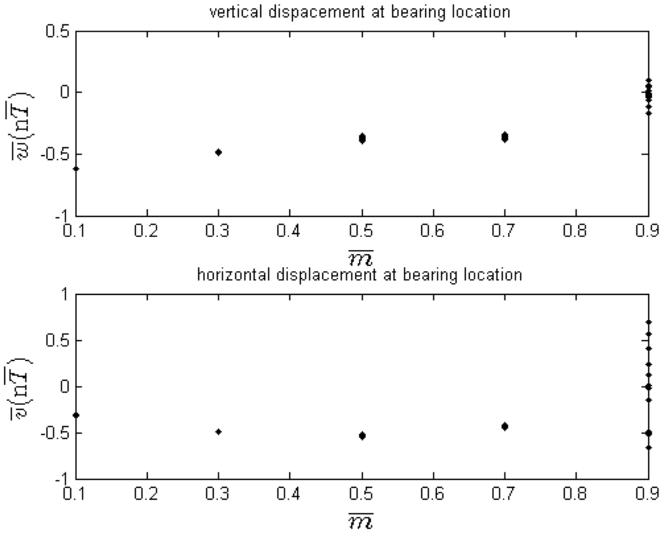

Fig. 4.49: Bifurcation diagram of rotor with $R/2L = 0.01$, $E/(\rho gL) = 1.8\times10^6$, $L_B/D = 1.0$, $\overline{m}_d = 0.25$, $\beta = 1.0$

Table 4.8 summarizes the effect of stiffness parameter on bifurcation characteristics of rotor-bearing system. It may be seen from Table 4.8, bifurcation occurs at higher mass parameter as the stiffness parameter increases for all values of bearing feeding parameter. Also, like previous cases, with increase in bearing feeding parameter, bifurcation takes place at lower mass parameter.

Table 4.8: Effect of stiffness parameter on bifurcation

$E/(\rho g L)$	Mass parameter at which bifurcation takes place		
	$\beta = 0.03$	$\beta = 1.0$	$\beta = 3.0$
1.8×10^6	2.0	0.9	0.5
2.7×10^6	3.0	2.6	2.4
5.4×10^6	4.0	3.2	2.8

4.3.4.3 Effect of Bearing Feeding Parameter

Bearing feeding parameter which depends on the permeability of the porous bush also has significant effect on the bifurcation behaviour of the rotor-bearing system. Figures 4.50-4.53 depict the bifurcation diagrams at the bearing location for four different values of bearing feeding parameters, β= 0.003, 0.1, 1.0 and 3.0 respectively when $R/(2L) = 0.01$, $E/(\rho g L) = 2.7\times10^6$ and $\bar{m}_d$ = 0.25. It has been observed from these plots that for β= 0.003 and 0.1 in the region $1.0 < \bar{m} < 3.0$, the rotor vibration is synchronous with non-dimensional time period $\bar{T} = 2\pi$ and then bifurcates at the same value of $\bar{m}$ = 3.0. But for β= 1.0 and 3.0 the values of mass parameter at which bifurcation occurs are $\bar{m}$ = 2.6 and 2.4 respectively. Therefore, it may be concluded that in the lower range of the bearing feeding parameter permeability has no significant effect on the bifurcation characteristics of the rotor-bearing system but at higher values of β bifurcation takes place at lower mass parameter as permeability increases.

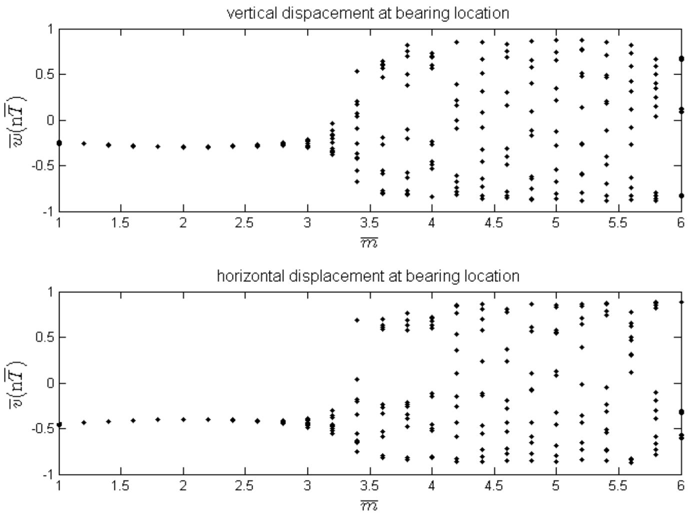

Fig. 4.50: Bifurcation diagram of rotor with $R/2L = 0.01$, $E/(\rho g L) = 2.7\times10^{6}$, $L_B/D = 1.0$, $\overline{m}_d$ =0.25, $\beta = 0.003$

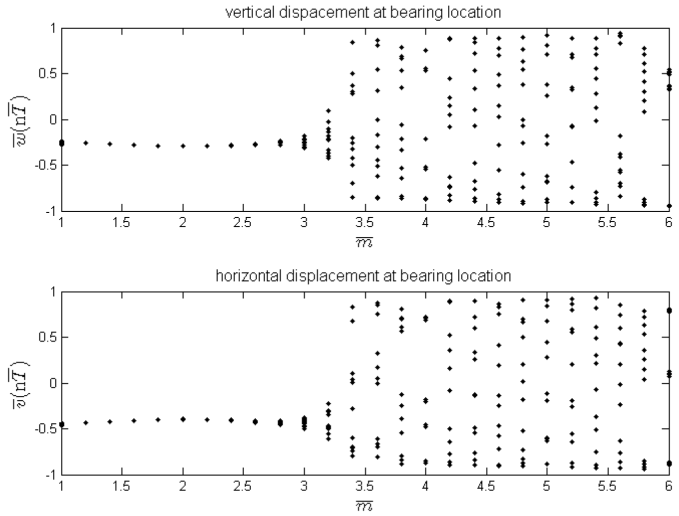

Fig. 4.51: Bifurcation diagram of rotor with $R/2L = 0.01$, $E/(\rho g L) = 2.7\times10^{6}$, $L_B/D = 1.0$, $\overline{m}_d$ =0.25, $\beta = 0.1$

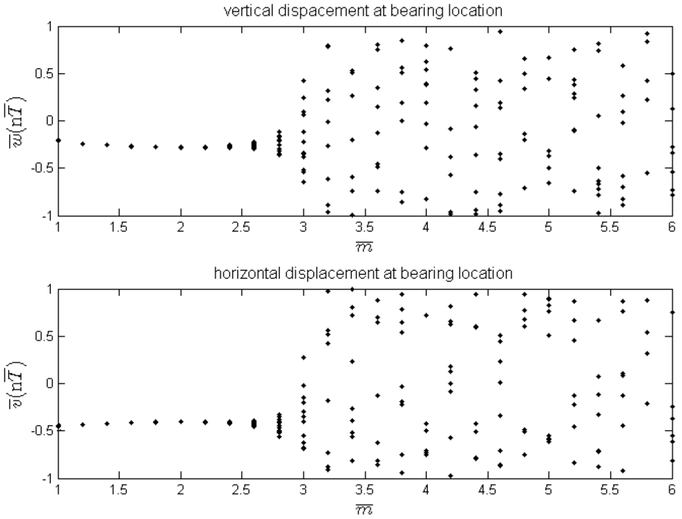

Fig. 4.52: Bifurcation diagram of rotor with $R/2L = 0.01$, $E/(\rho gL) = 2.7\times10^6$, $L_B/D = 1.0$, $\overline{m}_d = 0.25$, $\beta = 1.0$

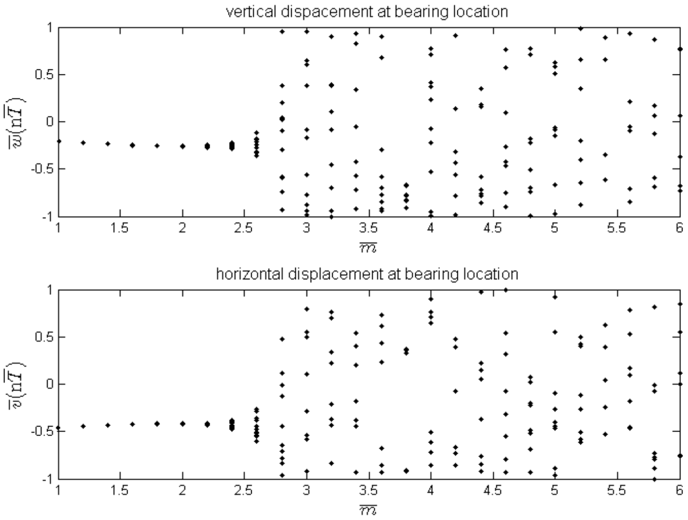

Fig. 4.53: Bifurcation diagram of rotor with $R/2L = 0.01$, $E/(\rho gL) = 2.7\times10^6$, $L_B/D = 1.0$, $\overline{m}_d = 0.25$, $\beta = 3.0$

From the above results the effect of bearing feeding parameter on the bifurcation characteristics of rotor-bearing system is now summarized in Table 4.9.

Table 4.9: Effect of bearing feeding parameter on bifurcation

β	Mass parameter at which bifurcation takes place
0.003	3.0
0.1	3.0
1.0	2.6
3.0	2.4

4.3.4.4 Effect of Ratio of Disk Mass to Shaft mass

An attempt has been made in this section to study the effect of the ratio of disk mass to the shaft mass, $\bar{m}_d = m_d / (\rho AL)$ on the non-linear dynamics of the rotor-bearing system. In this analysis, the non-linear behaviour of a rotor-bearing system is studied for three different values of $\bar{m}_d$ = 0.25, 1.5 and 3.0, when *R/2L* = 0.0125, $\beta = 0.03$ and $E/(\rho gL) = 2.7\times10^6$. Figure 4.32 shows the bifurcation diagram when $\bar{m}_d$ =0.25, whereas Figs. 4.54 and 4.55 depict the bifurcation diagrams with $\bar{m}_d$ = 1.5 and 3.0 respectively. It has been observed that for $\bar{m}_d$ = 0.25, bifurcation takes place at $\bar{m}$ = 4.0 but for $\bar{m}_d$ =1.5, bifurcation starts at $\bar{m}$ =2.0 and for $\bar{m}_d$ =3.0, bifurcation has been observed even at $\bar{m}$ =1.0. Thus, it may be inferred that with increase in $\bar{m}_d$, bifurcation takes place at lower mass parameter.

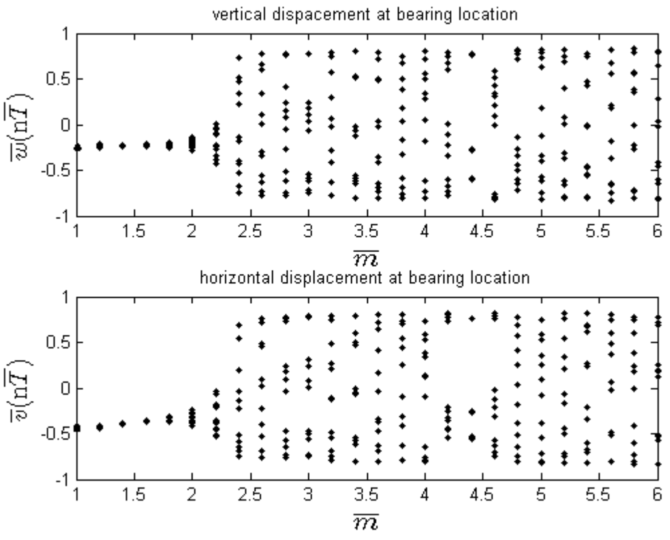

Fig. 4.54: Bifurcation diagram of rotor with $R/2L = 0.0125$, $E/(\rho gL) = 2.7\times10^6$, $L_B/D = 1.0$, $\overline{m}_d = 1.5$, $\beta = 0.03$

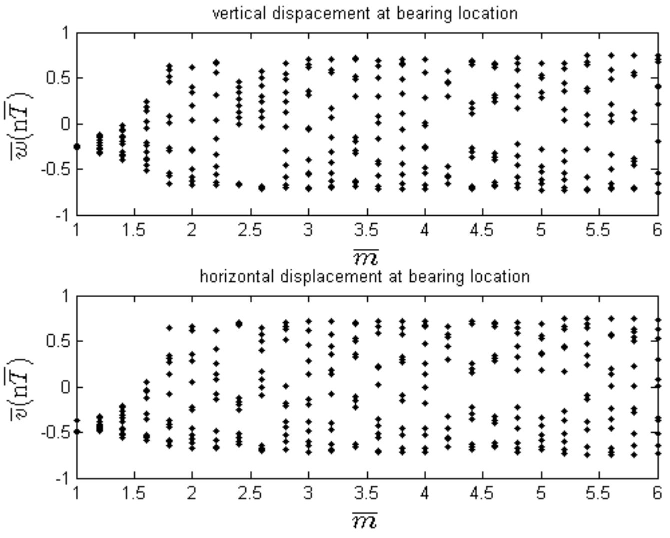

Fig. 4.55: Bifurcation diagram of rotor with $R/2L = 0.0125$, $E/(\rho gL) = 2.7\times10^6$, $L_B/D = 1.0$, $\overline{m}_d$ =3.0, $\beta = 0.03$

Trajectory, time response, Poincaré map and FFT-spectrum of rotor with $\overline{m}_d = 3.0$, $R/2L = 0.0125$, $E/(\rho gL) = 2.7\times10^6$ and $\beta = 0.03$ are depicted in Figs. 4.56-4.59 respectively. It has been observed that for the rotor-bearing parameters $\overline{m}_d =$ 3.0, $R/2L = 0.0125$, $E/(\rho gL) = 2.7\times10^6$ and $\beta = 0.03$, the motion is quasi-periodic throughout the range of $\overline{m}$ =2.0-5.0 as seen in Fig. 4.58. The trajectories and response are seen to be regular for all four values of $\bar{m}$=2.0, 3.0, 4.0 and 5.0. The motion is quasi-periodic throughout the entire range of $\bar{m}$=2.0-5.0 (Fig. 4.58) and also sub-synchronous (Fig. 4.59).

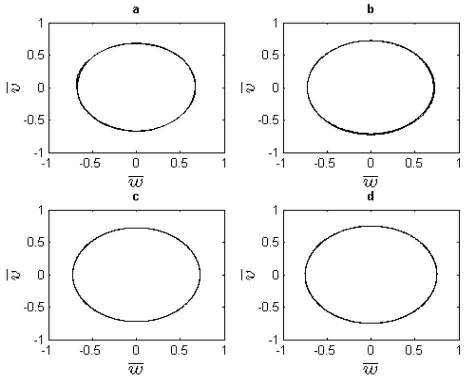

Fig. 4.56: Trajectory at (a) $\bar{m}$=2.0, (b) $\bar{m}$=3.0, (c) $\bar{m}$=4.0, (d) $\bar{m}$=5.0

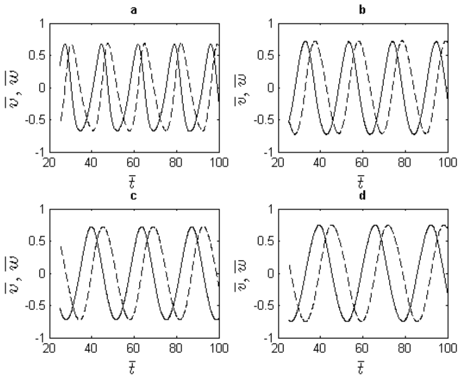

Fig. 4.57: Time response (a) $\bar{m}$=2.0, (b) $\bar{m}$=3.0, (c) $\bar{m}$=4.0, (d) $\bar{m}$=5.0

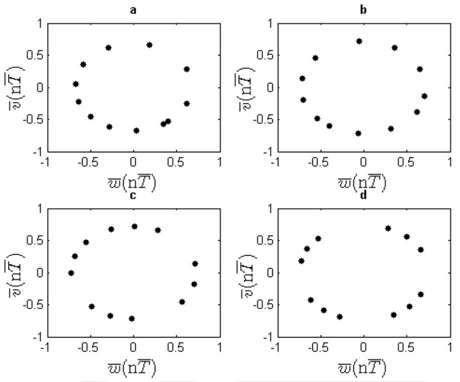

Fig. 4.58: Poincaré map at (a) $\bar{m}$=2.0, (b) $\bar{m}$=3.0, (c) $\bar{m}$=4.0, (d) $\bar{m}$=5.0

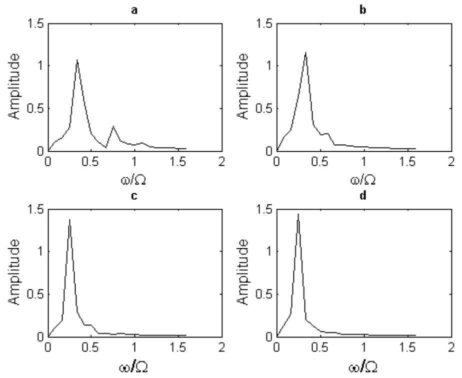

Fig. 4.59: FFT-spectrum at (a) $\bar{m}$=2.0, (b) $\bar{m}$=3.0,(c) $\bar{m}$=4.0, (d) $\bar{m}$=5.0

In the previous study on the effects of the ratio of disk mass to shaft mass on bifurcation characteristics was carried out at lower value of mass parameter, $\beta = 0.03$. The effect of the ratio of disk mass to shaft mass on the bifurcation characteristics is again analyzed at high value of $\beta = 1.0$. Three different ratios of disk mass to shaft mass are chosen, $\bar{m}_d$ = 0.25, 1.5 and 3.0 when $R/2L = 0.0125$, $E/(\rho g L) = 2.7 \times 10^6$, $L_B/D = 1.0$ and $\beta = 1.0$. The bifurcation diagrams are shown in Figs. 4.40, 4.60 and 4.61 respectively. It may be observed that for $\bar{m}_d$ = 0.25, 1.5 and 3.0, the rotor undergoes bifurcation at $\bar{m}$ = 3.0, 1.7 and 1.3 respectively. Thus, like the previous conclusion ($\beta = 0.03$), it may be again inferred that with increase in the ratio of disk mass to shaft mass, the rotor-bearing system undergoes Hopf bifurcation at lower mass parameter.

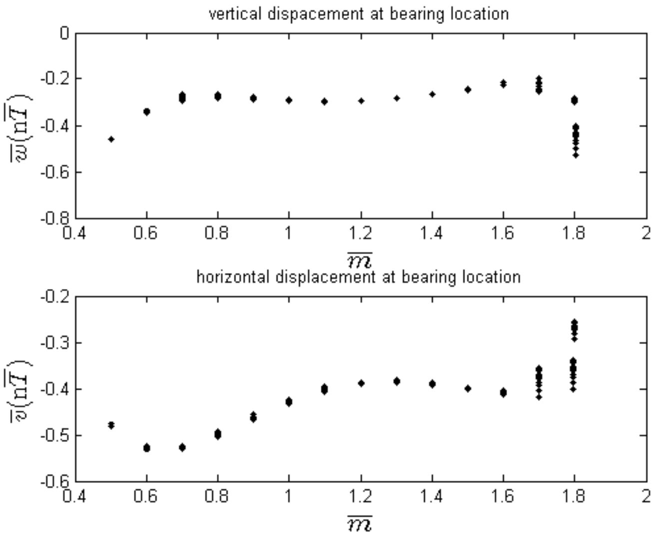

Fig. 4.60: Bifurcation diagram of rotor with $R/2L = 0.0125$, $E/(\rho gL) = 2.7\times10^6$, $L_B/D = 1.0$, $\overline{m}_d = 1.5$, $\beta = 1.0$

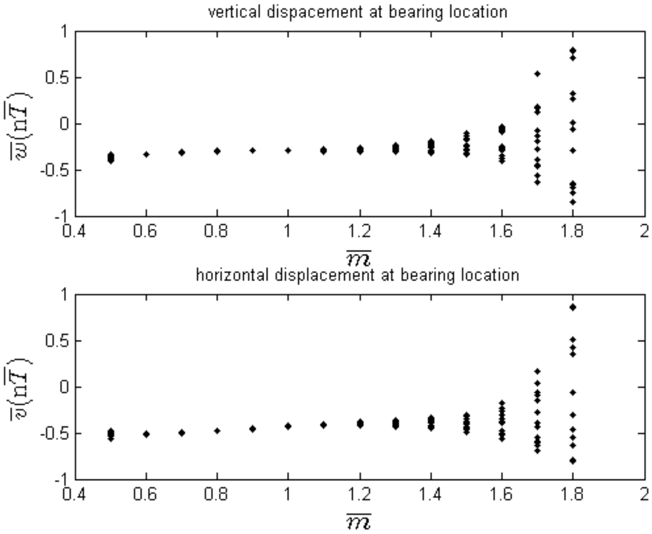

Fig. 4.61: Bifurcation diagram of rotor with $R/2L = 0.0125$, $E/(\rho gL) = 2.7\times10^6$, $L_B/D = 1.0$, $\overline{m}_d = 3.0$, $\beta = 1.0$

Table 4.10 gives the effect of the ratio of disk mass to shaft mass on the bifurcation behaviour of the system for three different values of bearing feeding parameter. It may be inferred that with increase in the ratio of disk mass to shaft mass the system undergoes Hopf bifurcation at lower mass parameter. Also, it may be again seen that as the permeability increases, bifurcation takes place at lower mass parameter.

Table 4.10: Effect of ratio of disk mass to shaft mass on bifurcation

$\bar{m}_d$	Mass parameter at which bifurcation takes place		
	β=0.03	$\beta = 1.0$	$\beta = 3.0$
0.25	4.0	3.0	2.6
1.5	2.0	1.7	1.3
3.0	1.0	1.3	0.8

4.3.4.5 Effect of Bearing Aspect Ratio

Bearing aspect ratio, L_B / D also plays an important role in the non-linear dynamics of rotor-bearing system. Bifurcation diagrams are plotted in Figs. 4.32, 4.62 and 4.63, taking mass parameter as the control parameter with three bearing aspect ratios L_B / D = 1.0, 2.0 and 0.5 respectively when $R/2L$ = 0.0125, $E/(\rho g L) = 2.7 \times 10^6$, $\bar{m}_d$ = 0.25, and $\beta = 0.03$. It has been observed that when L_B / D = 2.0 (Fig. 4.62), the system bifurcates at $\bar{m}$ = 4.2 whereas for L_B / D = 1.0 (Fig. 4.32) and 0.5 (Fig. 4.63) bifurcations occur at $\bar{m}$ = 4.0 and 3.6 respectively. Thus, from bifurcation diagrams generated for different L_B / D ratios along with Figs. 4.32, 4.62 and 4.63 it may be inferred that with increase in bearing aspect ratio, bifurcation takes place at higher mass parameter.

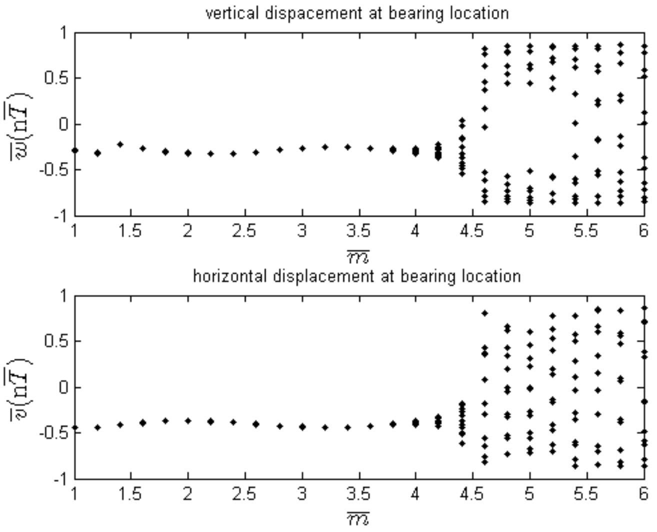

Fig. 4.62: Bifurcation diagram of rotor with $R/2L = 0.0125$, $E/(\rho g L) = 2.7\times10^6$, $L_B/D = 2.0$, $\overline{m}_d = 0.25$, $\beta = 0.03$

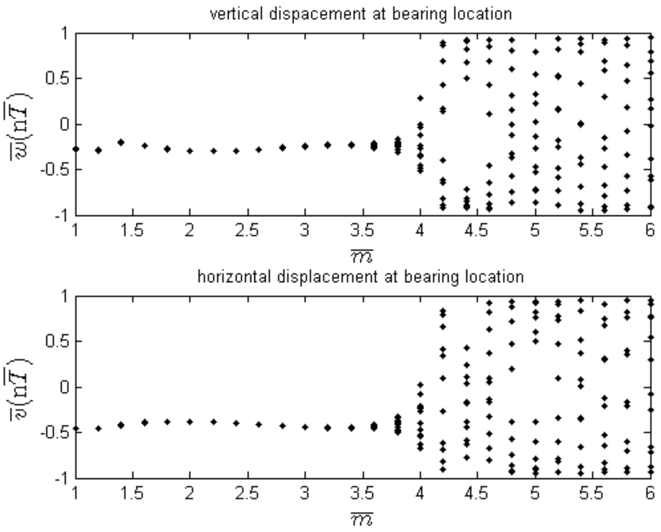

Fig. 4.63: Bifurcation diagram of rotor with $R/2L = 0.0125$, $E/(\rho g L) = 2.7\times10^6$, $L_B/D = 0.5$, $\overline{m}_d = 0.25$, $\beta = 0.03$

The effect of different bearing aspect ratio on bifurcation of the system is now tabulated in Table 4.

Table 4.11: Effect of bearing aspect ratio on bifurcation

L_B / D	Mass parameter at which bifurcation takes place
0.5	3.6
1.0	4.0
2.0	4.2

4.4 Summary

The present analysis deals with non-linear dynamic behaviour of an unbalanced flexible rotor supported by two porous oil bearings. The bearings are represented by non-linear oil-film forces and a finite element model of the flexible rotor based on Timoshenko beam theory is considered. Further, the whole analysis is carried out in a non-dimensional form, with an aim to identify different non-dimensional parameters of the rotor-bearing system that are having significant effect on the dynamics of the system. Waterfall diagrams and bifurcation diagrams are generated by varying these non-dimensional parameters to study the effects of these parameters on the dynamics of the rotor-bearing system. The following inferences are drawn from the waterfall diagrams:

- High value of bearing feeding parameter results in high amplitude of oil-whirl. Therefore, to avoid high amplitude of vibration, permeability of the porous bush should be low.
- Mass parameter at which oil-whirl appears increases with the increase in slenderness ratio of the rotor. Therefore, high value of slenderness ratio ensures safe running of the system.
- As the stiffness parameter increases the oil-whirl appears at higher speed. Thus, high stiffness parameter benefits safe operation of the rotor-bearing system.
- Increase in the ratio of disk mass to shaft mass results in appearance of oil-whirl at low spin speeds with high amplitude of vibration. Therefore, this ratio should be kept low for stable operation of the system.

From bifurcation analysis of flexible rotor supported on fluid-film bearing the following conclusions may be drawn.

- With increase in bearing feeding parameter, bifurcation of the system takes place at lower mass parameter.
- As the slenderness ratio of the rotor increases, the rotor-bearing system undergoes Hopf bifurcation at higher mass parameter.
- Increase in stiffness parameter results in bifurcation taking place at higher mass parameter.
- Bifurcation takes place at higher mass parameter as the bearing aspect ratio increases.
- With increase in the ratio of disk mass to shaft mass, the rotor-bearing system undergoes bifurcation at lower mass parameter.

CHAPTER 5

Effect of Tangential Velocity Slip on Stability and Dynamic Response of a Flexible Rotor Supported on Porous Bearing

---

5.0 Introduction

In the previous chapters, analysis of rotors supported on porous journal bearings have been carried out with an assumption that the lubricating fluid enters the clearance space of the bearing with a zero tangential velocity at the porous medium. However, earlier investigations suggest that this assumption is at best an approximation only. Beavers and Joseph [92] proposed an alternative boundary condition which admits a non-zero tangential velocity (so-called slip velocity) at the porous surface. They assumed that slip velocity for the free fluid is proportional to the shear rate at the porous boundary. Many investigators [97-100] have studied the effect of velocity slip given by the Beavers-Joseph condition both theoretically and experimentally.

In the present chapter a flexible rotor supported on two porous oil bearings of finite length with velocity slip has been considered. The mathematical formulation of the rotor-bearing system is given in chapter 2. However, the differential equations for the porous bearing with slip are little different from which was mentioned in chapter 2 and these are given in the following section. Stability curves are drawn for different slip parameters and the effect of velocity slip on waterfall diagram and bifurcation characteristics is also investigated.

5.1 Governing Equation of Porous Oil Bearing with Tangential Velocity Slip

The schematic diagram of a porous oil bearing is shown in Fig. 2.2. The non-dimensional governing differential equations for the porous bearing considering Beavers-Joseph criterion for velocity slip are given below [38]:

For the porous bush:

$$\mathrm{K}_x \frac{\partial^2 \overline{p}'}{\partial \theta^2} + \left(\frac{R}{H}\right)^2 \frac{\partial^2 \overline{p}'}{\partial \overline{y}^2} + \left(\frac{D}{L_B}\right)^2 \mathrm{K}_z \frac{\partial^2 \overline{p}'}{\partial \overline{z}^2} = 0 \tag{5.1}$$

For the clearance space:

$$\frac{\partial}{\partial\theta}\left[\bar{h}^{3}(1+\xi_x)\frac{\partial\bar{p}}{\partial\theta}\right]+\left(\frac{D}{L_B}\right)^{2}\frac{\partial}{\partial\bar{z}}\left[\bar{h}^{3}(1+\xi_z)\frac{\partial\bar{p}}{\partial\bar{z}}\right]=6(1+\xi_{ox})\frac{\partial\bar{h}}{\partial\theta}-12\left(\frac{\partial\phi}{\partial\bar{t}}\right)\left(\frac{\partial\bar{h}}{\partial\theta}\right)+12\frac{\partial\bar{h}}{\partial\bar{t}}+\beta\left(\frac{\partial\bar{p}'}{\partial\bar{y}}\right)_{\bar{y}=0} \tag{5.2}$$

Where,

$$\xi_x=\frac{3\left[\sigma_x\bar{h}+2\alpha\right]}{\sigma_x\left[\bar{h}+\alpha\bar{h}^{2}\sigma_x\right]};\ \xi_z=\frac{3\left[\sigma_z\bar{h}+2\alpha\right]}{\sigma_z\left[\bar{h}+\alpha\bar{h}^{2}\sigma_z\right]};\xi_{ox}=\frac{1}{1+\alpha\bar{h}\sigma_x};\ \sigma_x=\frac{C}{\sqrt{k_x}};\sigma_z=\frac{C}{\sqrt{k_z}}\ \text{and}$$

α is the slip coefficient.

The boundary conditions are the same as mentioned in section 2.4.2.

5.2 Effect of Velocity Slip on the Stability of a Flexible Rotor

The effect of velocity slip on the stability of a flexible rotor is carried out following the method described in section 3.3. The effect of tangential velocity slip on the stability of the rotor can be studied from Fig. 5.1. The critical mass parameter is plotted against Sommerfeld number for three different values of slip coefficients (α=0.1, 10 and 100) as depicted in Fig. 5.1. It can be observed that with increase in slip parameter critical mass parameter increases. Thus it may be inferred that stability improves with increase in velocity slip.

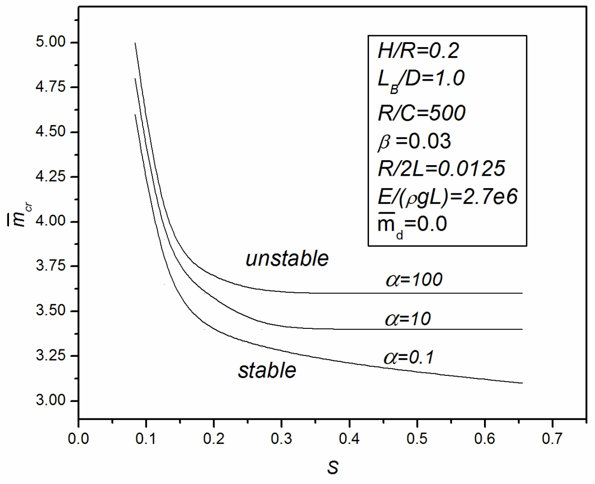

Fig. 5.1: Stability map ($\bar{m}_{cr}$ versus S) for different values of slip coefficient α

5.3 Effect of Slip on Nonlinear Dynamic Response of a Flexible Rotor

The non-linear dynamic response of a rotor-bearing system under unbalance condition is very much important. In the present section an unbalanced rotor supported by two hydrodynamic porous oil bearings with slip is considered. Waterfall diagrams are generated to study the dynamics of the rotor-bearing system. Further, Bifurcation diagrams, Poincaré maps, time response, journal trajectories and FFT-spectrum etc. are obtained to study the non-linear dynamics of the rotor-bearing system. The effect of velocity slip on the dynamic response of the rotor-bearing system is then analyzed.

The effect of slip coefficients on the dynamics of rotor-bearing can be studied by changing its value while other parameters are kept constant as shown in Figs. 5.2 through 5.5. Waterfall diagrams are obtained for four different values of slip coefficients, α=0.0, 0.1, 10.0 and 100.0 when $R/2L = 0.0125$, $E/(\rho g L) = 2.7\times10^{6}$, e_d/C=0.25, $\overline{m}_d$=1.5, L_B/D=1.0 and β=0.03 . It has been observed from Figs. 5.2 through 5.5 that for all four values of slip coefficients oil-whirl starts at $\overline{m}$=1.8. No significant change in the dynamics of rotor-bearing system is observed as the slip coefficient is varied. Thus, it may be inferred that slip has little effect on the dynamic behaviour of the rotor-bearing system.

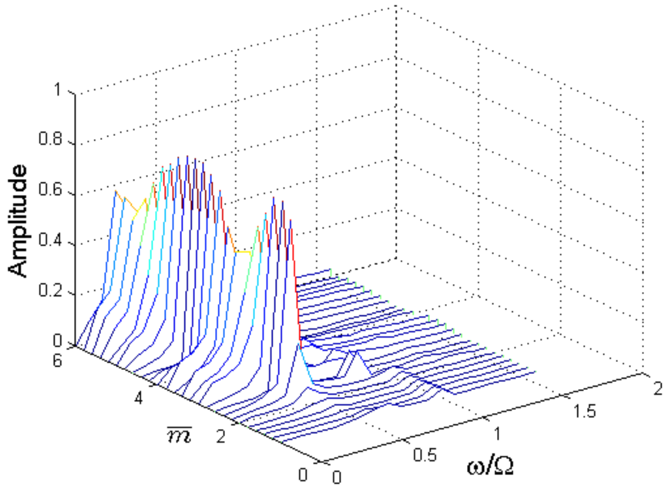

Fig. 5.2: Waterfall diagram of rotor during run-up with, α=0.0

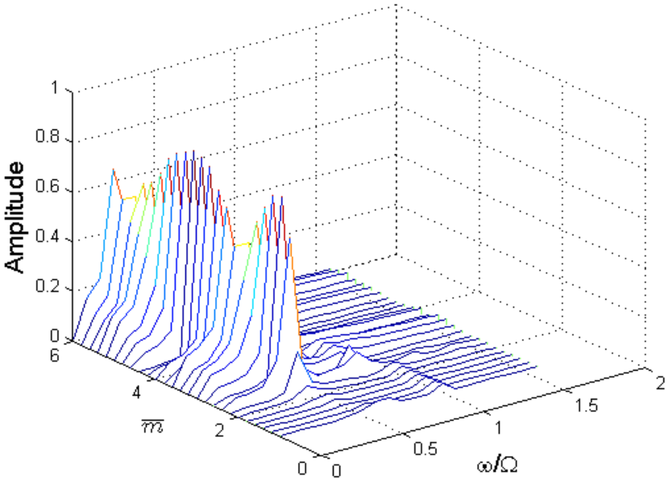

Fig. 5.3: Waterfall diagram of rotor during run-up with α =0.1

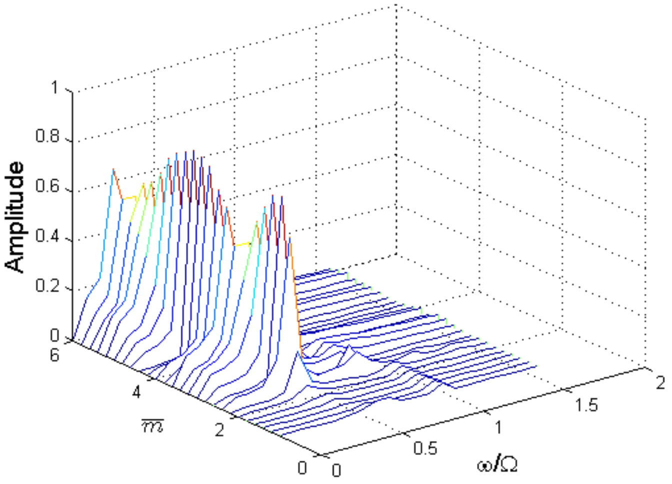

Fig. 5.4: Waterfall diagram of rotor during run-up with, α =10.0

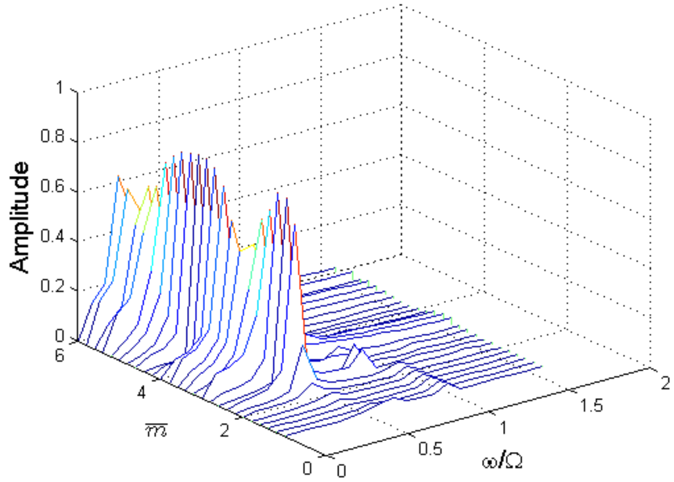

Fig. 5.5: Waterfall diagram of rotor during run-up with α =100

Similar to the previous analysis the effect of slip is further analyzed for higher bearing feeding parameter value of $\beta = 1.0$. Waterfall diagrams are obtained for α = 0.0, 0.1, 10 and 100 when the other non-dimensional parameters are as follows: $R/2L = 0.0125$, $E/(\rho gL) = 2.7\times10^6$, e_d/C=0.25, $\overline{m}_d$=3.0, L_B/D=1.0 and β=1.0. The corresponding waterfall diagrams are shown in Figs. 5.6 through 5.9. It may be observed that for all values of slip parameter, α, oil-whirl starts at $\overline{m}$ = 1.4. Thus, it may be concluded that slip has no or little effect on the dynamic behaviour of the system under unbalance excitation. The same trend was observed in case of $\beta = 0.03$

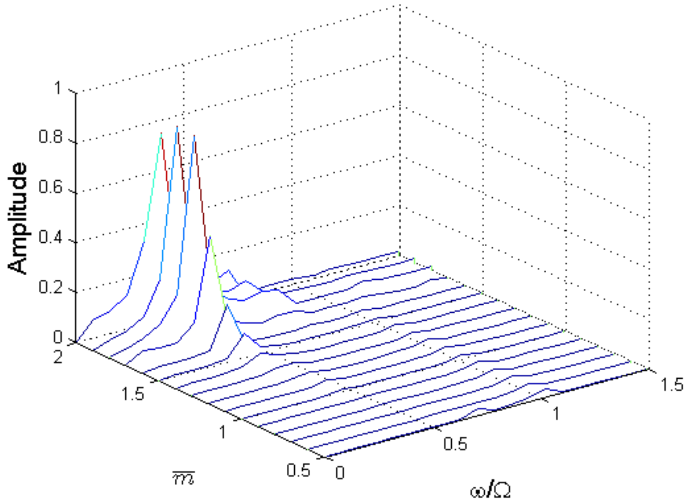

Fig. 5.6: Waterfall diagram of rotor during run-up with α =0.0

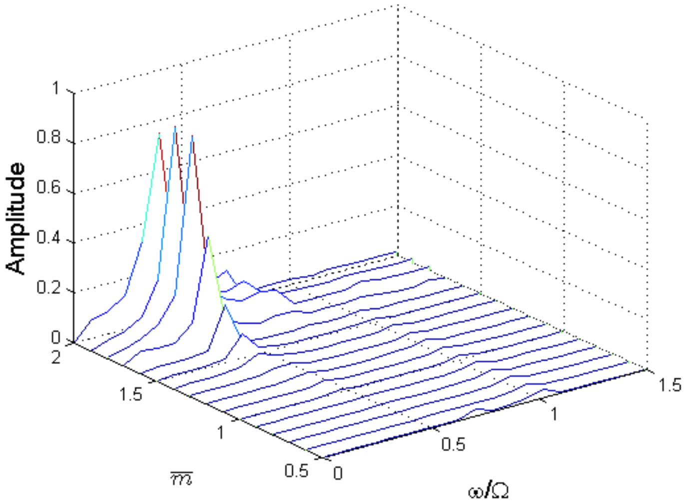

Fig. 5.7: Waterfall diagram of rotor during run-up with α =0.1

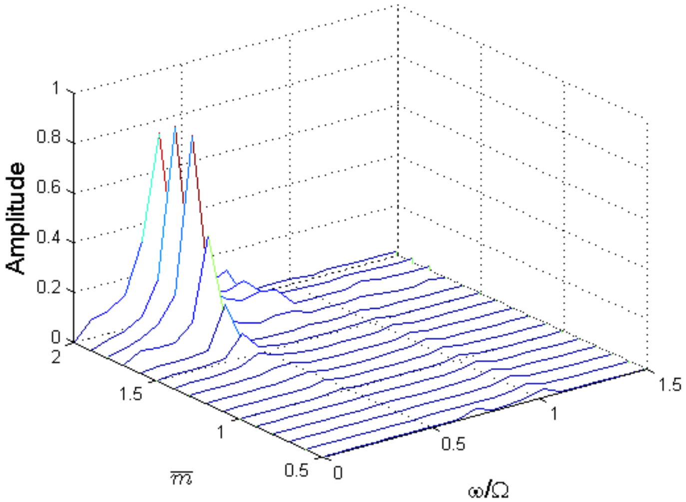

Fig. 5.8: Waterfall diagram of rotor during run-up with α =10.0

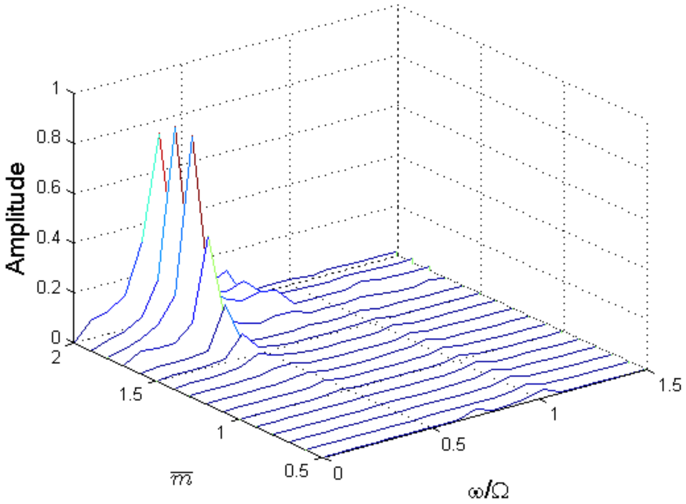

Fig. 5.9: Waterfall diagram of rotor during run-up with α =100.0

The effect of the ratio of slip on the appearance of oil-whirl has been is tabulated in Table 5.1. It has been observed from Table 5.1 that for all values of ,α oil-whirl appears at same value of mass parameter. Also, it may be again observed that oil-whirl appears at lower mass parameter as β increases.

Table 5.1: Effect of slip parameter on appearance of oil-whirl

α	Mass parameter at which oil whirl appears during run-up	
	$\beta = 0.03$	$\beta = 1.0$
0	1.8	1.4
0.1	1.8	1.4
10	1.8	1.4
100	1.8	1.4

In this analysis, the effect of the slip coefficient on the bifurcation characteristics is also studied for four different values of slip, α=0.0, 0.1, 10 and 100.0, when *R/2L*=0.0125, $\beta = 0.03$ and $E/(\rho g L) = 2.7\times10^{6}$. Figures 5.10, 5.11 5.12 and 5.13 show the bifurcation diagrams for α = 0.0, 0.1, 10 and 100.0 respectively.

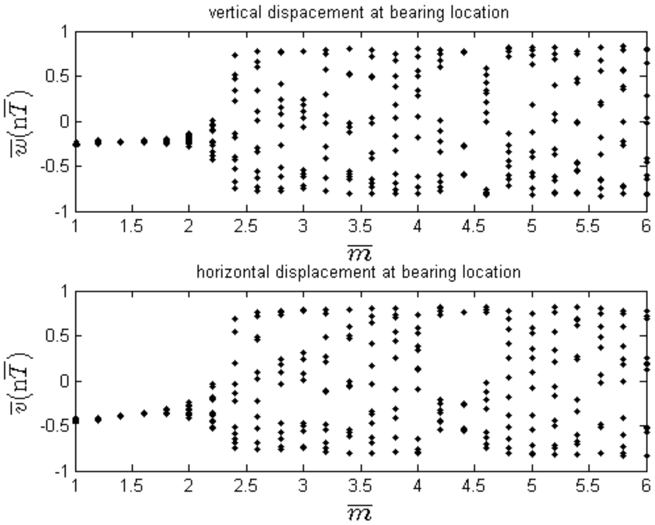

Fig. 5.10: Bifurcation diagram of rotor with α =0.0

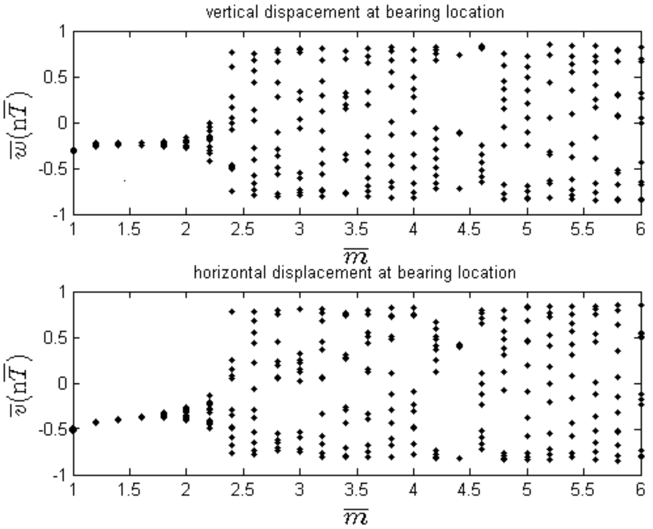

Fig. 5.11: Bifurcation diagram of rotor with α =0.1

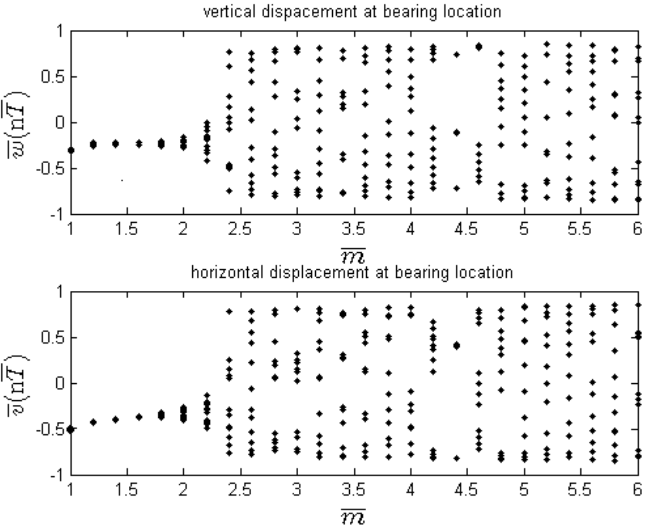

Fig. 5.12: Bifurcation diagram of rotor with α=10

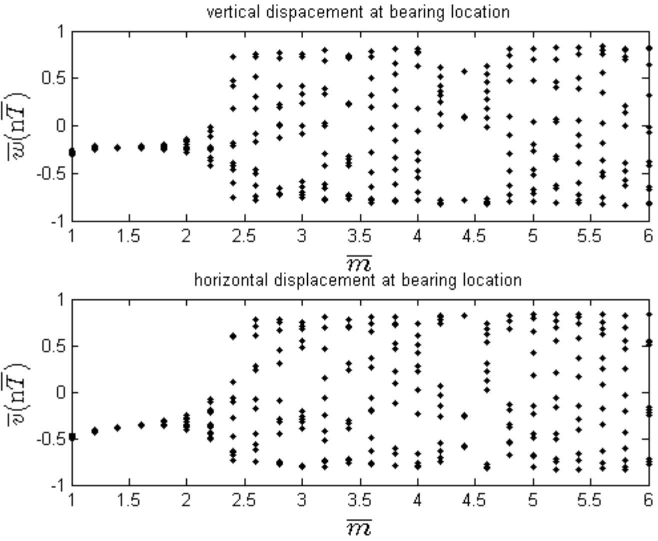

Fig. 5.13: Bifurcation diagram of rotor with α=100

It has been observed that for all the four values of α, bifurcation takes place at $\bar{m}$=2.0. Thus it is evident that velocity slip does not have any significant effect on the bifurcation characteristics of the rotor-bearing system.

Trajectory, time response, Poincaré map and FFT-spectrum of rotor with $R/2L = 0.0125$, $\bar{m}_d$=1.5, $E/(\rho g L) = 2.7\times 10^6$, $\beta = 0.03$ and α=100 are shown in Figs. 5.14-5.17 respectively. The trajectories and response is asynchronous at $\bar{m}$=2.0 but afterward becomes regular (Figs. 5.14-5.15). It has also been observed that for the above rotor-bearing parameters the motion is quasi-periodic throughout the range of $\bar{m}$=2.0-5.0 as seen in Fig. 5.16. Further, the rotor whirl motion is sub-synchronous (Fig. 5.17).

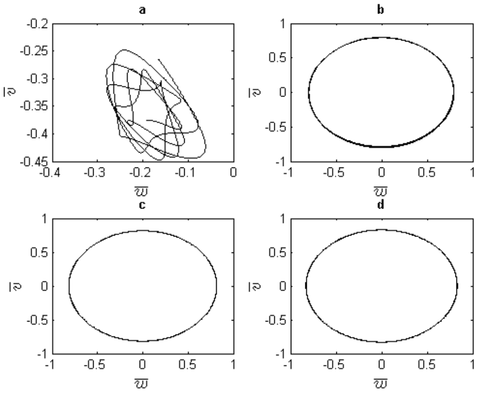

Fig. 5.14: Trajectory at (a) $\bar{m}$=2.0, (b) $\bar{m}$=3.0, (c) $\bar{m}$=4.0, (d) $\bar{m}$=5.0

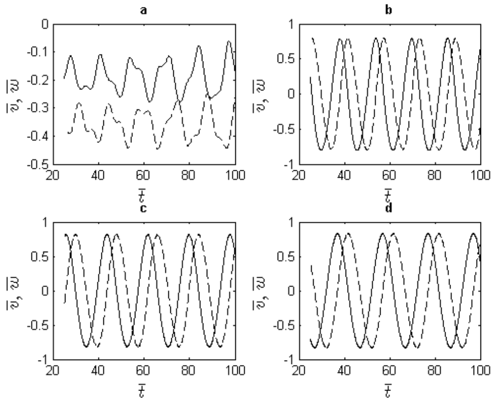

Fig. 5.15: Time response (a) $\bar{m}$=2.0, (b) $\bar{m}$=3.0, (c) $\bar{m}$=4.0, (d) $\bar{m}$=5.0

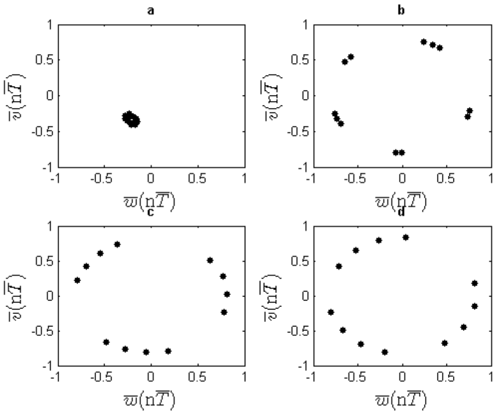

Fig. 5.16: Poincaré map at (a) $\bar{m}$=2.0, (b) $\bar{m}$=3.0, (c) $\bar{m}$=4.0, (d) $\bar{m}$=5.0

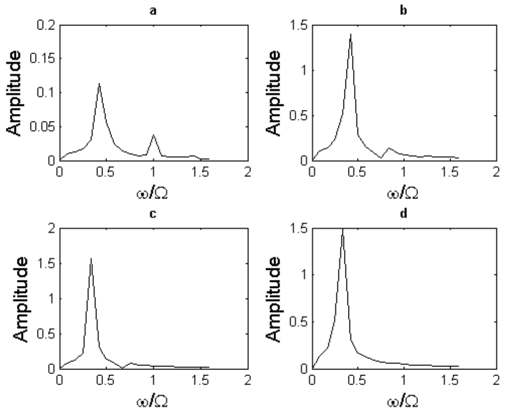

Fig. 5.17: FFT-spectrum at (a) $\bar{m}$=2.0, (b) $\bar{m}$=3.0,(c) $\bar{m}$=4.0, (d) $\bar{m}$=5.0

The effect of slip on bifurcation characteristics can be again analyzed at higher value of $\beta = 1.0$. Bifurcation diagrams are plotted for four values of slip parameters α= 0.0, 0.1, 10 and 100 and the corresponding figures are shown in Figs. 5.18 through

5.19 respectively. The bifurcation diagrams are obtained for the following parameters: $R/2L = 0.0125$, $E/(\rho g L) = 2.7\times10^{6}$, e_d/C=0.25, $\bar{m}_d$=3.0, L_B/D=1.0 and β=1.0. It may be seen from the bifurcation diagrams that for all values of slip parameter, α, the rotor-bearing system undergoes Hopf bifurcation at $\bar{m}$=1.4. Thus, even at high value of bearing feeding parameter, β=1.0 slip coefficient does not have any significant effect on the bifurcation characteristics of rotor-bearing system.

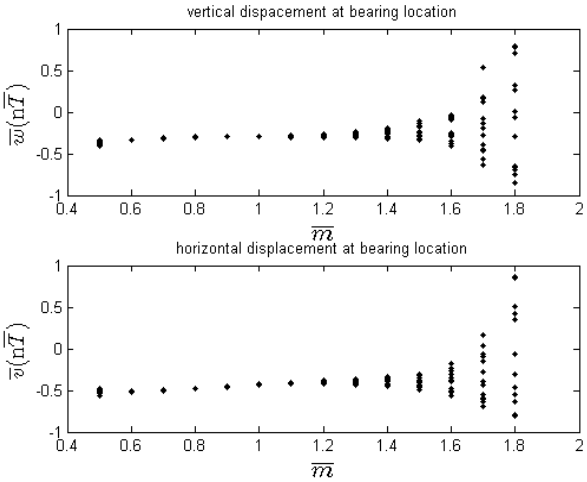

Fig. 5.18: Waterfall diagram of rotor during run-up with α=0.0

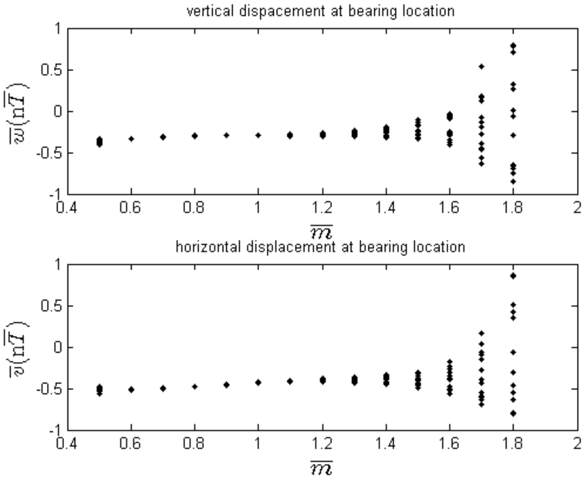

Fig. 5.19: Waterfall diagram of rotor during run-up with α=0.1

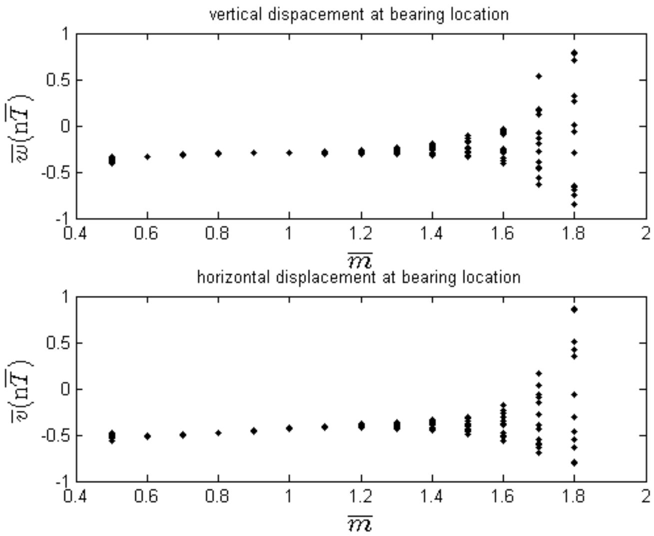

Fig. 5.20: Waterfall diagram of rotor during run-up with α =10.0

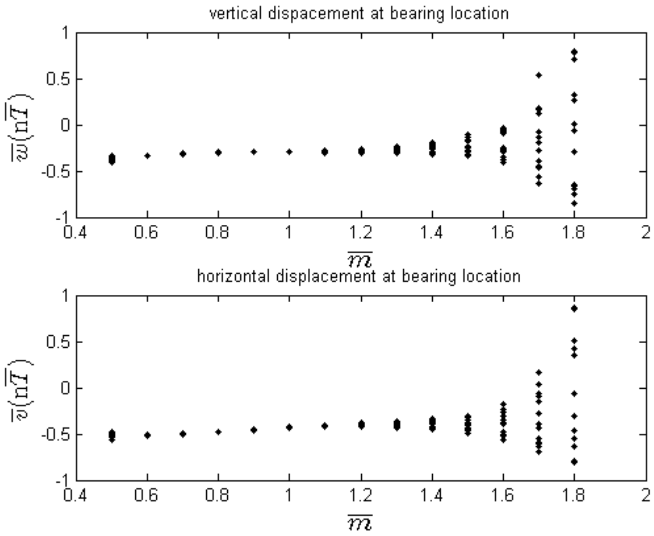

Fig. 5.21: Waterfall diagram of rotor during run-up with α =100.0

Table 5.2 summarizes the effect of slip parameter on bifurcation characteristics of rotor-bearing system. It may be seen from Table 5.2, bifurcation occurs at same mass parameter as the slip parameter increases for all values of bearing feeding parameter. Also, like previous cases, with increase in bearing feeding parameter, bifurcation takes place at lower mass parameter.

Table 5.2: Effect of slip parameter on bifurcation

α	Mass parameter at which bifurcation takes place	
	$\beta = 0.03$	$\beta = 1.0$
0	2.0	1.4
0.1	2.0	1.4
10	2.0	1.4
100	2.0	1.4

5.4 Summary

The present chapter deals with the effect of tangential velocity slip of porous oil bearing on the stability and non-linear dynamic response of a flexible rotor. Because of tangential velocity slip there is a migration of fluid tangent to the boundary within the porous medium. There is some net tangential drag due to the transfer of forward momentum across this permeable boundary.

The following inferences may be drawn from the above analysis:

- Increase in slip parameter results in better stability of rotor-bearing system.
- Velocity slip has no significant effect on the non-linear dynamic responses of the rotor-bearing system.

CHAPTER 6

Concluding Remarks

6.0 Introduction

The thesis deals with analysis of stability and unbalance response of a flexible rotor supported by two identical finite porous journal bearings. Based on the literature review presented in Chapter 1, the scope of the present work has been drawn. It is noteworthy that most of the investigations carried out earlier are either based on rigid rotor assumption or the bearing is based on short or long bearing approximation. In some cases simplified flexible model of the rotor, such as Jeffcott rotor is considered. In view of this, a methodology has been proposed to investigate stability as well as unbalance response of a rotor supported on porous hydrodynamic bearings. The present study takes up a finite element model of a flexible rotor, using Timoshenko beam theory as presented in chapter 2. The non-linear effects of fluid-film forces are incorporated in the simulation. Further, the equation of motion of the rotor has been presented in non-dimensional form. The mathematical model of the rotor-bearing system and solution procedure are also provided in the chapter. While carrying out stability analysis of a fully balanced rotor using a non-linear transient method, as presented in chapter 3, the effects of different non-dimensional parameters on the stability characteristics have been discussed. A thorough investigation on the dynamic behaviour of the unbalanced rotor system has been presented in chapter 4. Waterfall diagrams and bifurcation diagrams are generated to get a glimpse of the dynamical nature of the system. The study carried out depicts the effects of different non-dimensional parameters on the dynamic behaviour of the rotor-bearing system. Tangential slip velocity in porous bearing was ignored in the study presented in these chapters. However, the effect of velocity slip in porous bearing on stability map and dynamic characteristics of the rotor has been investigated and presented in chapter 5.

Some of the advantages of the methodology developed are as follows:

- ➢ The methodology developed to simulate a flexible rotor supported on two porous journal bearing taking into consideration a finite bearing solution instead of either hypothetical bearing or approximate (short or long bearing) solution of bearing. Therefore, the results presented here would be more practical and reliable.

- A non-dimensional parametric study has been carried out and therefore, the effect of the non-dimensional parameters can be studied. Further, the non-dimensional results has been utilized to study a wide range of combination of rotor-bearing system having different lengths, diameters, loads, material, eccentricity, speed, porosity of the bearing etc.
- In the non-dimensionalization scheme adopted in the present methodology, two new parameter are obtained which are stiffness parameter, $E/(\rho g L)$ and ratio of disk mass to shaft mass, $m_d/(\rho A L)$. It can be observed that these parameters have profound effect on the stability and dynamic response of the rotor-bearing system.
- The methodology has the advantage of tracing the trajectories at any location of the rotor and thereby the behaviour of the rotor can be studied in detail.
- Even though the porous bearings are considered in the analysis, it is possible to incorporate any other type of hydrodynamic bearings instead of porous bearings. This gives the flexibility to the methodology for simulation of different combination of rotor-bearing system.
- Another important issue worth mentioning that the methodology also allows studying not only the effect of hydrodynamic bearings, but also the effect of the unbalance of the rotor.
- The oil-whirl and whip phenomena can be studied from the model developed here. The dynamic behaviour of the rotor-bearing system during speed-ascending and speed-descending can also be studied.

6.1 Important Results

- High value of slenderness ratio ensures better stability of the rotor. Also rotor spin speed at which oil-whirl appears increases with the increase in slenderness ratio of the rotor. Therefore, high value of slenderness ratio ensures safe running of the system.

- Higher the stiffness parameter, the better is the stability. As the stiffness parameter increases, the oil-whirl appears at higher speed. Thus, high stiffness parameter benefits safe operation of the rotor-bearing system.
- Stability deteriorates with the increase in the ratio of disk mass to shaft mass. Increase in the ratio of disk mass to shaft mass results in oil-whirl appearing in low speeds as well as high amplitude of vibration. Therefore, this ratio should be kept low to ensure stable operation of the system.
- Permeability of the porous bush adversely affects the stability of rotor-bearing system. High permeability results in deterioration of stability. High value of bearing feeding parameter results in high amplitude of oil-whirl. Therefore, to avoid high amplitude of vibration, permeability of the porous bush should be low.
- With increase in slip velocity, stability of rotor improves. However, no significant difference in dynamic behaviour is observed as the slip coefficient is varied.
- Stability of the rotor-bearing system improves with the increase of bearing aspect ratio.
- Overhung rotors have better stability than rotors supported at the ends.
- At low spin speed unbalance forces are dominant and as the speed increases oil-film forces takes over as the major cause of vibration in rotor system. Thus, the whirling of the rotor gradually changes from synchronous to sub-synchronous.

Apart from above advantages the present analysis also substantiates the following established results such as:

- Critical values of mass parameter are estimated, rotor operating below this mass parameter are stable and operating above becomes unstable [21, 22, 37].
- Flexible rotor threshold speed approaches to rigid rotor threshold speed at slenderness ratio higher than 0.067 [31].
- In the presence of residual unbalance the rotor can have synchronous whirl when the mass parameter value is low [35-36].
- Rotor-bearing system shows distinct behaviour in run-up and run-down. Oil whirl during run-down disappears at a speed lower than the speed at which it appeared during run-up [11-12, 35-36].

- Rotor-bearing system undergoes Hopf bifurcation as the spin speed increases [35-37].

6.2 Scope for Future Works

- In the mathematical modelling of the rotor-bearing system bearing misalignment is neglected. However due to the bending and shear effect there is a possible misalignment of the rotor and therefore, pressure distribution about the axial direction may not be symmetrical. The issue may be taken up in future study to ascertain the effect of misalignment.
- The effect rotor acceleration or deceleration on the dynamic response, in particular, on the hysteresis phenomena of the rotor-bearing system can be studied in more detail.
- The model developed can be used to study the onset of chaotic motion in rotor-bearing system.
- The model can be used to study the effects of non-identical bearings and asymmetric location of disks and bearings.

6.3 Summary

An attempt has been made in this thesis to study stability and unbalance response of a flexible rotor supported by two porous bearings. Some insights about the stability and safe operation of the rotor are obtained. Further, the whole analysis is carried out in non-dimensional form. So, a wide range of rotor-bearing configuration can be studied utilizing the presented results. It is hoped that the study presented here would be useful to correlate design configuration and operating conditions of rotor-bearing system. In view of the above, it may be concluded that the results generated by the proposed methodology would be very much useful for rotor-bearing designers as well as maintenance engineers.

References

---

[1] Baxter, N. L., "Case Studies from 25 Years of Troubleshooting Vibration Problems", *ASM International*, 2001, pp. 51-68.

[2] Guy, K., R., "Industrial Case Histories: Who is to Blame?" *Journal of Failure Analysis and Prevention*, 2008, Vol. 8, pp. 111-144.

[3] Newkirk, B. L. and Taylor H. D., "Shaft Whipping due to Oil Action in Journal Bearings," *General Electrical Review*, 1925, Vol. 28, pp. 559-568.

[4] Newkirk, B. L., "Whirling Balanced Shafts", *Third International Congress, Applied Mechanics*, Sweden, 1930.

[5] Hagg, A. C., "The Influence of Oil-Film Journal Bearings on the Stability of Rotating Machines", *ASME Transaction: Journal of Applied Mechanics*, 1946, Vol. 68, pp. 211-220.

[6] Hori, Y., "A Theory of Oil Whip," *ASME Transaction: Journal of Applied Mechanics*, 1959, Vol. 26, pp. 189-198.

[7] Pinkus, O., "Experimental Investigation of Resonant Whip," *ASME Transaction*, 1956, July, Vol. 78, 1956, pp. 975-983.

[8] Ehrich, F. F., Subharmonic Vibration of Rotors in Bearing Clearance, *ASME Transaction: Journal of Engineering for Power*, 1966, Vol. 88, pp. 56–65.

[9] Lund., J. W., "Stability and Damped Critical Speeds of a Flexible Rotor in Fluid-Film Bearings", *ASME Transaction: Journal of Engineering for Industry*, 1974, Series B, Vol. 96(2), pp. 509-517.

[10] Lund., J. W., "Modal Response of a Flexible Rotor in Fluid-Film Bearings", *ASME Transaction: Journal of Engineering for Industry*, 1974, Series B, Vol. 96(2), pp. 525-533.

[11] Muszynska, A., "Whirl and Whip- Rotor/Bearing Stability Problems" *Journal of Sound and Vibration*, 1986, Vol. 110(3), pp. 443-462.

[12] Muszynska, A., "Stability of Whirl and Whip in Rotor/Bearing Systems" *Journal of Sound and Vibration*, 1988, Vol. 127(1), pp. 49-64.

[13] Hagg, A. C. and Warner P. C., "Oil Whip of Flexible Rotors", ASME Transaction, 1953, Vol. 75(7), pp. 1339-1344.

[14] Holmes, R., "The Role of Oil-Film Bearings in Promoting Shaft Instability and the Remedial Effect of Damping", *Tribology International*, 1980, 13, pp. 243-248.

[15] Manfrida, G. and Martelli F., "A Finite Element non-linear Stability Analysis for Journal Bearings", *Meccanica*, 1980, Vol. 15(1), pp. 47-53.

[16] Rao, J. S., "Instability of Rotors Mounted in Fluid-Film Bearings with a Negative Cross-coupled Stiffness Coefficient", *Mechanism and Machine Theory*, 1985, Vol. 20(3), pp. 181-187.

[17] Akers, A., Michaelson, S., and Cameron, A., "Stability Contours for a Whirling Finite Journal Bearing", *ASME Transaction: Journal of Lubrication Technology*, 1971, Vol. 93(1), pp. 177-190.

[18] Kirk, R. G. and Gunter E. J., "Short Bearing Analysis Applied to Rotor-Bearing Dynamics, Part 1: Theory", *ASME Transaction: Journal of Lubrication Technology*, 1976, Vol. 98, pp. 47-56.

[19] Kirk, R. G. and Gunter E. J., "Short Bearing Analysis Applied to Rotor-Bearing Dynamics, Part 2: Results of Journal Bearing Response", *ASME Transaction: Journal of Lubrication Technology*, 1976, Vol. 98, pp. 319-329.

[20] Sinhasan, R. and Goyal, K. C., "Transient Response of a Circular Journal Bearing Lubricated with Non-Newtonian Lubricants", *Wear*, 1992, Vol. 156, pp. 385-399.

[21] Kumar, A. and Rao, N. S., "On the Stability of a Rigid Rotor in Turbulent Finite Hydrodynamic Journal Bearings", *Wear*, 1992, 154, pp. 11-21.

[22] Kumar, A. and Rao, N. S., "Stability of a Rigid Rotor in Turbulent Hybrid Porous Journal Bearings", *Tribology International*, 1994, pp. 299-305.

[23] Pai, R. and Majumdar B. C., "Stability of Submerged Oil Journal Bearings under Dynamic Load, *Wear*, 1991, 146, pp. 125-135.

[24] Raghunandana, K. and Majumdar B. C., "Stability of Journal Bearing Systems using non-Newtonian Lubricants: a Non-linear Transient Analysis", *Tribology International*, 1999, 32, pp. 179-184.

[25] Kakoty, S. K. and Majumdar B. C., "Effect of Fluid Inertia on Stability of Oil Journal Bearings", *ASME Transaction: Journal of Tribology*, 2000, Vol. 122, pp. 741-745.

[26] Kakoty, S. K. and Majumdar B. C., "Effect of Fluid Inertia on Dynamic Coefficients and Stability of Journal Bearings", *Proceedings of IMechE, Journal of Engineering Tribology*, Vol. 214, Part J, 229 - 242.

[27] Kakoty, S. K. and Majumdar B. C., "Effect of Fluid Inertia on Stability of Flexibly Supported Oil Journal Bearings: Linear Perturbation Analysis", *Tribology International*, 1999, 32, pp. 217 – 228.

[28] Kakoty, S. K. and Majumdar B. C., "Effect of Fluid Inertia on Stability of Flexibly Supported Oil Journal Bearings: A non-Linear Transient Analysis", *STLE Tribology Transactions*, 2002, Vol. 45(2), pp. 253 - 257.

[29] Kakoty, S. K. and Kalita, M., "Stability of Rotors Supported on Fluid Film Bearings", *Second International Conference on Vibration Engineering and Technology of Machinery* (VETOMAC-2), 16-18 Dec., 2002, Mumbai, India.

[30] Kalita, M. and Kakoty, S. K., "Regarding Stability Study of Circular and Non-circular Bearings Supporting Rigid and Flexible Rotors". *Advances in Vibration Engineering*, Vol. 6(4). pp. 371-381.

[31] Kalita, Madhumita, "Dynamic Characteristics and Stability Analysis of Rotors Mounted on Fluid Film Bearings", *Ph.D dissertation,* IIT Guwahati, 2005.

[32] Chen, W. J., "Instability Threshold and Stability Boundaries of Rotor-Bearing Systems", *ASME Transaction: Journal of Engineering for Gas Turbine and Power*, 1996, Vol. 118, pp. 115-121.

[33] El-Shafei., A., Tawfick, S. H., Raafat, M. S., Aziz, G. M., "Some Experiments on Oil Whirl and Oil Whip", *ASME Transaction: Journal of Engineering for Gas Turbine and Power*, 2007, Vol. 129, pp. 144-153.

[34] Zhao S., Xu, H., Meng, G., and Zhu, J., "Stability and Response Analysis of Symmetrical Single-Disk Flexible Rotor-Bearing System", *Tribology International*, 2005, Vol. 38(8) pp. 749-756.

[35] JianPing, J., Guang, M., Yi, S., and SongBo X., "On the Non-linear Dynamic Behavior of a Rotor–Bearing System", *Journal of Sound and Vibration*, 2004, Vol. 274(3-5), pp. 1031-1044.

[36] JianPing, J., Guang, M., Yi, S., and SongBo X., "On the Oil-Whipping of a Rotor-Bearing System by a Continuum Model", *Applied Mathematical Modelling*, 2005, Vol. 29(5), pp. 461-475.

[37] Castro, H. F., Cavalca, K. L. and Nordmann, R., “Whirl and Whip Instabilities in Rotor-Bearing System Considering a Nonlinear Force Model”, *Journal of Sound and Vibration*, 2008, Vol. 317(1-2), pp. 273-293.

[38] Chattopadhyay, A. K. and Majumdar B. C., “On the Stability of a Rigid Rotor in Finite Porous Journal Bearings with Slip”, *ASME Transaction: Journal of Tribology*, 1986, Vol. 108, pp. 190-194.

[39] Kumar, A., “Conical Whirl Instability of Turbulent Flow Hybrid Porous Journal Bearings”, *Tribology International*, 1998, Vol. 31(5), pp. 235–243.

[40] Guha. S. K., “Study of Conical Whirl Instability of Hydrodynamic Porous Oil Journal Bearings with Tangential Velocity Slip”, *Tribology International*, 1986, Vol. 19(2), pp. 72-78.

[41] Lund, J.W. and Orcutt, F. K., “Calculation and Experiments on the Unbalance Response of a Flexible Rotor”, *ASME Transaction: Journal of Engineering for Industry*, 1967, Series B, Vol. 89(4), pp. 785-796.

[42] Ozguven, H.N. and Ozkan, Z. L., “Whirl Speeds and Unbalance Response of Multibearing Rotors using Finite Elements”, *Journal of Vibration, Acoustics, Stress, and Reliability in Design*, 1984, Vol. 106 (1), pp. 72-79.

[43] Rao, J. S., “Conditions For Backward Synchronous Whirl of a Flexible Rotor in Hydrodynamic Bearings”, *Mechanism and Machine Theory*, 1981, Vol. 17(2), pp. 143-152.

[44] Sharan, A. M. and Rao, J. S., “Unbalance Response of Rotor-Disks Supported by Fluid-Film Bearings with a Negative Cross Coupled Stiffness using Influence Coefficient Method”, *Mechanism and Machine Theory*, 1985, Vol. 20(5), pp. 415-426.

[45] Curti, G., Raffa, F. A., and Vatta, F., “Unbalance Response of Rotor Systems by the Dynamic Stiffness Method”, 1992, *Mechanics Research Communications*, Vol. 19(4), pp. 351-359.

[46] Lee, C. W., and Jei Y. G., “Modal Analysis of Continuous Rotor-Bearing Systems”, *Journal of Sound and Vibration*, 1988, Vol. 126(2), pp. 345-361.

[47] Genta, G. and Bona F. D., “Unbalance Response of Rotors: A Modal Approach with some extensions to Damped Natural Systems”, *Journal of Sound and Vibration*, 1990, Vol. 140(1), pp. 129-153.

[48] Raffa, F. A. and Vatta, F., “The Dynamic Stiffness Method for Linear Rotor-Bearing Systems”, *ASME Transaction: Journal of Vibration and Acoustics*, 1996, Vol. 118, pp. 332-339.

[49] Shih, Y-P. and Lee, A-C., “Identification of the Unbalance Distribution in Flexible Rotor” *International Journal of Mechanical Sciences*, 1997, Vol. 39(7), pp. 841-857.

[50] Hong, S. -W. and Park J. -H., “An Efficient Method for the Unbalance Response Analysis of Rotor-Bearing Systems”, *Journal of Sound and Vibration*, 1997, Vol. 200(4), pp. 491-504.

[51] Lee, A. S. and Ha, J. W., “Prediction of Maximum Unbalance Responses of a Gear-coupled Two-Shaft Rotor-Bearing System”, *Journal of Sound and Vibration*, 2005, Vol. 283, pp. 507–523.

[52] Zhao, J. Y., Linnett, I. W., and Mclean L. J., “Unbalance Response of a Flexible Rotor Supported by a Squeeze Film Damper”, *ASME Transaction: Journal of Vibration and Acoustics*, 1998, Vol. 120, pp. 32-38.

[53] Va´zquez, J. A., Barrett, L. E., and Flack, R. D., “A Flexible Rotor on Flexible Bearing Supports: Stability and Unbalance Response”, *ASME Transaction: Journal of Vibration and Acoustics*, 2001, Vol. 123, pp. 137-144.

[54] Yang, T. and Lin, C., “Estimation of Distributed Unbalance of Rotors”, *ASME Transaction: Journal of Engineering for Gas Turbine and Power*, 2002, Vol. 124, pp. 976-983.

[55] Zachariadis, D. C., “Unbalance Response of Rotors Supported on Hydrodynamic Bearings Placed Close to Nodal Points of Excited Vibration Modes”, *ASME Transaction: Journal of Engineering for Gas Turbine and Power*, 2006, Vol. 128, pp. 661-669.

[56] Liu, Z., Huang, S., and Su, J., “Nonlinear Dynamic Analysis of an Unsymmetrical Generator-Bearing System”, *ASME Transaction, Journal of Vibration and Acoustics*, 2007, Vol. 129, pp.448-457.

[57] San Andrés, L., D. Rubio, and T.H. Kim, “Rotordynamic Performance of a Rotor Supported on Bump Type Foil Gas Bearings: Experiments and Predictions,” *ASME Transaction, Journal of Engineering for Gas Turbines and Power*, 2007, 129(3), pp. 850-857.

[58] Wilde, D.A., and San Andrés, L., “Comparison of Rotordynamic Analysis Predictions with the Test Response of Simple Gas Hybrid Bearings for Oil

Free Turbomachinery," *ASME Transaction, Journal of Engineering for Gas Turbines and Power*, 2006,128, pp. 634-643.

[59] De Santiago, O., and L. San Andrés, "Imbalance Response of a Rotor Supported on Flexure Pivot Tilting Pad Journal Bearings in Series with Integral Squeeze Film Dampers," 2003, *ASME Transaction: Journal of Engineering for Gas Turbines and Power,* 2003, 115, pp. 1026-1032.

[60] Myers, C. J., "Bifurcation Theory Applied to Oil Whirl in Plain Cylindrical Journal Bearings", *ASME Transaction: Journal of Applied Mechanics*, 1984, Vol. 51, pp. 244–250.

[61] Hollis, P. and Taylor, D. L., "Hopf Bifurcation to Limit Cycles in Fluid Film Bearings," *ASME Transaction: Journal of Tribology*, 1986, Vol. 108, pp. 184–189.

[62] Noah, S. T. and Sundarajan, P., "Significance of Considering Nonlinear Effects in Predicting the Dynamic Behavior of Rotating Machinery", *Journal of Vibration and Control*, 1995, Vol. 1(4), pp. 431-458.

[63] Wang, J. K. and Khonsari, M. M., "Application of Hopf Bifurcation Theory to Rotor-Bearing Systems with Consideration of Turbulent Effects", *Tribology International*, 2006, Vol. 39(7), pp. 701-714.

[64] Deepak, S. T. and Noah, S. T., "Experimental Verification of Subcritical Whirl Bifurcation of a Rotor Supported on a Fluid Film Bearing," *ASME Transaction: Journal of Tribology*, 1998, Vol.120, pp. 605–609.

[65] Shaw, J. and Shaw, S. W., "The Effects of Unbalance on Oil Whirl", *Nonlinear Dynamics*, 1990, Vol. 1, pp. 293-311.

[66] Lin., J-R. and Hwang, C-C., "Hopf Bifurcation to a Short Porous Journal-Bearing System using the Brinkman Model: Weakly Nonlinear Stability", *Tribology International*, 2002, Vol. 35 pp. 75–84.

[67] Brown, R. D., Addison, P. and Chan, A. H. C., "Chaos in the Unbalance Response of Journal Bearing", *Nonlinear Dynamics*, 1994, Vol. 5, pp. 421-432.

[68] Adiletta, G., Guido, A. R. and Rossi, C., "Chaotic Motion of Rigid Rotor in Short Journal Bearing", *Nonlinear Dynamics*, 1996, Vol. 10, pp. 251-269.

[69] Adiletta, G., Guido, A. R. and Rossi, C., "Nonlinear Dynamics of a Rigid Unbalanced Rotor in Journal Bearings. Part I: Theoretical Analysis", *Nonlinear Dynamics*, 1997, Vol. 14, pp. 57-87.

[70] Adiletta, G., Guido, A. R. and Rossi, C., “Nonlinear Dynamics of a Rigid Unbalanced Rotor in Journal Bearings. Part II: Experimental Analysis”, *Nonlinear Dynamics*, 1997, Vol. 14, pp. 157-189.

[71] Brancatti, R., Russo, M. and Russo, R., “On the Stability of Periodic Motions of an Unbalanced Rigid Rotor on Lubricated Journal Bearings”, *Nonlinear Dynamics*, 1996, Vol. 10, pp.175-185.

[72] Kim, Y. B. and Noah, S. T., “Bifurcation Analysis for a Modified Jeffcott Rotor with Bearing Clearances”, *Nonlinear Dynamics*, 1990, Vol. 1, pp. 221-241.

[73] Chen, C-L. and Yau, H-T, “Chaos in the Imbalance Response of a Flexible Rotor Supported by Oil Film Bearings with Non-Linear Suspension”, *Nonlinear Dynamics*, 1998, Vol. 9, pp. 71-90.

[74] Karpenko, E. V., Pavlovskaia, E. E. and Wiercigroch., M., “Bifurcation Analysis of a Preloaded Jeffcott Rotor”, *Chaos, Solitons and Fractals*, 2003, Vol. 15, pp. 407–416.

[75] Wang, C-C., Lo, C-Y. and Chen, C-K., Nonlinear Dynamic Analysis of a Flexible Rotor Supported by Externally Pressurized Porous Gas Journal Bearings”, *ASME Transaction: Journal of Tribology*, 2002, Vol. 124, pp. 553-561.

[76] Shen, G., Xiao, Z., Zhang, W. and Zheng, T., “Nonlinear Behavior Analysis of a Rotor Supported on Fluid-Film Bearings”, *ASME Transaction: Journal of Vibration and Acoustics*, 2006, Vol. 128, pp. 35-40.

[77] Valverde, J., Escalona, J. L., Freire, E. and Dominguez, J., “Stability and Bifurcation Analysis of a Modified Geometrically Nonlinear Orthotropic Jeffcott Model with Internal Damping”, *Nonlinear Dynamics*, 2005, Vol. 42, pp. 137-163.

[78] Wenhui, X., Yougang, T. and Yushu, C., “Analysis of Motion Stability of the Flexible Rotor-Bearing System with Two Unbalanced Disks”, *Journal of Sound and Vibration*, 2008, Vol. 310, pp. 381–393.

[79] Shen, X., Jia, J., Zhao, M. and Jianping, J., “Experimental and Numerical Analysis of Nonlinear Dynamics of Rotor–Bearing–Seal System”, *Nonlinear Dynamics*, 2008, Vol. 53, pp. 31-44.

[80] Wang, J. K. and Khonsari, M. M., “Bifurcation Analysis of a Flexible Rotor Supported by Two Fluid-Film Journal Bearings”, *ASME Transaction: Journal of Tribology*, 2006, Vol. 128, pp. 594-603.

[81] Wang, J. K. and Khonsari, M. M., “On the Hysteresis Phenomenon Associated With Instability of Rotor-Bearing Systems”, *ASME Transaction: Journal of Tribology*, 2006, Vol. 128, pp. 188-196.

[82] San Andrés, L., J.C. Rivadeneira, K. Gjika, C. Groves, and G. LaRue, “A Virtual Tool for Prediction of Turbocharger Nonlinear Dynamic Response: Validation Against Test Data,” *ASME Transaction, Journal of Engineering for Gas Turbines and Power*, 2007, 129(4), pp. 1035-1046.

[83] Zhu, S. and L. San Andrés, “Rotordynamic Performance of Flexure Pivot Hydrostatic Gas Bearings for Oil-Free Turbomachinery,” *ASME Transaction, Journal of Engineering for Gas Turbines and Power*, 2007, 129(4), pp. 1020-1027.

[84] San Andrés, L., J.C. Rivadeneira, M. Chinta, K. Gjika, G. LaRue,”Nonlinear Rotordynamics of Automotive Turbochargers – Predictions and Comparisons to Test Data,” *ASME Transaction: Journal of Engineering for Gas Turbines and Power*, 2007, 129, pp. 488-493

[85] Holt, C., L. San Andrés, S. Sahay, P. Tang, G. LaRue, and K. Gjika, “Test Response and Nonlinear Analysis of a Turbocharger Supported on Floating Ring Bearings,” *ASME Transaction:Journal of Vibrations and Acoustics*, 2005, 127, pp. 107-212.

[86] Morgan, V.T. and Cameron, A., “Mechanism of Lubrication in Porous Metal Bearings”. Proceedings, *Conference on Lubrication and Wear, Institution of Mechanical Engineers*, London, 1957, 89**,** pp. 151–157.

[87] Cusano, C., “Lubrication of Porous Journal Bearings”, *ASME Transaction: Journal of Lubrication Technology*, 1972, Vol. 94, pp. 69–73.

[88] Cheng, K. and Rowe, A.K., “A Selection Strategy for the Design of Externally Pressurized Journal Bearings”, *Tribology International*, 1995, Vol. 28(7), pp. 465-474.

[89] Kaneko, S. and Obara, S., “Experimental Investigation of Mechanism of Lubrication in Porous Journal Bearings: Part 1-Observation of Oil Flow in Porous Matrix”, *ASME Transaction: Journal of Tribology*, 1990, Vol. 112, pp. 618-623.

[90] Quan, Y-X. and Wang, P-M, “Theoretical Analysis and Experimental Investigation of a Porous Metal Bearing”, *Tribology International*, 1985, Vol. 18(2), pp. 67-73.

[91] Quan, Y-X., Ji, M., Tian, Y-G., Zhou, G-R., Shi, G-Y., Wang, G-L., “Investigation of Sintered Bronze Bearings under High Speed Conditions”, *Tribology International*, 1985, Vol. 18, pp. 75-80.

[92] Beavers, G. S. and Joseph, D. D., “Boundary Conditions at a Naturally Permeable Wall”, *Journal of Fluid Mechanics*, 1961, Vol. 30 (1), pp.197 - 207.

[93] Beavers, G. S., Sparrow, E. M. and Magnuson, R. A., “Experiments on Coupled Parallel Flows in a Channel and a Bounding Porous Medium”, *ASME Transaction: Journal of Basic Engineering*, 1970, Vol. 92 (4), pp. 843 - 848.

[94] Murti, P. R. K., “Effect of Slip Flow in Narrow Porous Bearings with Arbitrary Wall Thickness”, *ASME Transaction: Journal of Applied Mechanics*, 1973, Vol. 42(2), pp. 305-310.

[95] Rouleau, W. T. and Steiner, L. I., “Hydrodynamic Porous Journal Bearings, Part I: Finite Full Bearings”, *ASME Transaction: Journal of Lubrication Technology*, 1974, Vol. 96, pp. 346-353.

[96] Cusano, C., “An Analytical Study of Starved Porous Bearings”, *ASME Transaction: Journal of Lubrication Technology*, 1979, Vol. 101, pp. 38-47.

[97] Prakash, J. and Vij, S.K., “Analysis of Narrow Porous Journal Bearing using Beavers-Joseph Criterion of Velocity Slip”, *ASME Transaction: Journal of Applied Mechanics*, 1974, Vol. 96, pp. 348–353.

[98] Chandra, M., Malik, M. and Sinhasan, R., “Investigation of Slip Effects in Plane Porous Journal Bearing”, *Wear*, 1981, 73 (1), pp. 61-72.

[99] Chattopadhyay, A.K. and Majumdar, B.C., “Steady State Solution of Finite Hydrostatic Porous Oil Journal Bearing with Tangential Velocity Slip”, *Tribology International*, 1984, Vol. 17(6), pp. 317-323.

[100] Gururajan, K. and Prakash, J., “Effect of Velocity Slip in a Narrow Rough Porous Journal Bearing”, *IMechE, Part J: Journal of Engineering Tribology*, 2003, Vol. 217, pp. 59-70.

[101] Kumar, A. and Rao, N. S., “Steady-State Performance of Finite Hydrodynamic Porous Journal Bearing in Turbulent Regimes”, 1993, *Wear*, Vol. 167, pp. 212-126.

[102] Lin, J-R. and Hwang, C-C., "Hydrodynamic Lubrication of Finite Porous Journal Bearing-Use of the Brinkman-Extended Darcy Model", *International Journal of Mechanical Science*, 1994, Vol. 36(7), pp. 631-644.

[103] Gururajan, K. and Prakash, J., "Surface Roughness Effect on Infinitely Long Porous Journal Bearing", *ASME Transaction: Journal of Tribology*, 1999, Vol. 121, pp. 139-147.

[104] Elsharkawy, A., A. and Guedouar L. H., "Hydrodynamic Lubrication of Porous Journal Bearings using a modified Brinkman-Extended Darcy Model", *Tribology International*, 2001, Vol. 34(11), pp. 767-777.

[105] Meurisse, M.H. and Bernard G., "A 3D Conservative Model for Self-Lubricated Porous Journal Bearings in a Hydrodynamic Steady State", *ASME Transaction: Journal of Tribology*, 1999, Vol. 121, pp. 529-537.

[106] Chen, M-D., Chang, K-M., Lin, J-W., Li, W-L., "Lubrication of Journal Bearing-Influence of Stress Jump Condition at the Porous-Media/Fluid Film Interface", *Tribology International*, 2002, Vol. 35, pp. 287–295.

[107] Archer, J. S., "Consistent Mass Matrix of Distributed Mass System", *Proceedings of American Society of Civil Engineers*", 1963, Vol. 89, pp. 161-178.

[108] Ruhl, R. F. and Booker, J. F., "A Finite Element Model for Distributed Parameter Turbo Rotor System", *ASME Transaction, Journal of Engineering for Industry*, 1972, Vol. 94(1), pp. 128-132.

[109] Thorkildsen, T., "Solution of a Distributed Mass and Unbalanced Rotor System Using a Consistent Mass Matrix Approach", *MSE Engineering Report*, 1972, Arizona State University.

[110] Dimaragonas, A. D., "A General Method for Stability Analysis of Rotating Shafts," *Ingenieur-Archieve*, 1975, Vol. 44, pp. 9-20.

[111] Gasch, R., "Vibration of Large Turbo-Rotors in Fluid-Film Bearings on an Elastic Foundation," *Journal of Sound and Vibration*, 1976, Vol. 47, pp. 53-73.

[112] Nelson, H. D., and McVaugh, J. M., "The Dynamics of Rotor-Bearing Systems using Finite Elements", *ASME Transaction: Journal of Engineering for Industry*, 1976, Vol. 98(2), pp. 593-600.

[113] Zorzi, E. S. and Nelson H. D., "Finite Element Simulation of Rotor Bearing Systems with Internal Damping" *ASME Transaction: Journal of Engineering for Power*, 1977, Vol. 99, pp. 71-76.

[114] Rouch, K. E. and Kao J. S., "Dynamic Reduction in Rotor Dynamics by the Finite Element Method", *ASME Transaction: Journal of Mechanical Design*, 1980, Vol. 102, pp. 360-368.

[115] Kim, Y. D. and Lee, C. W., "Finite Element Analysis of Rotor Bearing System using Modal Transformation Matrix", *Journal of Sound and Vibration*, 1986, Vol. 111(3), pp. 441-456.

[116] Nelson, H. D., "A Finite Rotating Shaft Element using Timoshenko Beam Theory", *ASME Transaction: Journal of Mechanical Design*, 1980, Vol. 102, pp. 793-803.

[117] Chen, L. W. and Ku, D.M., "Finite Element Analysis of Natural Whirl Speeds of Rotating Shafts", *Computers and Structures*, 1991, Vol. 40(1), pp. 741-747.

[118] Ku, D. M., "Finite Element Analysis of Whirl Speeds for Rotor-Bearing Systems with Internal Damping", *Journal of Systems and Signal Processing*, 1998, Vol. 12(5), pp. 599-610.

[119] Khulief, Y.A. and Mohiuddin, M. A., "On the Dynamic Analysis of Rotors using Modal Reduction", *Finite Elements in Analysis and Design*, 1997, Vol. 26, pp. 41-55.

[120] Christopherson, D.G., "A New Mathematical Model for Solution of Film Lubrication Problems", *Proceedings of IMechE*, 1942, Vol. 146, pp. 126-135.

[121] Rao, J.S., Rotor Dynamics, *New Age International Publishers*, Third Edition, 1996.

APPENDIX 1

Non-dimensionalization and Elemental Matrices

The following non-dimensionalization scheme is introduced

$\bar{v} = \frac{v}{C}$, $\bar{w} = \frac{w}{C}$ $\bar{l} ,= \frac{l}{C}$, $\bar{t} = \Omega t$, $\bar{F} = \frac{F}{W}$ and $\bar{M} = \frac{M}{(WC)}$ where v and w are rotor displacements, l is length of shaft element, C is the clearance, F is the force, M is the moment and $W = \frac{g}{2}(\rho AL + m_d)$ is the load per bearing.

Thus, if displacement (vertical or horizontal) of the journal centre is denoted by δ then the non-dimensional displacement and their derivatives are given by,

$$\bar{\delta} = \frac{\delta}{C}\ ,\ \dot{\bar{\delta}} = \frac{\dot{\delta}}{(C\Omega)} \text{ and } \ddot{\bar{\delta}} = \frac{\ddot{\delta}}{(C\Omega^2)}.$$

Similarly, if the rotation of the journal centre (about X or Y-axis) is denoted by φ_{rot} then the non-dimensional rotations and their derivatives are given by,

$$\bar{\varphi}_{rot} = \varphi_{rot}\ ,\ \dot{\bar{\varphi}}_{rot} = \frac{\dot{\varphi}_{rot}}{\Omega} \text{ and } \ddot{\bar{\varphi}}_{rot} = \frac{\ddot{\varphi}_{rot}}{\Omega^2}.$$

Let m_j and K_j denote mass and stiffness of the journal then non-dimensional mass and stiffness are given by,

$$\bar{m}_j = \frac{m_j C\Omega^2}{W} \text{ and } \bar{K}_j = \frac{K_j C}{W} \text{ respectively.}$$

The above non-dimensional quantities are substituted into the finite element equation of the rotor (Eqn. (2.12)) and then after some algebraic manipulations the following non-dimensional finite element equation of the rotor is obtained,

$$\left(\left[\bar{M}_T\right]^e + \left[\bar{M}_R\right]^e\right)\left\{\ddot{\bar{q}}\right\}^e - \left[\bar{G}\right]^e\left\{\dot{\bar{q}}\right\}^e + \left[\bar{K}\right]^e\left\{\bar{q}\right\}^e = \left\{\bar{F}\right\}^e.$$

The elemental matrices in non-dimensional terms are given below,

$\Phi = 12\frac{E}{K'G}\left(\frac{R}{(2L)}\right)^2 k^2 = 24\frac{(1+\nu)}{K'}\left(\frac{R}{(2L)}\right)^2 k^2$ where $K' = \frac{6(1+\nu)}{(7+6\nu)}$ is the shear correction factor.

a) Stiffness matrix $\left[\bar{K}\right]=\left[\bar{K}\right]_0+\Phi\left[\bar{K}\right]_1$ (A1)

$$\left[\bar{K}\right]_0=\overline{KK}\begin{bmatrix} 12 & & & & & & & sym \\ 0 & 12 & & & & & & \\ 0 & -6\bar{l} & 4\bar{l}^2 & & & & & \\ 6\bar{l} & 0 & 0 & 4\bar{l}^2 & & & & \\ -12 & 0 & 0 & -6\bar{l} & 12 & & & \\ 0 & -12 & 6\bar{l} & 0 & 0 & 12 & & \\ 0 & -6\bar{l} & 2\bar{l}^2 & 0 & 0 & 6\bar{l} & 4\bar{l}^2 & \\ 6\bar{l} & 0 & 0 & 2\bar{l}^2 & -6\bar{l} & 0 & 0 & 4\bar{l}^2 \end{bmatrix}$$

$$\left[\bar{K}\right]_1=\overline{KK}\begin{bmatrix} 0 & & & & & & & sym \\ 0 & 0 & & & & & & \\ 0 & 0 & \bar{l}^2 & & & & & \\ 0 & 0 & 0 & \bar{l}^2 & & & & \\ 0 & 0 & 0 & 0 & 0 & & & \\ 0 & 0 & 0 & 0 & 0 & 0 & & \\ 0 & 0 & -\bar{l}^2 & 0 & 0 & 0 & \bar{l}^2 & \\ 0 & 0 & 0 & -\bar{l}^2 & 0 & 0 & 0 & \bar{l}^2 \end{bmatrix}$$

where $\overline{KK}=\dfrac{4k^3}{(1+\Phi)}\left(\dfrac{E}{(\rho gL)}\right)\left(\dfrac{C}{R}\right)\left(\dfrac{R}{(2L)}\right)^3\left(\dfrac{1}{1+\dfrac{m_d}{(\rho AL)}}\right)$

It has been observed from the above matrices the following non-dimensional parameters are obtained, stiffness parameter, $\dfrac{E}{(\rho gL)}$; clearance ratio, $\dfrac{R}{C}$; slenderness ratio, $\dfrac{R}{(2L)}$ and ratio of disk mass to shaft mass, $\dfrac{m_d}{(\rho AL)}$. Out of the above parameters , $\dfrac{E}{(\rho gL)}$ and $\dfrac{m_d}{(\rho AL)}$ are introduced in this thesis for the first time.

b) Translational Mass Matrix $\left[\bar{M}_T\right]=\left[\bar{M}_T\right]_0+\Phi\left[\bar{M}_T\right]_1+\Phi^2\left[\bar{M}_T\right]_2$ (A2)

$$\left[\bar{M}_T\right]_0=\overline{MT}\begin{bmatrix} 156 & & & & & & & sym \\ 0 & 156 & & & & & & \\ 0 & -22\bar{l} & 4\bar{l}^2 & & & & & \\ 22\bar{l} & 0 & 0 & 4\bar{l}^2 & & & & \\ 54 & 0 & 0 & 13\bar{l} & 156 & & & \\ 0 & 54 & -13\bar{l} & 0 & 0 & 156 & & \\ 0 & 13\bar{l} & -3\bar{l}^2 & 0 & 0 & 22\bar{l} & 4\bar{l}^2 & \\ -13\bar{l} & 0 & 0 & -3\bar{l}^2 & -22\bar{l} & 0 & 0 & 4\bar{l}^2 \end{bmatrix}$$

$$\left[\bar{M}_T\right]_1=\overline{MT}\begin{bmatrix} 294 & & & & & & & sym \\ 0 & 294 & & & & & & \\ 0 & -38.5\bar{l} & 7\bar{l}^2 & & & & & \\ 38.5\bar{l} & 0 & 0 & 7\bar{l}^2 & & & & \\ 126 & 0 & 0 & 31.5\bar{l} & 294 & & & \\ 0 & 126 & -31.5\bar{l} & 0 & 0 & 294 & & \\ 0 & 31.5\bar{l} & -7\bar{l}^2 & 0 & 0 & 38.5\bar{l} & 7\bar{l}^2 & \\ -31.5\bar{l} & 0 & 0 & -7\bar{l}^2 & -38.5\bar{l} & 0 & 0 & 7\bar{l}^2 \end{bmatrix}$$

$$\left[\bar{M}_T\right]_2=\overline{MT}\begin{bmatrix} 140 & & & & & & & sym \\ 0 & 140 & & & & & & \\ 0 & -17.5\bar{l} & 3.5\bar{l}^2 & & & & & \\ 17.5\bar{l} & 0 & 0 & 3.5\bar{l}^2 & & & & \\ 70 & 0 & 0 & 17.5\bar{l} & 140 & & & \\ 0 & 70 & -17.5\bar{l} & 0 & 0 & 140 & & \\ 0 & 17.5\bar{l} & -3.5\bar{l}^2 & 0 & 0 & 17.5\bar{l} & 3.5\bar{l}^2 & \\ -17.5\bar{l} & 0 & 0 & -3.5\bar{l}^2 & -17.5\bar{l} & 0 & 0 & 3.5\bar{l}^2 \end{bmatrix}$$

where $\overline{MT}=\left(\dfrac{C\Omega^2}{g}\right)\dfrac{1}{\left(210k\left(1+\Phi\right)^2\right)}\left(\dfrac{1}{1+\dfrac{m_d}{(\rho AL)}}\right)$.

From Eqn. (A2), the following non-dimensional parameters are obtained: mass parameter, $\dfrac{C\Omega^2}{g}$ and ratio of disk mass to shaft mass, $\dfrac{m_d}{(\rho AL)}$.

c) Rotational Mass Matrix $\left[\bar{M}_R\right] = \left[\bar{M}_R\right]_0 + \Phi\left[\bar{M}_R\right]_1 + \Phi^2\left[\bar{M}_R\right]_2$ (A3)

$$\left[\bar{M}_R\right]_0 = \overline{MR}\begin{bmatrix} 36 & & & & & & & sym \\ 0 & 36 & & & & & & \\ 0 & -3\bar{l} & 4\bar{l}^2 & & & & & \\ 3\bar{l} & 0 & 0 & 4\bar{l}^2 & & & & \\ -36 & 0 & 0 & -3\bar{l} & 36 & & & \\ 0 & -36 & 3\bar{l} & 0 & 0 & 36 & & \\ 0 & -3\bar{l} & -\bar{l}^2 & 0 & 0 & 3\bar{l} & 4\bar{l}^2 & \\ 3\bar{l} & 0 & 0 & -\bar{l}^2 & -3\bar{l} & 0 & 0 & 4\bar{l}^2 \end{bmatrix}$$

$$\left[\bar{M}_R\right]_1 = \overline{MR}\begin{bmatrix} 0 & & & & & & & sym \\ 0 & 0 & & & & & & \\ 0 & 15\bar{l} & 5\bar{l}^2 & & & & & \\ -15\bar{l} & 0 & 0 & 5\bar{l}^2 & & & & \\ 0 & 0 & 0 & 15\bar{l} & 0 & & & \\ 0 & 0 & -15\bar{l} & 0 & 0 & 0 & & \\ 0 & 15\bar{l} & -5\bar{l}^2 & 0 & 0 & 15\bar{l} & 5\bar{l}^2 & \\ -15\bar{l} & 0 & 0 & -5\bar{l}^2 & 15\bar{l} & 0 & 0 & 5\bar{l}^2 \end{bmatrix}$$

$$\left[\bar{M}_R\right]_2 = \overline{MR}\begin{bmatrix} 0 & & & & & & & sym \\ 0 & 0 & & & & & & \\ 0 & 0 & 10\bar{l}^2 & & & & & \\ 0 & 0 & 0 & 10\bar{l}^2 & & & & \\ 0 & 0 & 0 & 0 & 0 & & & \\ 0 & 0 & 0 & 0 & 0 & 0 & & \\ 0 & 0 & 5\bar{l}^2 & 0 & 0 & 0 & 10\bar{l}^2 & \\ 0 & 0 & 0 & 5\bar{l}^2 & 0 & 0 & 0 & 10\bar{l}^2 \end{bmatrix}$$

where, $\overline{MR} = \left(\dfrac{C\Omega^2}{g}\right)\left(\dfrac{R}{(2L)}\right)^2 \dfrac{k}{\left(15(1+\Phi)^2\right)}\left(\dfrac{1}{1+\dfrac{m_d}{(\rho AL)}}\right).$

The non-dimensional parameters obtained from Eqn. (A3) are: mass parameter, $\dfrac{C\Omega^2}{g}$; slenderness ratio, $\dfrac{R}{(2L)}$ and ratio of disk mass to shaft mass, $\dfrac{m_d}{(\rho AL)}$.

d) Gyroscopic Matrix $\left[\bar{G}\right]=\left[\bar{G}\right]_0+\Phi\left[\bar{G}\right]_1+\Phi^2\left[\bar{G}\right]_2$ (A4)

$$\left[\bar{G}\right]_0=\overline{GG}\begin{bmatrix} 0 & & & & & & & \textit{skew sym} \\ -36 & 0 & & & & & & \\ 3\bar{l} & 0 & 0 & & & & & \\ 0 & 3\bar{l} & -4\bar{l}^2 & 0 & & & & \\ 0 & -36 & 3\bar{l} & 0 & 0 & & & \\ 36 & 0 & 0 & 3\bar{l} & -36 & 0 & & \\ 3\bar{l} & 0 & 0 & -\bar{l}^2 & -3\bar{l} & 0 & 0 & \\ 0 & 3\bar{l} & \bar{l}^2 & 0 & 0 & -3\bar{l} & -4\bar{l}^2 & 0 \end{bmatrix}$$

$$\left[\bar{G}\right]_1=\overline{GG}\begin{bmatrix} 0 & & & & & & & \textit{skew sym} \\ 0 & 0 & & & & & & \\ -15\bar{l} & 0 & 0 & & & & & \\ 0 & -15\bar{l} & -5\bar{l}^2 & 0 & & & & \\ 0 & 0 & -15\bar{l} & 0 & 0 & & & \\ 0 & 0 & 0 & -15\bar{l} & 0 & 0 & & \\ -15\bar{l} & 0 & 0 & -5\bar{l}^2 & 15\bar{l} & 0 & 0 & \\ 0 & -15\bar{l} & 5\bar{l}^2 & 0 & 0 & 15\bar{l} & -5\bar{l}^2 & 0 \end{bmatrix}$$

$$\left[\bar{G}\right]_2=\overline{GG}\begin{bmatrix} 0 & & & & & & & \textit{skew sym} \\ 0 & 0 & & & & & & \\ 0 & 0 & 0 & & & & & \\ 0 & 0 & -10\bar{l}^2 & 0 & & & & \\ 0 & 0 & 0 & 0 & 0 & & & \\ 0 & 0 & 0 & 0 & 0 & 0 & & \\ 0 & 0 & 0 & 5\bar{l}^2 & 0 & 0 & 0 & \\ 0 & 0 & -5\bar{l}^2 & 0 & 0 & 0 & -10\bar{l}^2 & 0 \end{bmatrix}$$

where, $\overline{GG}=\left(\frac{C\Omega^2}{g}\right)\left(\frac{R}{(2L)}\right)^2\frac{2k}{\left(15(1+\Phi)^2\right)}\left(\frac{1}{1+\frac{m_d}{(\rho AL)}}\right).$

The non-dimensional parameters obtained from Eqn. (A4) are: mass parameter, $\frac{C\Omega^2}{g}$, slenderness ratio, $\frac{R}{(2L)}$ and and ratio of disk mass to shaft mass, $\frac{m_d}{(\rho AL)}$.

e) Mass Matrix of the Disk

$$\left[\bar{M}^{d}\right]=\overline{MD}\begin{bmatrix} \dfrac{m_d}{(\rho AL)} & 0 & 0 & 0 \\ 0 & \dfrac{m_d}{(\rho AL)} & 0 & 0 \\ 0 & 0 & \dfrac{I_d}{(\rho ALC^2)} & 0 \\ 0 & 0 & 0 & \dfrac{I_d}{(\rho ALC^2)} \end{bmatrix}$$

f) Gyroscopic Matrix of the Disk

$$\left[\bar{M}^{d}\right]=\overline{MD}\begin{bmatrix} 0 & 0 & 0 & 0 \\ 0 & 0 & 0 & 0 \\ 0 & 0 & 0 & \dfrac{I_p}{(\rho ALC^2)} \\ 0 & 0 & -\dfrac{I_p}{(\rho ALC^2)} & 0 \end{bmatrix}$$

where, $\overline{MD}=2\left(\dfrac{C\Omega^2}{g}\right)\left(\dfrac{1}{1+\dfrac{m_d}{(\rho AL)}}\right)$

g) Sommerfeld number

$$S=\frac{\eta\Omega L_B D}{(2\pi W)}\left(\frac{R}{C}\right)^2=\left(\frac{4\eta\Omega}{(\pi^2\rho L_B g)}\right)\left(\frac{L_B}{D}\right)\left(\frac{R}{C}\right)^2$$

h) Non-dimensional Bearing Forces

Hydrodynamic force component is given by,

$F=\bar{F}^{B}\eta\Omega RL_B\left(\dfrac{R}{C}\right)^2$ where, $\bar{F}^{B}$ is obtained by solving the dimensionless modified Reynolds equation for pressure and then double integrating the dimensionless pressure over the clearance space.

Non-dimensional forces acting on rotor is then given by,

$$\bar{F} = \frac{F}{W} = \frac{\bar{F}^B \eta \Omega R L_B \left(\frac{R}{C}\right)^2}{\left(\rho A L + m_d\right) g/2} = \bar{F}^B \pi S \,.$$

i) Non-dimensional Unbalance Forces

The amplitude of unbalance force components are given by, $F_d = m_d e_d \Omega^2$.

Therefore, this force component can be non-dimensionalized by dividing with W.

Thus, non-dimensional unbalance force is,

$$\bar{F}_d = \frac{F_d}{W} = \frac{m_d e_d \Omega^2}{W} = 2\left(\frac{C\Omega^2}{g}\right)\left(\frac{e_d}{C}\right)\frac{\frac{m_d}{(\rho AL)}}{\left(1+\frac{m_d}{(\rho AL)}\right)}$$

APPENDIX 2

Relation between Sommerfeld Number and Mass Parameter

Sommerfeld number is defined as follows, $S = \frac{\eta \Omega L_B D}{\left(2\pi W\right)}\left(\frac{R}{C}\right)^2$. Let S_1 and S_2 are two Sommerfeld numbers corresponding to two spin speeds Ω_1 and Ω_2 respectively *i.e.*, $S_1 = \frac{\eta \Omega_1 L_B D}{\left(2\pi W\right)}\left(\frac{R}{C}\right)^2$ and $S_2 = \frac{\eta \Omega_2 L_B D}{\left(2\pi W\right)}\left(\frac{R}{C}\right)^2$. The corresponding mass parameters are then $\bar{m}_1 = \frac{C\Omega_1^2}{g}$ and $\bar{m}_2 = \frac{C\Omega_2^2}{g}$ respectively. From above relations we can write, $\frac{\bar{m}_1}{\bar{m}_2} = \frac{\Omega_1^2}{\Omega_2^2} = \frac{S_1^2}{S_2^2}$.

APPENDIX 3

A Sample MATLAB Program for Time-transient Analysis of Rotor-Bearing System with Velocity Slip

---

```
clear all;
clc;
%% omebar=(clearance*omega^2/g) ; mass parameter

BEARING_LD=1.0;
BETA=0.03;
ALP=10;

L=1;
n=16;            % no of elements
rho=7830;
E=2.07e11;
g=9.81;
ECr=(E/(rho*g*L));
poi=0.3;
G=E/(2*(1+poi));
ka=6*(1+poi)/(7+6*poi);
LD=20.0;                ( slenderness ratio of the shaft, L/D= ');
DL=1/LD;
omebar=3.4;
RC=500;
LC=2*LD*RC;
lbar=LC/n;
CL=1/LC;
phi=0.75*(E*n^2/(ka*G))*DL^2;
ts=0.0025;
no_time_steps=40000;
node_num=1;
node_num=node_num-1;


KK=n^3*ECr*DL^2*CL/(8*(1+phi));
k0=KK*([12 0 0 (6*lbar) -12 0 0 (6*lbar);
         0 12 -(6*lbar) 0 0 -12 (-6*lbar) 0;
         0 (-6*lbar) (4*lbar^2) 0 0 (6*lbar) (2*lbar^2) 0;
         (6*lbar) 0 0 (4*lbar^2) (-6*lbar) 0 0 (2*lbar^2);
         -12 0 0 (-6*lbar) 12 0 0 (-6*lbar);
         0 -12 (6*lbar) 0 0 12 (6*lbar) 0;
         0 (-6*lbar) (2*lbar^2) 0 0 (6*lbar) (4*lbar^2) 0;
         (6*lbar) 0 0 (2*lbar^2) (-6*lbar) 0 0 (4*lbar^2)]);
k1=KK*([0 0 0 0 0 0 0 0;
         0 0 0 0 0 0 0 0;
         0 0 lbar^2 0 0 0 -lbar^2 0;
         0 0 0 lbar^2 0 0 0 -lbar^2;
         0 0 0 0 0 0 0 0;
         0 0 0 0 0 0 0 0;
         0 0 -lbar^2 0 0 0 lbar^2 0;
         0 0 0 -lbar^2 0 0 0 lbar^2]);
kb=k0+phi*k1;
```

```
MT=omebar/(210*n*(1+phi)^2);
mt0=MT*([156 0  0  22*lbar  54  0  0   -13*lbar;
          0 156 -22*lbar  0  0 54 13*lbar 0;
          0 -22*lbar  4*lbar^2 0  0  -13*lbar -3*lbar^2 0;
        22*lbar 0  0  4*lbar^2  13*lbar   0  0  -(3*lbar^2);
          54   0   0  13*lbar  156   0    0   -22*lbar;
          0  54    -13*lbar  0   0  156  22*lbar  0;
          0      13*lbar  -3*lbar^2   0  0   22*lbar 4*lbar^2 0;
        -13*lbar  0  0 -(3*lbar^2)  -22*lbar 0  0 (4*lbar^2)]);

mt1=MT*([  294   0  0 38.5*lbar  126  0  0  -31.5*lbar;
            0  294  -38.5*lbar 0  0  126  31.5*lbar 0;
            0 -38.5*lbar  7*lbar^2  0  0 -31.5*lbar   -7*lbar^2    0;
         38.5*lbar 0  0 7*lbar^2  31.5*lbar 0  0  -7*lbar^2;
           126  0   0 31.5*lbar   294   0  0 -38.5*lbar;
            0  126  -31.5*lbar  0   0  294  38.5*lbar   0;
            0  31.5*lbar  -7*lbar^2  0   0  38.5*lbar 7*lbar^2  0;
         -31.5*lbar   0 0 -7*lbar^2  -38.5*lbar  0   0  7*lbar^2]);

mt2=MT*([140   0  0  17.5*lbar  70 0  0 -17.5*lbar;
          0 140 -17.5*lbar 0 0 70 17.5*lbar  0;
          0 -17.5*lbar (3.5*lbar^2) 0  0 -17.5*lbar -(3.5*lbar^2)  0;
          17.5*lbar   0  0   (3.5*lbar^2) 17.5*lbar  0  0   -
(3.5*lbar^2);
          70    0  0  17.5*lbar  140    0 0     -17.5*lbar;
          0  70  -17.5*lbar 0  0   140    17.5*lbar  0;
          0     17.5*lbar  -(3.5*lbar^2)   0  0  17.5*lbar
(3.5*lbar^2) 0;
          -17.5*lbar   0  0 -(3.5*lbar^2) -17.5*lbar  0 0
(3.5*lbar^2)]);

me=mt0+phi*mt1+(phi^2)*mt2;

MR=omebar*n*DL^2/(240*(1+phi)^2);
mr0=MR*([36      0    0         3*lbar     -36       0       0
3*lbar;
         0      36      -3*lbar     0         0      -36    -3*lbar
0;
         0    -3*lbar   4*lbar^2   0         0      3*lbar  -lbar^2
0;
       3*lbar   0    0      4*lbar^2  -3*lbar   0        0        -
lbar^2;
        -36     0   0        -3*lbar     36       0       0        -
3*lbar;
         0   -36  3*lbar    0       0       36     3*lbar      0;
         0  -3*lbar   -lbar^2    0     0     3*lbar    4*lbar^2    0;
       3*lbar   0      0  -lbar^2   -3*lbar   0      0  4*lbar^2]);

mr1=MR*([0   0  0   -15*lbar  0   0 0  -15*lbar;
        0   0  15*lbar  0    0   0       15*lbar       0;
        0  15*lbar    5*lbar^2    0   0  -15*lbar  -5*lbar^2      0;
     -15*lbar  0   0   5*lbar^2   15*lbar    0   0    -5*lbar^2;
        0  0  0   15*lbar  0  0    0   15*lbar;
        0 0  -15*lbar    0   0   0 15*lbar  0;
        0      15*lbar    -5*lbar^2    0   0  15*lbar   5*lbar^2  0;
     -15*lbar 0 0 -5*lbar^2   15*lbar   0   0  5*lbar^2]);

mr2=MR*([0       0       0       0      0       0      0       0;
         0       0       0       0      0       0      0       0;
```

```
         0       0    10*lbar^2  0       0       0   5*lbar^2   0;
         0       0       0    10*lbar^2 0       0      0    5*lbar^2;
         0       0       0       0       0       0      0        0;
         0       0       0       0       0       0      0        0;
         0       0    5*lbar^2    0       0       0   10*lbar^2  0;
         0       0       0    5*lbar^2   0       0      0
10*lbar^2]);
mr=mr0+phi*mr1+(phi^2)*mr2;

GG=omebar*n*DL^2/(120*(1+phi)^2);
g0=GG*([ 0     36     -(3*lbar)       0    0   -36     -(3*lbar)
0;
       -36    0     0       -(3*lbar)     36  0     0      -(3*lbar);
     (3*lbar) 0     0   (4*lbar^2)   -(3*lbar)    0    0   -lbar^2;
        0 (3*lbar)  -(4*lbar^2)  0     0    -(3*lbar)  lbar^2   0;
        0    -36   (3*lbar)  0    0     36  (3*lbar)      0;
       36    0    0 (3*lbar)  -36    0     0    (3*lbar);
      (3*lbar)  0    0     -lbar^2   -(3*lbar)     0    0   (4*lbar^2);
        0  (3*lbar)  lbar^2  0     0    -(3*lbar)  -(4*lbar^2)    0]);

g1=GG*([  0    0    (15*lbar)    0     0    0   (15*lbar)      0;
         0    0    0    (15*lbar)   0     0      0        (15*lbar);
     -(15*lbar)  0     0   (5*lbar^2)  (15*lbar)   0    0         -
(5*lbar^2);
         0      -(15*lbar)  -(5*lbar^2)     0    0    (15*lbar)
(5*lbar^2)   0;
         0    0  -(15*lbar) 0      0    0     -15*lbar      0;
         0     0    0     -(15*lbar)      0     0    0     -(15*lbar);
     -(15*lbar)    0   0     -(5*lbar^2)  15*lbar    0     0    (5*lbar^2);
         0    -(15*lbar) (5*lbar^2)     0    0    (15*lbar)   -(5*lbar^2)
0]);

g2=GG*([  0     0     0     0    0      0     0   0 ;
         0    0      0  0       0      0     0      0;
         0   0    0   (10*lbar^2)    0    0     0  (5*lbar^2);
         0    0 -(10*lbar^2)     0    0     0    -(5*lbar^2)   0;
         0    0    0      0      0     0      0     0;
         0    0      0   0      0    0      0      0;
         0   0 0   (5*lbar^2)    0     0      0   (10*lbar^2);
         0   0   -(5*lbar^2)   0  0     0     -(10*lbar^2)   0]  );

ge=g0+phi*g1+(phi^2)*g2;%element gyroscopic matrix
m=4*(n+1);

   kg=zeros(m,m);
   kgg=zeros(m,m);

   Mg=zeros(m,m);
   Mgg=zeros(m,m);

   Mr=zeros(m,m);
   Mrr=zeros(m,m);

   gy=zeros(m,m);
   Gy=zeros(m,m);

   m1=1;
   m2=8;
   p=0;
```

```
    for e= 1:n
        for i= m1:m2
            for j= m1:m2
                kg(i,j)=kb(i-p,j-p);
                Mg(i,j)=me(i-p,j-p);
                Mr(i,j)=mr(i-p,j-p);
                gy(i,j)=ge(i-p,j-p);
            end
        end
        kgg=kgg+kg;
        Mgg=Mgg+Mg;
        Mrr=Mrr+Mr;
        Gy=Gy+gy;
        m1=m1+4;
        m2=m2+4;
        p=p+4;
        kg=zeros(m,m);
        Mg=zeros(m,m);
        Mr=zeros(m,m);
        gy=zeros(m,m);
    end

C1=-Gy;
M=Mgg+Mrr;
K=kgg;

K=sparse(K);
M=sparse(M);
C1=sparse(C1);

Ri=zeros(m,1);

% preallocation
eccn=zeros(no_time_steps,1);
att=zeros(no_time_steps,1);
xy=zeros(2,no_time_steps);
xym=zeros(2,no_time_steps);

for bi=1:4:m-3
displi(bi)=-0.5;
displi(bi+1)=0;
displi(bi+2)=0;
displi(bi+3)=0;
end
displi=displi';

P0=zeros(42,13,17);
somnum=0.1796;

veli=zeros(m,1);
K1=K*displi;
acci=inv(M)*(Ri-K1);

epsilon=0.5;
epsdot=0;
phidot=0;
phis=0;
PP=P0;
```

```
for ii=2:no_time_steps

    [WR,WPHI,P1]=porous_with_slip(BETA,RC,BEARING_LD,ALP,...
                  epsilon,phidot,epsdot,PP);
    R=zeros(m,1);
    PP=P1;
    FZ=(WPHI*pi*somnum*sin(phis)-WR*pi*somnum*cos(phis)-1);
    FY=-(WPHI*pi*somnum*cos(phis)+WR*pi*somnum*sin(phis));
    R(1+4*node_num)=FZ;
    R(2+4*node_num)=FY;
    R(m-3-4*node_num)=FZ;
    R(m-2-4*node_num)=FY;

[displ,vel,acc]=wilsontheta_method(K,M,R,Ri,C1,displi,veli,acci,ts);
    z1=-(displ(1+4*node_num));
    y1=-(displ(2+4*node_num));
    zdot1=-(vel(1+4*node_num));
    ydot1=-(vel(2+4*node_num));
    epsilon=sqrt(y1*y1+z1*z1);
    if epsilon >1.0
        stop;
    end
    eccn(ii)=epsilon;
    phis=atan2(y1,z1);
    att(ii)=phis;
    epsdot=ydot1*sin(phis)+zdot1*cos(phis);
    phidot=(ydot1*cos(phis)-zdot1*sin(phis))/epsilon;
    xy(:,ii)=displ(1+4*node_num:2+4*node_num);
    xym(:,ii)=displ(m/2-1:m/2);
    displi=displ;
    veli=vel;
    acci=acc;
    Ri=R;
    ii
end

% Trajectory
figure(1)
plot(xym(2,2:no_time_steps),xym(1,2:no_time_steps),'-k')
xlabel('$\overline{v}$','Interpreter','latex',...
'FontSize',18,'FontName','Arial');
ylabel('$\overline{w}$','Interpreter','latex',...
'FontSize',18,'FontName','Arial');

bb=zeros(no_time_steps,1);
bb(1)=0;
for bc=2:no_time_steps
   bb(bc)=bb(bc-1)+ts;
end

% Response
figure(2)
plot(bb(2:no_time_steps),xy(1,2:no_time_steps),...
'-k',bb(2:no_time_steps),xy(2,2:no_time_steps),'--k')
legend('$\overline{w}$','$\overline{v}$','Interpreter'...
,'latex','FontSize',18,'FontName','Arial');
xlabel('$\overline{t}$','Interpreter','latex','FontSize',18,...
    'FontName','Arial');
ylabel('$\overline{v}$,
$\overline{w}$','Interpreter','latex','FontSize',18,...
```

```
    'FontName','Arial');

% polar plot
figure(5)
polar(att(2:no_time_steps),eccn(2:no_time_steps))

figure(8)
plot(bb(2:no_time_steps),xym(1,2:no_time_steps),...
'-k',bb(2:no_time_steps),xym(2,2:no_time_steps),'--k')
legend('$\overline{w}$','$\overline{v}$','Interpreter',...
'latex','FontSize',18,'FontName','Arial');
xlabel('$\overline{t}$','Interpreter','latex','FontSize',18,...
    'FontName','Arial');
ylabel('$\overline{v}$,
$\overline{w}$','Interpreter','latex','FontSize',18,...
    'FontName','Arial');

dt=ts;
Fs=1/dt;
y=xym(2,20000:no_time_steps);
L=length(y);
f = (Fs)*(2*pi)*linspace(0,1,L);
Y = fft(y-mean(y))/L;
% % % % % % Plot single-sided amplitude spectrum.
figure(6)
plot(f(1:24),2*abs(Y(1:24)),'-k')
xlabel('\omega/\Omega', 'Fontsize',18)
ylabel('Amplitude', 'Fontsize',18)



            %%%%----------------------------------------%%%

function [WR,WPHI,P]=porous_with_slip(BETA,...
            RC,BEARING_LD,ALP,epsilon,phidot,epsdot,P0)

% % % % % % BEARING PARAMETERS

R=BEARING_LD;
HR=0.2;
KTH=1.0;
KZ=1.0;
COEF=12*RC/(BETA*HR);
SIGY=sqrt(COEF);
SIGX=SIGY*sqrt(1/KTH);
SIGZ=SIGY*sqrt(1/KZ);

RR=(1/R)^2;
RH=(1/HR)^2;
%%GRID SIZES
L=40;
M=12;
N=16;
ORF=1.65;
DEL=2*pi/L;
DELZ=1.0/N;
DELY=1.0/M;
DEL2=DEL^2;
DELY2=DELY^2;
DELZ2=DELZ^2;
```

```
%CONSTANTS FOR POROUS LAYER
C0=2.0*(KTH/DEL2+RH/DELY2+(KZ*RR)/DELZ2);
C1=KTH/(C0*DEL2);
C2=RH/(C0*DELY2);
C3=(KZ*RR)/(C0*DELZ2);
%INITIALISATION OF PRESSURE IN POROUS LAYER
P=P0;
% P=zeros(L+2,M+1,N+1);
SPO=0.0;
%BOUNDARY CONDITIONS
P(2:L+2,2:M+1,N+2)=0.0;
ERR1=1.0;
while abs(ERR1)>0.0001
P(2:L+2,1,2:N+1)=-(P(2:L+2,3,2:N+1)-4.*P(2:L+2,2,2:N+1))/3.0;
if P(2:L+2,1,2:N+1)<0.0
    P(2:L+2,1,2:N+1)=0.0;
end

P(2:L+2,2:M+1,1)=P(2:L+2,2:M+1,3);

%FILM THICKNESS
AI=zeros(1,L);
TH=zeros(1,L);
H=zeros(1,L);
for I=2:L+1
    AI(I)=(I-2);
    TH(I)=AI(I)*DEL;
    H(I)=1.0+epsilon*cos(TH(I));
end
H(1)=H(L+1);
H(L+2)=H(2);


% CALCULATION OF VARIOUS SLIP FUNCTIONS
AX=zeros(1,L);
AY=zeros(1,L);
AZ=zeros(1,L);
PSIX=zeros(1,L);
PSIZ=zeros(1,L);
PSIOX=zeros(1,L);
for I=1:L+2

    AX(I)=3*(H(I)*SIGX+2*ALP)/((H(I)*SIGX)*(1+H(I)*ALP*SIGX));
    AZ(I)=3*(H(I)*SIGZ+2*ALP)/((H(I)*SIGZ)*(1+H(I)*ALP*SIGZ));
    AY(I)=1/(1+H(I)*ALP*SIGX);

% % % % % %     NO SLIP CASE:
%     AX(I)=0.0;
%     AY(I)=0.0;
%     AZ(I)=0.0;

    PSIX(I)=(1.0+AX(I))*(H(I))^3;
    PSIZ(I)=(1.0+AZ(I))*(H(I))^3;
    PSIOX(I)=(1.0+AY(I))*(H(I));
end

%PRESSURE IN POROUS LAYER
TERM=zeros(L+1,M,N+1);
ERR2=zeros(L+1,M,N+1);
```

```
for I=2:L+1
    for J=2:M
        for K=2:N+1
            TERM(I,J,K)=C1*(P(I+1,J,K)+P(I-
1,J,K))+C2*(P(I,J+1,K)+P(I,J-1,K))+C3*...
                (P(I,J,K+1)+P(I,J,K-1));
            ERR2(I,J,K)=TERM(I,J,K)-P(I,J,K);
            P(I,J,K)=P(I,J,K)+ORF*ERR2(I,J,K);
            if (P(I,J,K)< 0.0)
                P(I,J,K)=0.0;
            end
            P(2,J,K)=P(L+2,J,K);
            P(L+1,J,K)=P(1,J,K);
        end
    end
end


%    *********************************
%       SOLUTION FOR REYNOLDS EQUATION
%     *********************************

A1=zeros(L+1,N+1);
A2=zeros(L+1,N+1);
A3=zeros(L+1,N+1);
A4=zeros(L+1,N+1);
C4=zeros(1,L+1);
C5=zeros(L+1,N+1);
C6=zeros(L+1,N+1);
C7=zeros(1,L+1);
C8=zeros(1,L+1);
C9=zeros(1,L+1);
C10=zeros(1,L+1);
C11=zeros(1,L+1);
DPDY=zeros(L+1,N+1);
C12=zeros(L+1,N+1);
TERM=zeros(L+1,N+1);
ERR=zeros(L+1,N+1);

for I=2:L+1
    for K=2:N+1
        AI(I)=I;
        TH(I)=(AI(I)-2)*DEL;
        A1(I)=PSIX(I)+0.25*(PSIX(I+1)-PSIX(I-1));
        A2(I)=PSIX(I)-0.25*(PSIX(I+1)-PSIX(I-1));
        A3(I)=PSIZ(I);
        A4(I)=PSIZ(I);
        C4(I)=2.0*((PSIX(I))/DEL2+RR*(PSIZ(I))/DELZ2);
        C5(I)=A1(I)/(C4(I)*DEL2);
        C6(I)=A2(I)/(C4(I)*DEL2);
        C7(I)=RR*A3(I)/(DELZ2*C4(I));
        C8(I)=RR*A4(I)/(DELZ2*C4(I));
        C9(I)=-3.0*(PSIOX(I+1)-PSIOX(I-1))/(DEL*C4(I));
        C10(I)=-12.0*epsdot*cos(TH(I))/C4(I);
        C11(I)=-12.0*phidot*epsilon*sin(TH(I))/C4(I);
        DPDY(I,K)=(3.0*P(I,M+1,K)-4.0*P(I,M,K)+P(I,M-
1,K))/(DELY*2.0);
        C12(I,K)=-BETA*DPDY(I,K)/C4(I);
        TERM(I,K)=C5(I)*P(I+1,M+1,K)+C6(I)*...
P(I-1,M+1,K)+C7(I)*P(I,M+1,K+1)+...
```

```
            C8(I)*P(I,M+1,K-1)+C9(I)+C10(I)+C11(I)+C12(I,K);
        ERR(I,K)=TERM(I,K)-P(I,M+1,K);
        P(I,M+1,K)=P(I,M+1,K)+ERR(I,K)*ORF;
        if (P(I,M+1,K)< 0.0);
            P(I,M+1,K)=0.0;
        end
        P(2,M+1,K)=P(L+2,M+1,K);
        P(L+1,M+1,K)=P(1,M+1,K);
    end
end

% % %TEST FOR CONVERGENCE
SPN=sum(sum(sum(P(:,M+1,:))));
ERR1=(SPN-SPO)/SPN;
SPO=SPN;
end
% P1=P;
PP(:,:)=P(:,M+1,:);
% mesh(PP)
dd=find(PP(:,N/2)); %#ok<MXFND>
LL=max(dd);

%EVALUATION OF LOAD BEARING CAPACITY

F1=zeros(N+2);
F2=zeros(N+2);
BI=zeros(LL);
TH1=zeros(LL);
TH2=zeros(LL);
TH3=zeros(LL);
TRM1=zeros(LL,N+1);
TRM2=zeros(LL,N+1);

for K=2:N+2
    for I=2:2:LL
        BI(I)=I-2;
        TH1(I)=BI(I)*DEL;
        TH2(I)=(BI(I)+1)*DEL;
        TH3(I)=(BI(I)+2)*DEL;

TRM1(I,K)=P(I,M+1,K)*cos(TH1(I))+4.0*P(I+1,M+1,K)*cos(TH2(I))...
            +P(I+2,M+1,K)*cos(TH3(I));

TRM2(I,K)=P(I,M+1,K)*sin(TH1(I))+4.0*P(I+1,M+1,K)*sin(TH2(I))...
            +P(I+2,M+1,K)*sin(TH3(I));
        F1(K)=F1(K)+TRM1(I,K)*DEL/3.0;
        F2(K)=F2(K)+TRM2(I,K)*DEL/3.0;
    end
end
WR=0.0;
WPHI=0.0;
TERM1=zeros(N+1);
TERM2=zeros(N+1);
for K=2:2:N
    TERM1(K)=F1(K)+4.0*F1(K+1)+F1(K+2);
    TERM2(K)=F2(K)+4.0*F2(K+1)+F2(K+2);
    WR=WR+TERM1(K)*DELZ/3.0;
    WPHI=WPHI+TERM2(K)*DELZ/3.0;
end
% WBAR=sqrt(WR*WR+WPHI*WPHI);
```

```
% SOMNUM=1/(pi*WBAR)


          %%%%----------------------------------------%%%
function [displ,vel,acc]=wilsontheta_method...
(K,M,R,Ri,C1,displi,veli,acci,ts)
theta=1.4;
a0=6/(theta*ts)^2;
a1=3/(theta*ts);
a2=2*a1;
a3=(theta*ts)/2;
a4=a0/theta;
a5=-a2/theta;
a6=1-3/theta;
a7=ts/2;
a8=ts*ts/6;

K_effective=K+a0*M+a1*C1;
R_effective=R+theta*(R-Ri)+M*(a0*displi+a2*veli+2*acci)...
    +C1*(a1*displi+2*veli+a3*acci);
theta_delt_disp=inv(K_effective)*R_effective;

acc=a4*(theta_delt_disp-displi)+a5*veli+a6*acci;
vel=veli+a7*(acc+acci);
displ=displi+ts*veli+a8*(acc+2*acci);
```

This program will give critically stable trajectory when

$R/2L = 0.0125$, $E/(\rho g L) = 2.7\times10^6$, $L_B/D = 1.0$, $\beta = 0.03$, $S = 0.1796$ and $\alpha = 10.0$

List of Publications

International Journal

- S K Laha, H Banzare, S K Kakoty, "Stability analysis of flexible rotor supported on finite hydrodynamic porous journal bearing using non-linear transient method", *Proc. IMechE, Part J: J. Engg. Tribol.*, Vol. 222, No. 7, 2008, pp. 963-973.
- S K Laha, S K Kakoty, "Non-linear dynamic analysis of a flexible rotor supported on porous oil journal bearing", *Comm. in Nonl. Sc. & Num. Simul.,* Vol. 6(3), 2010, pp. 1617-1631.

International Conference

- S K Laha, S K Kakoty, "Effect of unbalance on the dynamic response of a flexible rotor supported on porous oil journal bearing", IUTAM Symposium on Emerging Trends in Rotordynamics, 23-26 March, 2009, IIT Delhi,
- S K Laha, S K Kakoty, "On the non-linear dynamics of a flexible rotor supported on porous journal bearing", VETOMAC VI, 13-15 December, 2010,IIT Delhi.

Vitae

Born and brought up in Durgapur, West Bengal Mr. Swarup Kumar Laha is the eldest son of Mr. Sadhan Laha and Mrs. Suchitra Laha. After schooling from Durgapur, he graduated in Mechanical Engineering from National Institute of Technology, Rourkela (erstwhile Regional Engineering College, Rourkela) in 2002. He took his Master of Engineering (M.E.) degree in Machine Design from Bengal Engineering and Science University, Shibpur, Howrah in 2005. Then he joined Department of Mechanical Engineering of Indian Institute of Technology Guwahati as a Research Scholar in 2005 and worked under supervision of Prof. S K Kakoty.

Recently, he has joined Central Mechanical Engineering Research Institute (CMERI), Durgapur as Scientist 'C'.